SWOT Project

MISSION PERFORMANCE AND ERROR BUDGET

Revision A

Prepared by:

Daniel Esteban Fernandez
Lead Mission Performance Engineer

Date

Approved:

Lee-Lueng Fu
Project Scientist

Date

Brian Pollard
KaRIn Instrument Manager

Date

Parag Vaze
Project Manager

Date

Concurred:

Robert Abelson
Project System Engineer

Date

Nathalie Steunou
CNES Performance Lead

Date

Paper copies of this document may not be current and should not be relied on for official purposes. The current version is in the Product Data Management System (PDMS): https://pdms.jpl.nasa.gov/

This document has been reviewed and determined not to contain export controlled information.

April 7, 2017
JPL D-79084

National Aeronautics and Space Administration
Jet Propulsion Laboratory
California Institute of Technology

CHANGE LOG

DATE	SECTIONS CHANGED	REASON FOR CHANGE	REVISION
09/23/13	ALL	Initial release	Initial Release
2/1/14	ALL	Included derivation of the slope PSD in Appendix B; included ocean sigma0 section; expanded height and slopes sections for hydrology; expanded pointing error budget section; included section on correlation of systematic errors.	interim
3/13/15	ALL	Expanded measurement sampling discussion several corrections; several general additions.	interim
6/19/16	ALL	Expanded discussion on wet tropo errors	interim
3/17/17	ALL	Added section on motion errors for both ocean and hydrology; updated top level error budget tables; updated hydrology slope error budget and derivations; updated pointing error budget section; updated hydrology POD, hydrology classification sections (added discussion on surface water brightness, contrast, and temporal decorrelation).	Rev A

CONTRIBUTIONS

This objective of this document is to describe the overall performance and error budget of the SWOT mission. A document like this is never the outcome of a single person, but rather includes a very significant amount of work performed by a large team of people, in the form of discussions, exchanges, and analyses. In particular, the author would like to acknowledge the critical work and numerous direct contributions of Eva Peral, Ernesto Rodriguez, Nathalie Steunou, Curtis Chen, Shannon Brown, Brian Pollard, Dalia McWatters, Richard Hughes, Lee Fu, Clement Ubelmann, Bruce Haines, Shailen Desai, Dhemetrios Boussalis, Phil Callahan, and Brent Williams, among others, as well as thank the many users, science and engineering team members, and reviewers for their valuable comments and suggestions to improve the quality of this document.

Table of Contents

1 SCOPE

This document presents the top-down error budget for the SWOT mission and its ability to meet the scientific requirements. It includes all the different systems and subsystems that have a significant contribution to the overall performance of the mission. It is structured in several parts corresponding to the key error contributions for both oceanography and hydrology, with a discussion of the main contributors to the global performance: Flight System, Payload and Payload Instruments, S/C bus, Algorithms, and Mission System. The error budget presented in this document forms the basis for the performance requirements for the SWOT Mission levied across all these elements.

Note that unless explicitly noted, the error budget and its derivations as presented throughout the document correspond to 1-sigma values and allocations, as they flow down from the 1-sigma science requirements. The various sections therefore reflect the expected error contributions under controlled conditions (e.g. ocean waves of 2m Significant Wave Height, no layover conditions for lakes and rivers, etc.), as explicitly described in the science requirements. While in some cases the performance impact of exceeding those conditions is also presented, the general use-cases beyond these 1-sigma regions are beyond the scope of this requirement-focused document.

2 REFERENCES AND APPLICABLE DOCUMENTS

[1] SWOT Science Requirement Document, JPL D-61923.

[2] SWOT L2 Mission Requirements, JPL D- D-61935.

[3] Lee-Lueng Fu, D. Alsdorf, R. Morrow, E. Rodriguez, N. Mognard, Ed.: The Surface Water and Ocean Topography Mission. JPL Publication 12-05, February 2012.

[4] Vandemark, D., B. Chapron, J. Sun, G. H. Crescenti, H. C. Graber, 2004: Ocean wave slope observations using radar backscatter and laser altimeters. J. Phys. Oceanogr., 34, 2825–2842. doi: http://dx.doi.org/10.1175/JPO2663.1.

[5] Freilich, M.H. and P.G. Challenor, 1994: A new approach for determining fully empirical altimeter wind speed model functions. J. Geophys. Res., 99, 25,051-25,062.

[6] Chelton, D. (1994). The sea state bias in altimeter estimates of sea level from collinear analysis of TOPEX data. Journal of Geophysical Research 99: doi: 10.1029/94JC02113. issn: 0148-0227.

[7] Gaspar, P., Ogor, F., Le Traon, P. and Zanife, O. (1994). Estimating the sea state bias of the TOPEX and POSEIDON altimeters from crossover differences. Journal of Geophysical Research 99: doi: 10.1029/94JC01430. issn: 0148-0227.

[8] J.Y Cherniawsky, M.G.G Foreman, and et al. Ocean tides from topex/poseidon sea level data. Journal of Atmos. And Oceanic Tech.,18, 2001.

[9] F.Gatelli, A.M.Guamieri, F.Parizzi, P.Pasquali, C.Prati, and F.Rocca. The wavenumber shift in sar interferometry. Geoscience and Remote Sensing, IEEE Transactions on, 32(4):855–865, Jul. 1994.

[10] Feindt, F., J. Schröter, and W. Alpers (1986): Measurement of the ocean wave-radar modulation transfer function at 35 GHz from a sea-based platform in the North Sea, J. Geophys. Res., 91(C8), 9701–9708, doi:10.1029/JC091iC08p09701.

[11] William J. Plant, W.C. Keller, and K. Hayes, “Measurement of River Surface Currents With Coherent Microwave Systems”, IEEE Trans. On Geoscience and Remote Sensing, Vol. 43, No. 6, June 2005.

[12] Z. Chen, D. Chen, K. Xu, et al. Acoustic Doppler current profiler surveys along the Yangtze River. Geomorphology, Volume 85, Issue 3-4, p. 155-165. doi: 10.1016/j.geomorph.2006.03.018

[13] Tsang, L., J. Kong, and R. Shin, 1985: Theory of Microwave Remote Sensing. Wiley-Interscience, New York.

[14] Moller, D. and Esteban-Fernandez, D. (2014) Near-Nadir Ka-band Field Observations of Freshwater Bodies, in Remote Sensing of the Terrestrial Water Cycle, John Wiley & Sons, Inc, Hoboken, NJ. doi: 10.1002/9781118872086.ch9

[15] IEEE Standard Specification Format Guide and Test Procedure for Single-Axis Interferometric Fiber Gyros, Gyro and Accelerometer Panel of the IEEE Aerospace and Electronic Systems Society, 2008, New York, USA, ISBN 1-55937-961-8.

[16] A. Lamy and V. Tyrou, SWOT Mission Analysis, Ref: SWOT-TN-SYS-0162-CNES.

[17] OSTM/Jason-2 Science and Operational Requirements, Ref: TP3-J0-SP-188-CNES.

[18] Katsaros, K.B. 2015. Review of An Introduction to Ocean Remote Sensing, by S. Martin. Oceanography 28(1):174–176, http://dx.doi.org/10.5670/oceanog.2015.23.

[19] Jason-3 Products Handbook, Ref: SALP-MU-M-OP-16118-CN.

[20] Schaer S., Gurtner W., Feltens J., IONES: The IONosphere Map Exchange Format Version 1, Proceedings of the 1998 IGS Analysis Centers Workshop, ESOC, Darmstadt, Germany, February 9-11, 1998.

[21] T. Long, X. Dong, C. Hu and T. Zeng, "A New Method of Zero-Doppler Centroid Control in GEO SAR," in IEEE Geoscience and Remote Sensing Letters, vol. 8, no. 3, pp. 512-516, May 2011. doi: 10.1109/LGRS.2010.2089969

3 TERMINOLOGY AND ABREVIATIONS

ADC	Analog-to-Digital Converter
AMR	Advanced Microwave Radiometer
CoG	Center of Gravity
CoM	Center of Mass
EIK	Extended Interaction Klystron
EMB	Electro-Magnetic Bias
GPM	Global Precipitation Mission
ISLR	Integrated Side Lobe Ratio
LNA	Low-Noise Amplifier
OBP	Onboard Processor
POD	Precision Orbit Determination
POE	Precision Orbit Ephemeris
PRF	Pulse Repetition Frequency
PRI	Pulse Repetition Interval
RF	Radio Frequency
RSS	Root-Square Sum
RX	Receive (event)
SAR	Synthetic Aperture Radar
SNR	Signal-to-Noise Ratio
SRD	Science Requirements Document
SSB	Sea-State Bias
SSH	Sea Surface Height
SWH	Significant Wave Height
TRF	Transmit Repetition Frequency
TX	Transmit (event)
WSOA	Wide-Swath Ocean Altimeter

4 SWOT MEASUREMENT OVERVIEW

4.1 Introduction

SWOT will measure the water elevation of the global oceans, as well as terrestrial water bodies, to answer key scientific questions on the kinetic energy of the ocean circulation, the spatial and temporal variability of the world's surface freshwater storage and discharge, and to provide societal benefits on predicting climate change, coastal zone management, flood prediction, and water resources management.

The core oceanographic objective is to characterize the ocean mesoscale and sub-mesoscale circulation at spatial resolutions of 15 km and larger. Current altimeter constellations can only resolve the ocean circulation at resolutions larger than 100-200 km [3]. Fundamental questions on the dynamics of ocean variability at shorter scales, the mesoscale and sub-mesoscale processes, such as the formation, evolution, and dissipation of eddy variability (including narrow currents, fronts, and quasi-geostrophic turbulence) and its role in air-sea interaction, are to be addressed by these new observations. Global study of the circulation in the scales between 15 and 300 km are essential for quantifying the kinetic energy of ocean circulation and the ocean uptake of climate relevant tracers such as heat and carbon. The SWOT mission is the only available option to open a window on these dynamics.

SWOT will also target hydrology science objectives, by providing measurements of water storage changes in terrestrial surface water bodies and will provide estimates of discharge in large (50 m-100 m width) rivers, globally.

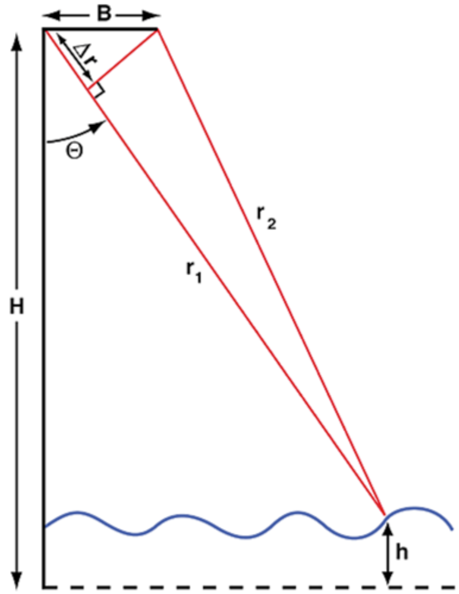

Figure 1. The interferometric measurement concept is basically triangulation. The baseline (mechanically stable) forms the base. The range is determined by the system timing accuracy, and the difference between the two sides, Δr, is obtained from the phase difference, φ, between the two radar channels.

The core instrument for SWOT is the Ka-Band Radar Interferometer (KaRIn) instrument, originally developed from the efforts of the Wide Swath Ocean Altimeter (WSOA). While conventional altimetry relies on the power and the specific shape of the leading edge of the return waveform, which is only available for the nadir point, the interferometric technique relies on the measurement of the relative delay between the signals measured by two antennas separated by a known distance (hereafter termed "baseline"), together with the system ranging information, to derive the height for every imaged pixel in the scene. For a given point on the ground, a triangle is thus formed by the baseline B, and the range distance to the two antennas, r_1 and r_2, which can be used to geolocate in the plane of the observation (see Figure 1). Using radar pulses transmitted from one of the antennas to form the interferometric pair (this operation mode is commonly referred to as "single transmit antenna"), the range difference between r_1 and r_2 is determined by the relative phase difference φ between the two signals as given by the following equation:

$$\varphi = 2kr_1 - k(r_1 + r_2) \approx kB \sin(\theta)$$

where θ is the look angle, and k is the electromagnetic wavenumber. From the phase measurement, and with precise knowledge of the range distance and the look direction θ, the height h above a reference plane can be obtained using the equation:

$$h \approx H - r_1 \cos(\theta)$$

where H is the platform height. The KaRIn instrument is complemented with the following suite of instruments:

- A dual-frequency (C- and Ku-band) Nadir Altimeter, similar to the Poseidon altimeter flown on the Jason series,
- A three-frequency microwave radiometer, similar to the Advanced Microwave Radiometer (AMR) flown on the Jason series,
- A DORIS receiver, a GPS receiver, and a Laser Retroreflector Array (LRA) for Precise Orbit Determination (POD).

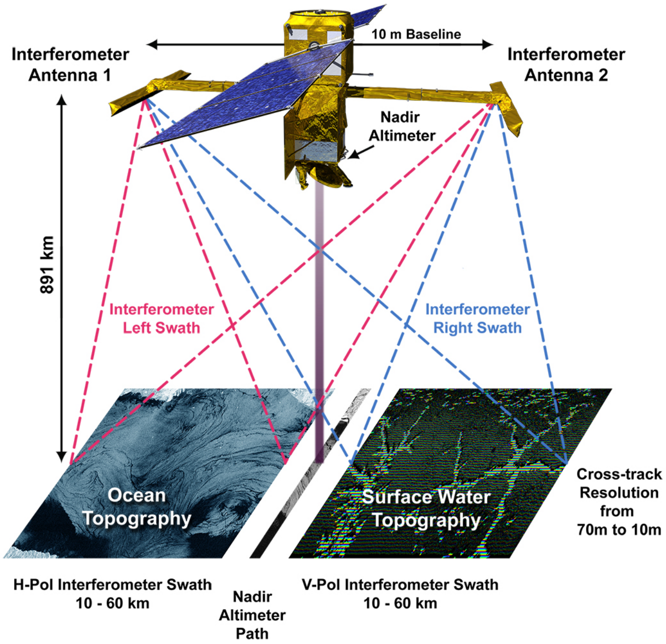

Figure 2. Conceptual illustration of the SWOT mission measurement concept. The Ka-band Radar Interferometer (KaRIn) illuminates two swaths of 50 km (±10 to 60 km on each side of the nadir track).

The figure on the left shows an artist's concept of the observatory with the antennas in the deployed state. In order to minimize the impact of tidal signals aliasing into the ocean topography data, while still covering important polar ocean areas, the satellite will operate during the nominal science mission in a 20.86-day repeat, non sun-synchronous orbit, at an altitude of 890.5 km and 77.6 deg inclination. An initial calibration phase 1-day repeat orbit is also established, at an altitude of 857 km and 77.6 deg inclination, with the main objectives of: 1) obtain fast-repeat ocean observations towards the calibration and validation objectives; and 2) understand the decorrelation times of the ocean mesoscale and sub-mesoscale processes, which are expected to suffer from relatively fast temporal decorrelations at the short ocean scales.

4.2 Ocean Measurement

For SWOT, the ocean measurement drives the required performance of the system, since centimetric accuracies are required to resolve sub-mesoscale processes. The high accuracy requirements for ocean topography measurements imply that the measurement error budget must be well understood and properly sub-allocated. The ocean measurement is conceptualized differently in two different wavelength regions: a) the region of wavelengths shorter than 1,000 km, where the fundamental topographic measurement is provided by KaRIn, as a swath measurement; and b) the region of wavelengths larger than 1,000 km, where the fundamental measurement is provided by the nadir altimeter as a nadir-only measurement.

In general, several sources of errors limit the accuracy of the final height measurement:

1) **Random errors.** These are errors related to the variance of the height (or phase) measurements, most notably the intrinsic noise of the interferometer, as well as other destructive

errors that increase the variance, and which cannot be corrected on the ground. The random error contribution depends on several factors, such as the system signal-to-noise ratio (SNR), the length of the interferometric baseline, and the processing algorithm. Additionally, it drives the pointing control stability of the observatory and the deployment accuracy and stability of the KaRIn antennas to minimize SNR loss over the desired swath on the ground.

2) **S/C and instrument systematic errors.** These are non-destructive errors typically associated with drifts or range variations that end up introducing bias in the measured heights, and which could be corrected if known. Some of the most important systematic errors are associated with a baseline roll, a change in the baseline length, and to range (or timing) and phase drift errors. Lack of knowledge in the spacecraft roll angle, changes in the baseline due to thermal contraction or expansion, system timing and phase drifts introduced by the antennas or the KaRIn electronics will induce height errors.

3**) Electromagnetic propagation (media), motion, and orbit errors.** The ranges measured onboard by the interferometer must be corrected to account for additional delays caused by propagation effects through the ionosphere and troposphere. These include wet and dry troposphere errors, as well as ionosphere errors, which include cross-track variations within the swath. While KaRIn will not directly measure the tropospheric and ionospheric signals, the SWOT radiometer will be used to obtain range corrections of the wet troposphere, which is the largest source of media errors. The dry troposphere and ionosphere signals at Ka-band constitute relatively small errors for the ocean scales of interest (ocean wavelengths < 1,000 km). Since they do not drive the error budget, they are allocated without requiring specific corrections during ground processing. In addition, motion errors due to mean ocean velocities and wave motion in the oceans will also introduce height biases, which cannot be corrected. Lastly, errors in the knowledge of the satellite and instrument radial positions will directly translate into height errors. The POD suite of instruments will be used to correct radial orbit errors.

4) **Wave-related errors**, such as Sea-State (also termed “electromagnetic”, EM) Bias (SSB) and significant wave height (SWH) related errors. The spatial variability of the wave and wind fields will introduce height biases.

The table below shows the science traceability matrix for oceanography, mapping the science objectives into science requirements, and in turn into instrument functional requirements.

Table 1. Science traceability matrix for oceanography

Science Objectives	Scientific Measurement Requirements	Instrument Functional Requirements
Measure mesoscale and sub-mesoscale activity, including: • fronts, eddies, and boundary currents; • eddy mean-flow interactions, eddy transports, and the role of eddies in climate; • physical-biological interactions and the role of eddies in the carbon cycle; • coastal tides and open ocean internal tides • and coastal currents.	• Monitor global mesoscale and sub-mesoscale activity (ocean wavelengths ranging from 15 km to 1,000 km) through the measurement of sea surface height (SSH) with a spatial resolution no coarser than 2 km x 2 km. • Global coverage of sea surface height measurements for ice free oceans (up to 74-78 deg latitude), with a repeat cycle of 21 to 23 days, with minimal tidal aliasing. • The SSH accuracy shall meet the	Ka-band Interferometer: • Height measurements with 2 km x 2 km resolution and ensemble average of the height error spectrum not to exceed the envelope listed in the SRD for wavelengths < 1,000 km • Provide above measurement accuracy over two swaths of 50 km each. Microwave Radiometer: • Resolve wet tropospheric correction.

• Estimate global change in mesoscale and sub-mesoscale dynamics at sub-monthly, seasonal, and annual time scales	envelope listed in the SRD.	Nadir Altimeter (Ku and C band): • Height measurement with Jason class performance. POD Suite: • Determine orbit.
	• 42 month operation for capturing 3 seasonal cycles and inter-annual variability.	• 42 month reliability

A high-level view of the flow of the key error budget components for wavelengths < 1,000 km is illustrated in the figure below, where KaRIn provides the basic height measurement. For simplicity, those elements that are pass-through are not shown.

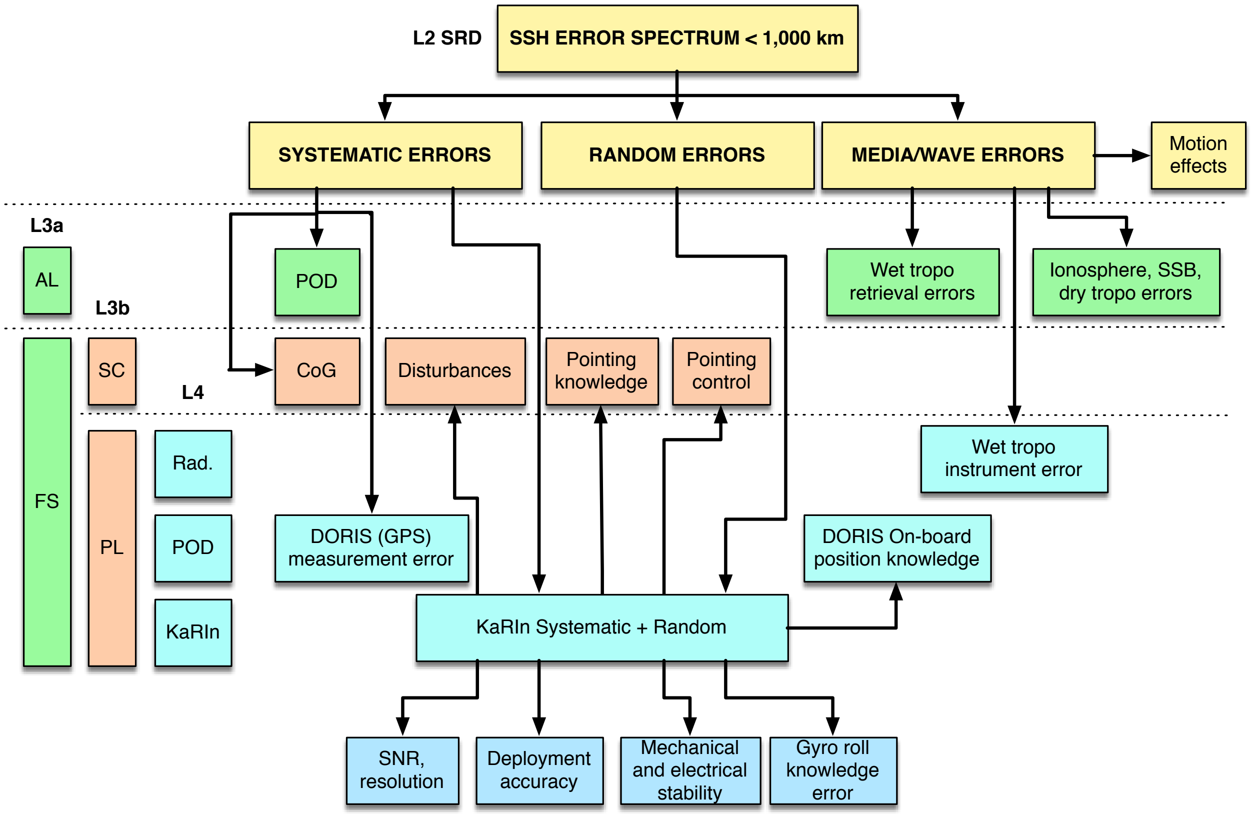

Figure 3. Overview of the key error budget components across levels for λ<1,000 km.

The Nadir Altimeter provides the measurements for wavelengths longer than 1,000 km, with a required accuracy equal or better than the Jason series of altimeters, radiometers, and POD.

4.3 Hydrology Measurement

Storage of water at and near the land surface is a key term in the terrestrial water balance, yet the dynamics, and even the amount, of water stored in lakes, streams, reservoirs, and wetlands globally is poorly known [3]. Furthermore, surface water stage and/or slope is a key measurement for derivation of streamflow, yet such measurements are currently only made at points via in situ methods, the spatial distribution of which is highly non-uniform, and mostly concentrated in the most populous parts of the developed world.

The primary SWOT hydrology science question relates to the global water cycle: "What is the spatial and temporal variability in the world's terrestrial surface water storage and discharge? How can we predict these variations more accurately?" The ability of SWOT to provide Water Surface Elevation (WSE), as well as freshwater discharge and storage change in lakes, reservoirs, wetlands, and rivers at the global scale, will provide a tremendous leap forward in understanding the dynamics of the land surface branch of the global water cycle. The second SWOT hydrology science question is: "How much water is stored on a floodplain and subsequently exchanged with its main channel? How much carbon is potentially released from inundated areas?" SWOT measurements will provide the means to study the nature of the floodplain hydraulics. A better understanding of the global water cycle would allow for a detailed investigation of linkages with the global Carbon cycle. The third SWOT hydrology science question is: "What policy implications would freely available water storage data have for water management? Can health issues related to waterborne diseases be predicted through better mappings?" For trans-boundary rivers, where water resources and flood risk management are international in nature, SWOT measurements of upstream reservoir levels could prove useful.

These science questions lead to the following key mission performance requirements, as specified in [1]:

a) The non-vegetated area of all water bodies greater than 250 m x 250 m, and rivers wider than 100 m must be measured with a relative error $\leq 15\%$ (1-sigma) of the total water body area.

b) The vertical precision of WSE measurements averaged over a non-vegetated area of 1 km^2 (lake, reservoir, wetland, and river) elevations must not exceed 10 cm (1-sigma)

c) The river slopes for river widths > 100 m must be measured to an accuracy of 17 μrad (1 cm/km) after averaging no more than 10 km downstream the river.

The table below shows the science traceability matrix for hydrology, mapping the science objectives into science requirements, and in turn into instrument functional requirements.

Table 2. Science traceability matrix for hydrology

Science Objectives	**Scientific Measurement Requirements**	**Instrument Functional Requirements**
• Determine surface water storage change and discharge to predict the land surface branch of the global hydrologic cycle. • Measure flood hydraulics. • Assess the role of fresh water storage as a regulator of biogeochemical cycles such as carbon and nutrients. • Estimate global storage change in terrestrial surface water bodies and global change in river discharge at sub-monthly, seasonal, and annual time scales	• Global monitoring of storage change by measuring changes in water body height and spatial extent with time for all bodies whose surface area exceeds (250m)^2 and rivers whose width exceeds 100 m. • Estimation of water mask extent to within 15% of body area. • Derivation of river discharge from measurements of slope and spatial extent within a hydrodynamic model assimilation. • Revisit time ~2 weeks in the tropics and less than 1 week in the Arctic (including ascending and descending orbits).	Ka-band Interferometer: • Height measurement for water bodies and rivers. • Slope measurement relative to surrounding topography. • Spatial resolution of 70 m postings or finer at the near-swath. • Provide above measurement accuracy over two swaths of 50 km each. POD Suite: • Determine orbit.
	• 42 month baseline operation for capturing 3 seasonal cycles and interannual variability	• 42 month reliability

4.4 KaRIn Overview

KaRIn is a synthetic aperture (“imaging”) radar interferometer operating at Ka-band (35.75 GHz center frequency). The key system parameters are shown in the table below. The antenna subsystem is formed by two 5 m long and ~0.3 m wide deployable antennas on opposite ends of a 10 m deployable boom (which forms the interferometric baseline). The antenna employs printed reflectarray technology, which is basically a flat panel with etched elements on its surface providing the phase change required to collimate the beam, emulating a parabolic reflector. This architecture enables stowage of the antenna to fit inside the launcher fairing, while structurally being low mass, to minimize the tip-mass for best overall baseline system stiffness.

Table 3. KaRIn Key System Parameters

Parameter	Value
Center frequency	35.75 GHz
TX Bandwidth (average)	200 MHz
TX Pulse length (baseline)	5.7 us
Pulse Repetition Frequency (average)	2 x 4420 Hz
Peak Transmit Power (EOL)	1,500 W
Physical Baseline Length	10 m
Antenna size	5 m x 0.25 m
Boresight Look Angle	+/- 2.65 deg
Polarization, Right Swath	VV
Polarization, Left Swath	HH

One of the antennas transmits, and both receive the radar echoes. The interferometer is a dual-swath system, alternatively illuminating the left and right swaths on each side of the nadir track (see figure below). This is accomplished by an offset dual-feed design operating with orthogonal linear polarizations (V and H polarizations), which enables each reflectarray antenna to generate two separate beams scanned ±2.65 deg off boresight, one at each polarization. The instrument’s spatial resolution in the direction parallel to the baseline direction (across the swath) is determined by the system bandwidth. With a 200 MHz transmit bandwidth, KaRIn will achieve ground resolutions in the cross-track direction ranging from approximately 70 m (at the near edge of the swath) down to 10 m (at the far end of the swath). As a synthetic aperture radar (SAR), the spatial resolution in the along-track direction (perpendicular to the baseline direction), is given by the length of the synthetic aperture that can be realized. The highest theoretical resolution that can be obtained is approximately given by half the antenna length, or 2.5 m. In practice, the resolution is determined by a combination of factors, including the antenna pattern, the azimuth bandwidth that is processed to achieve a desired ambiguity level (“contamination” level from adjacent pixels), and other design parameters, which make it closer to 2.63 m. In addition, the maximum resolution that can be synthesized will be in practice limited by the decorrelation time of the scene (the time for which the phase of the returns from a resolution cell is considered to be coherent, also referred to as coherence time). The decorrelation time needs to be longer than the integration time (the time of the synthesized aperture) in order to achieve azimuth resolutions close to the theoretical limit. Note that the decorrelation time only affects the achievable resolution and does not impact the accuracy of the interferometric measurement since, for a given swath, every echo pair observes the same realization of speckle noise.

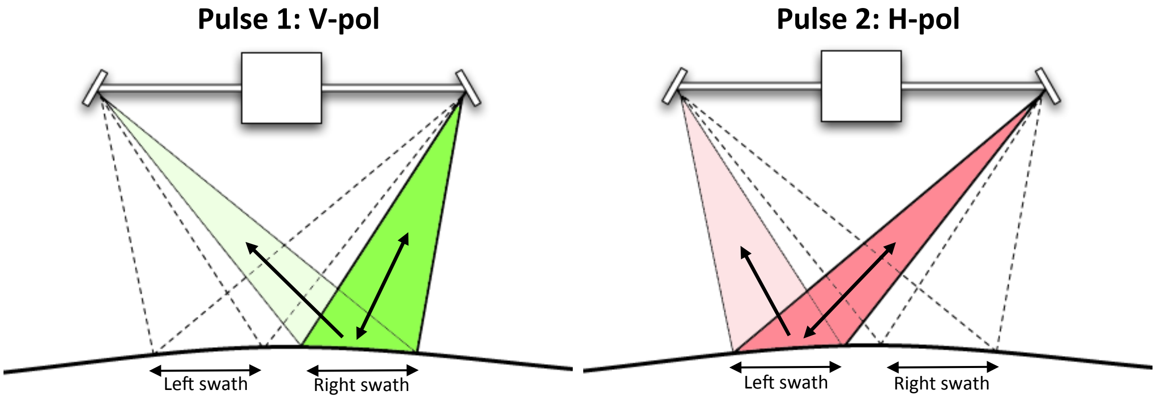

Figure 4. The timing sequence is formed by two pulses, interleaving left and right swaths. The left swath is imaged by a single pulse from the transmit antenna, followed by a pulse illuminating the right swath. The nominal pulse repeat frequency (PRF) is 4.42 KHz per swath, for a total transmit repetition frequency (TRF) of 8.84 KHz.

KaRIn's high resolution places high demands on the onboard storage and the downlink needs of the overall observatory. In order to reduce the output data rates and downlink volumes to fit within existing capabilities, KaRIn's digital subsystem performs onboard processing, which is discussed in the next section.

4.5 KaRIn Onboard processing overview

The KaRIn Onboard Processor (OBP) is integral to the overall functionality of the KaRIn system, performing a double duty for both surface water and ocean measurements:

1) Over land, the instrument performs standard SAR compression techniques: pre-summing by a factor of 2.125, resampling to the system bandwidth (200 MHz), and Block Floating Point Quantization (BFPQ) to 3 bits. The allocated output data rate for this mode is 349 Mbps.
2) Over the oceans, the instrument processes the incoming radar signal from an interferometric channel pair and generates a complex interferogram, as well as amplitude images for each channel, to be downlinked to the ground. The amplitude images for each channel enable estimation of the interferometric coherence on the ground. The onboard processor also performs multi-look averaging to decrease the data rate over the oceans before downlink. The OBP averages down to a resolution of $(500\text{ m})^2$ at 250 m posting, achieving a significant reduction in the data rate. The allocated output data rate for this mode is 17.1 Mbps.

At a high-level, the ocean algorithm (shown in the figure below) implements the following steps for each swath: a pair of received echoes (one echo from each antenna) are first processed independently; each is range compressed (i.e., a matched filter via an FFT in frequency domain), followed by sinc interpolation to co-register in time the echoes from both receive channels, and a spectral filtering to approximately flatten the phase and remove the non-common portion of the two spectra to minimize the coherence loss. This is accomplished by a two-step process: first, an opposite sign phase ramp is applied to each of the interferometric channels in the time domain to induce a frequency spectrum shift that aligns the spectral components of the interferometric channel pair (i.e. flattens the interferometric phase). Second, a FIR filtering is performed to remove the non-overlapping parts between channel spectra. This filtering is slowly adjusted along the orbit to account for mean sea surface (MSS) variations. The algorithm then takes 9 range-compressed lines, which are corner-turned and stored in memory since the next steps will operate in the azimuth direction, processing one range gate at a time. The azimuth processing implements a squinted unfocused azimuth SAR processing for each collection of range gates from a series of consecutive pulses. This effectively divides the real-aperture azimuth beamwidth into 9 separate sub-beams to maintain the number of looks, for an unfocused azimuth resolution of ~250 m. This step is accomplished by performing the complex multiplication of the 9 azimuth samples by 9 separate phase ramps that take into account the Doppler centroid (separately estimated by the algorithm, so as to relax what would otherwise be very stringent S/C pointing control or real-time knowledge requirements), to shift the Doppler spectrum to 9 different Doppler angles. The next stage in the algorithm is to compute the complex interferogram for each one of the 9 output beams by multiplying one channel by the conjugate of the other, as well as the amplitude images for each channel by multiplying each channel by its own complex conjugate. Finally, the algorithm performs multi-look averaging of each interferogram and the images power to achieve the required 500 m (along-track) x 500 m (cross-track) resolution at 250 m x 250 m posting.

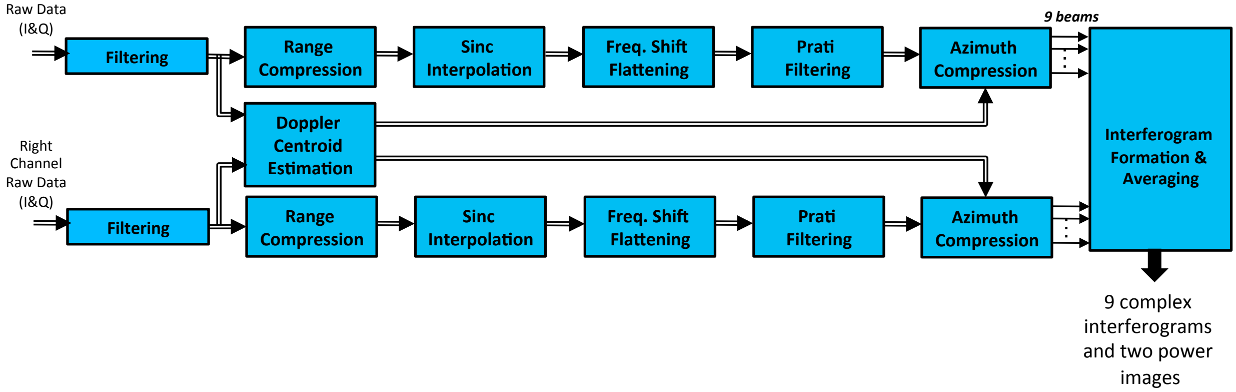

Figure 5. Basic steps of the KaRIn Onboard Processor for the oceans.

A raw data mode is also implemented in the KaRIn instrument, which can be selected by ground command, to enable the collection of raw Analog-to-Digital Converter (ADC) samples of the receive echoes for a continuous set of 2,800 pulses per swath (corresponding to a time duration of roughly 0.6 sec, or 4 km along-track). Ocean onboard processed data is also generated concurrently for downlink. The short duration of the raw-data mode is related to the fact that the instantaneous raw data rate is very high (close to 7 Gbps); since the rest of the Flight System is not able to cope with such data rate, it is buffered inside the instrument and output to the Solid State Recorded (SSR) at a not-to-exceed rate of 360 Mbps. The main objectives of this data collection mode includes support of the instrument commissioning activities related to the OBP (allowing for a direct comparison of the onboard processed data against the raw data being processed on the ground), as well as to support diagnose of on-flight anomalies. As such, it is conceived as an engineering data collection mode, and does not serve any direct science objectives.

5 OCEAN MEASUREMENT REQUIREMENTS AND ERROR BUDGET

As indicated in the previous section, the ocean requirements are formulated for two separate wavenumber regions, which will be fulfilled by a different combination of payload instruments. We first discuss the measurement requirement and error budget for ocean wavelengths below 1,000 km, followed by the error budget for the other wavenumbers.

5.1 Error budget for ocean wavelengths < 1,000 km

We define the Sea Surface Height (SSH) error spectrum, $E_{SSH}(f)$, as a function of the spatial frequency f (i.e., $f = 1/\text{ocean wavelength} = 1/\lambda$) (the spatial frequency is the same as the term of "wave-number" used in some oceanographic literature). The key oceanographic requirement for the SSH is thus specified as the error spectrum defined in the SWOT Science Requirement Document in units of cm^2/cycle/km as:

$$E_{SSH}(f) = 2 + 1.25 \cdot 10^{-3} f^{-2}, \qquad 15\,km < \lambda < 1{,}000\,km$$

The error spectrum is defined as an "ensemble average" (1-sigma) requirement, such that the expected SSH error variance in a wavelength interval $[\lambda_{min}, \lambda_{max}]$ is given by the integral of $E_{SSH}(f)$:

$$<(\delta h)^2> = \int_{1/\lambda_{max}}^{1/\lambda_{min}} E_{SSH}(f)\,df$$

The total SSH error science allocation over $\lambda = [15, 1{,}000 \text{ km}]$ integrates to 1.168 cm. Figure 6

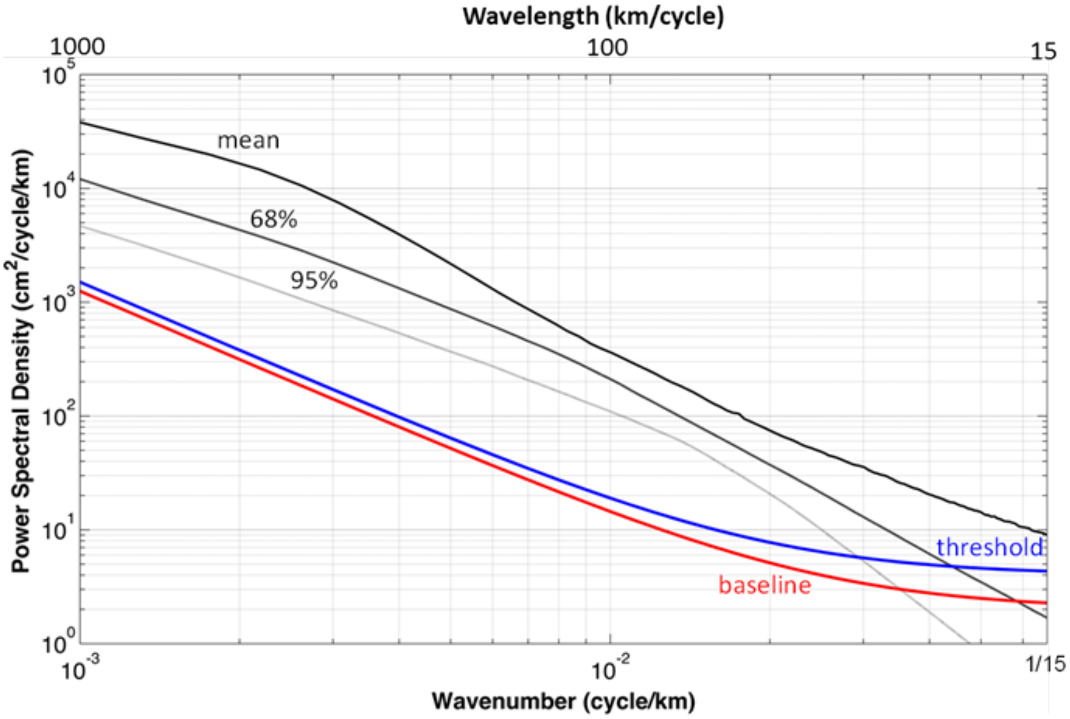

Figure 6. SSH error spectrum requirement (red curve) as a function of wavenumber, given by $E_{SSH}(f) = 2 + 1.25e - 3f^{-2}$. Also shown is the global mean SSH spectrum estimated from the Jason-1 and Jason-2 observations (thick black line), the lower boundary of 68% and 95% of the spectral values (upper gray dotted line and lower gray dotted lines, respectively). The intersections of the two dotted lines with the error spectrum at ~ 15 km (68%) and 30 km (95%) determine the resolving capabilities of the SWOT measurement. The threshold requirement is also shown (blue), which follows the expression $E_{SSH}^{threshold}(f) = 4 + 1.5e - 3\,f^{-2}$.

shows the error spectrum both for the science baseline and threshold requirements, where the latter one is defined as $E_{SSH}^{threshold}(f) = 4 + 1.5e - 3\, f^{-2}$ for $30\, km < \lambda < 1{,}000\, km$. Also shown in the figure are the global SSH signals in different percentiles estimated from Jason measurements (and extrapolated for wavelengths below ~100 km).

5.1.1 Measurement sampling

In order to translate the SSH spectral requirement into the payload's overall performance requirement, we need to first consider how to derive an instrument sampling error spectrum from the ocean wavelength error spectrum. The conversion of spatial frequency f into sampling frequency f_s for any given payload instrument is given by the amount of time that it takes to cover a given ocean wavelength λ, which is simply governed by the spacecraft ground speed. While the ground velocity changes slightly depending on the satellite's position along the orbit, we hereafter assume a constant (nominal) ground velocity of v_g = 6.5 km/s (the sensitivity of this parameter to small variations of the orbit altitude is not significant). Therefore, the relationship between spatial frequency and instrument sampling frequency is simply given by $f_s = v_g \cdot f = v_g/\lambda$. As a result, the 1 km ocean wavelength corresponds to 6.5 Hz, and the 1,000 km wavelength corresponds to 0.0065 Hz. The latter value corresponds to a sampling time of 153.8 sec, or 2.6 min. It is worth noting that this period of time corresponds to the time where the Flight System, and KaRIn in particular, needs to remain sufficiently stable to meet the overall SSH error spectrum.

To resolve up to a wavelength of 15 km, the data must be at least critically (Nyquist) sampled at 7.5 km. The SSH error spectrum requirement is specified as a single-sided along track spectrum of the swath-average performance (from 10 km to 60 km) after filtering the cross-track with an ideal square filter to 15 km wavelengths [1]. Considering that the two-dimensional dual-sided spectral density is related to the total height error variance simply by:

$$\sigma_h^2 = \iint_{-f_S/2}^{f_S/2} N_{2D}\, dA = N_{2D}^{dual-sided} f_S^2$$

and that the one-dimensional, dual-sided spectral density is then given by $N_{1D}^{dual-sided} = N_{2D}^{dual-sided} \cdot f_s$, the one-dimensional dual-sided spectral density becomes:

$$N_{1D}^{single-sided} = 2N_{1D}^{dual-sided} = 2N_{2D} \cdot f_s = \frac{2\sigma_h^2}{f_s^2} f_s = \frac{2\sigma_h^2}{f_s}$$

In this document, we will use the KaRIn standard deviation of the height error, σ_{cm} (expressed in cm), for 1 km^2 averaged pixels as the basis for most formulations. Therefore, the corresponding single-sided one-dimensional spectral density of the random noise for SWOT, N_{random} (in units of $cm^2/cy/km$), is finally obtained as:

$$N_{random} = 2 \cdot \frac{\sigma_{cm}^2}{\left(\frac{1cy}{km}\right)^2} \cdot \left(\frac{2}{\lambda_{min}}\right) \approx 0.267 \cdot \sigma_{cm}^2 \quad [cm^2/cy/km]$$

Note that not filtering (averaging) in cross-track wavelengths shorter than 15 km would mean that the along-track noise spectral density would increase by a factor of λ_{min} / 2 = 7.5. It is also worth noting that along-track averaging has no impact on the spectral density level of the white noise in the along-track PSD. This is due to the fact that in forming a pixel of 7.5 km in along-track, the variance is reduced because one has effectively filtered in the along-track spectrum all frequencies that are above the Nyquist frequency corresponding to the 7.5 km; however, it has not changed the level of the spectral density (and therefore it has no relevance with respect to the SSH spectral requirement). Therefore, the along-track averaging is only important if one is interested in finding the variance that a given pixel size would have, as it determines up to what frequency the noise density is integrated (obviously, larger pixel sizes will exhibit less variance due to the filtering of the random noise). This situation is not symmetric in the cross-track direction, since the variance in the cross-track direction is the basis to form the white noise density level that will then appear when one takes an along track spectrum. Therefore, in cross-track, averaging (or filtering) does have the ability to change the white noise density level in the along-track. And it is only in cross-track that the pixel needs to be averaged to 7.5 km (consistent with resolving 15 km min wavelength) to assess against the SSH requirement.

5.1.2 Shortest wavelength and aliasing considerations

An additional consideration arises regarding the shortest wavelength. While the science performance requirement is specified down to 15 km wavelength, the effective shortest wavelength requirement needs to extend to at least half the sampling frequency; for a 2 km posting requirement, it needs to extend to at least 1/4 cy/km. Currently, the OBP produces $(500\text{m})^2$ pixels, posted every 250m, with high frequency (>1/0.5 cy/km) errors being filtered in the process of obtaining the $(500\ \text{m})^2$ pixels. This sampling introduces aliasing of frequencies above 1/0.5 cy/km back into lower ones, as illustrated in the figures below. These aliased components can be removed later in processing since the posting meets Nyquist for the pixel size, i.e., a posting of 250 m for a $(500\ \text{m})^2$ averaged pixel. However, it is still crucial that no significant high frequency components appear around frequencies slightly larger than 1/0.5 cy/km, before the on-board filtering can sufficiently attenuate them during the filtering stage. In what follows, we will extend the requirement as a PSD through 1 cy/km, which correspond to a sampling frequency of 6.5 Hz (0.15 seconds). In practical terms, this is mainly relevant to bound systematic errors, although the random noise component is also filtered in the same way, with a -3dB point around 1 cy/km.

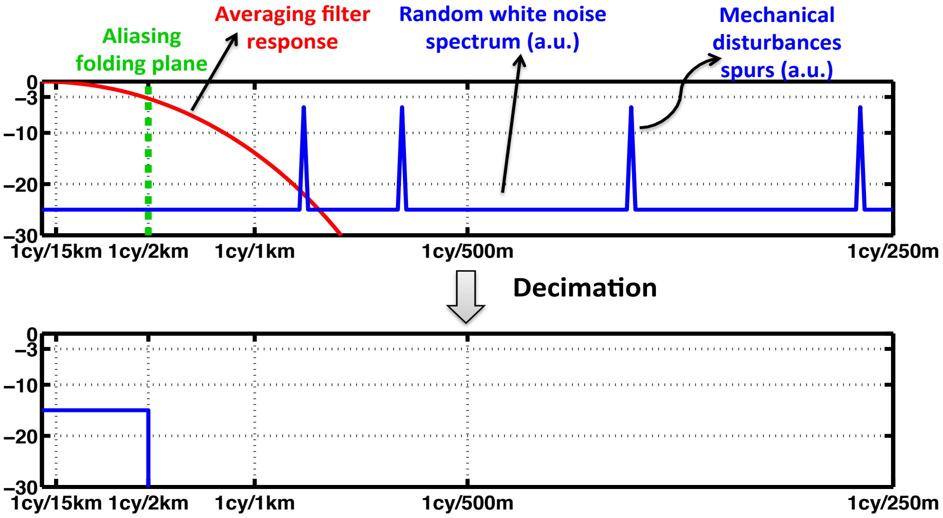

Figure 7. Illustration of high-frequency errors for $(1\ \text{km})^2$ pixels at 1 km posting. Above 1cy/2km, spurs should be greatly attenuated above the folding plane. Note spurs frequency and amplitude are merely notional.

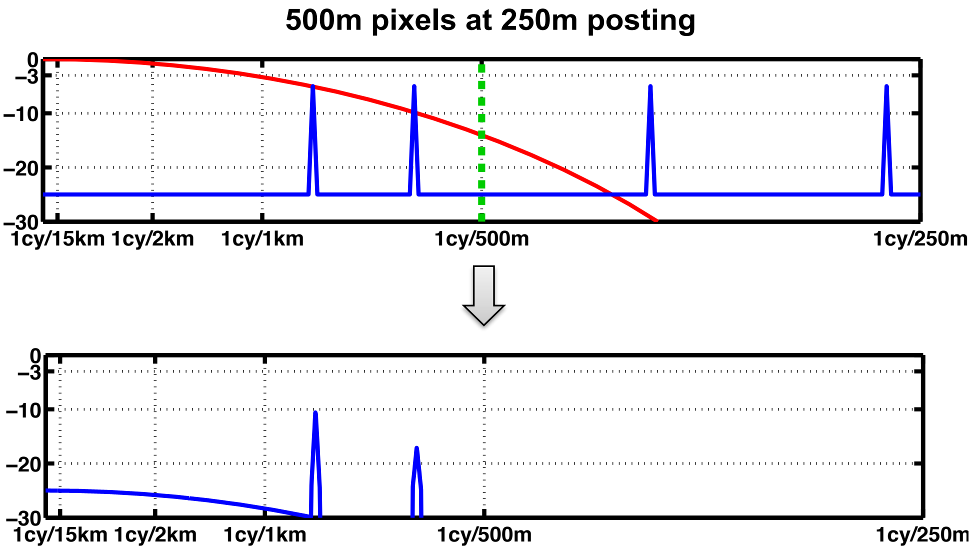

Figure 8. Illustration of high-frequency errors (top) at the pixel formation level, and (bottom) after decimation. for (500 m)^2 pixels at 250 m posting. Note spurs frequency and amplitude is merely notional.

In addition, it is worth noting that the filtering that is implemented onboard also has the effect of tapering the signal in a spectral sense; an ideal rectangular window would result in a sync function in frequency with a null right at 1 cy/km, and a -3dB taper at 1/2 cy/km. The tapering reduces at longer wavelengths, and is basically negligible (< 0.1 dB) at 1/15 cy/km, so it will not distort the spectrum of the SSH for the required range of wavelengths.

5.1.3 Error budget top-level break-down

A typical approach to establishing the interferometric error budget is to allocate a budget for each error source (systematic, random, media, etc.) at one or more points along the swath, where the root-square sum (RSS) of all the errors satisfies the overall height accuracy requirement. However, it is important to note that for SWOT, the science requirements define the error as a swath-average performance requirement, rather than specifying the performance at some point in the swath. Also, the spectral form of the science requirements effectively specifies the error requirement over different time scales (or, equivalently, spatial scales), as given by the SSH spectral power density error spectrum. Therefore, the allocation rationale that will be applied throughout the ocean error budget is as follows:

1) We first define that the direct sum of all spectral errors (random, systematic, media, motion effects, and radial error spectra), shall meet the required science error envelope, $E_{SSH}(f)$.
2) We define the KaRIn instrument standard deviation of the random error allocation as 2.5 cm, defined as a swath-average for an average 1 km^2 pixel, and for all wavelengths. This translates into a random error spectral density, $E_{random}(k) = 0.267*(2.5)^2$ cm^2/km/cycle = 1.67 cm^2/km/cycle.
3) We bound all the media, and radial errors by using error spectral envelopes. By subtracting all these spectral envelopes from the previous residual, one obtains the residual error that will be allocated to the systematic errors, E_{SYS} (k):

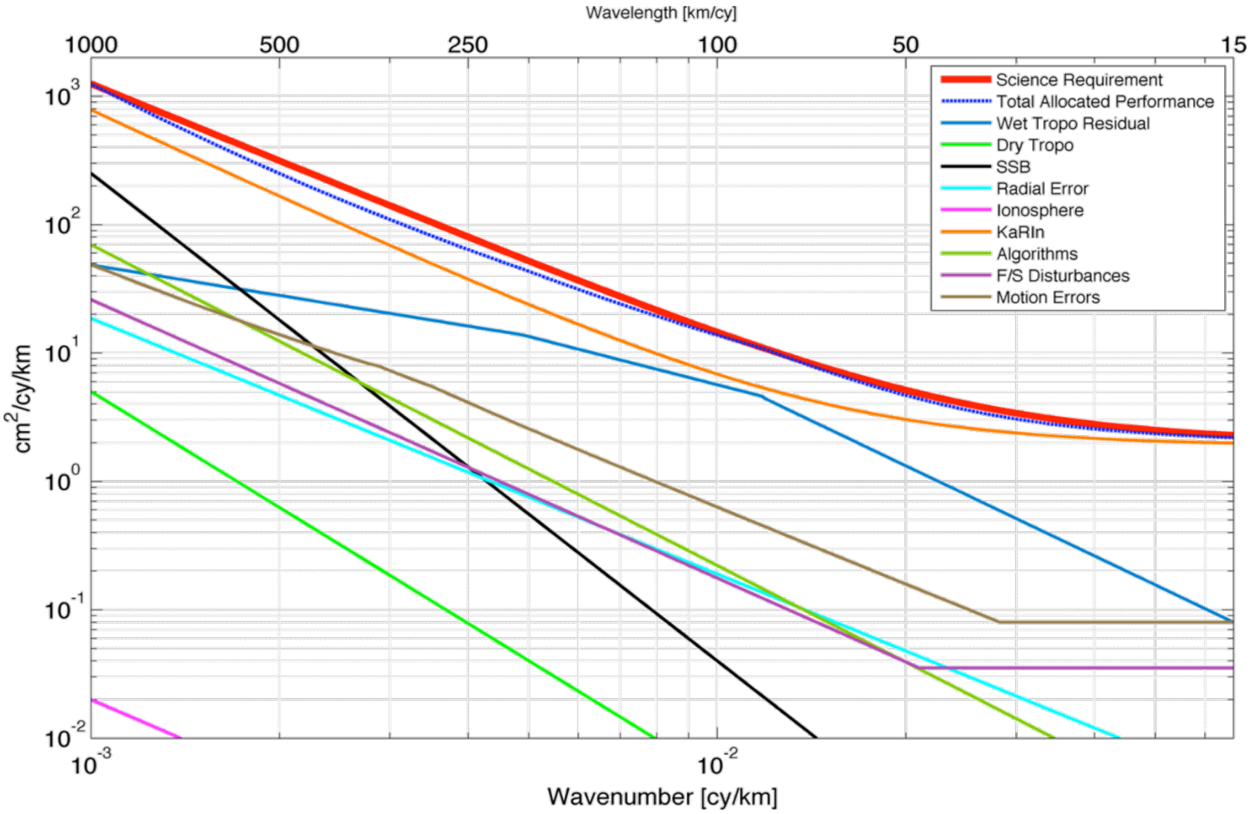

Figure 9. Break-down of the overall SSH error budget for spectral form for wavelengths < 1,000km. This includes all propagation, media, radial, and the sum of all KaRIn errors. Note the KaRIn measurement includes S/C contributions such as pointing and F/S disturbances.

$$E_{SYS}(k) = E_{SSH}(k) - E_{random}(k) - E_{wet\ tropo}(k) - E_{dry\ tropo}(k) - E_{SSB}(k) - E_{ionosphere}(k) - E_{radial}(k) - E_{motion}(k)$$

The sub-allocation of media and motion errors are presented in section 5.3. The discussion of radial errors is captured in section 5.5.6. F/S disturbances are discussed in detail in section 5.5. The algorithm error is presented in section 5.5.8.

The KaRIn allocation, including all KaRIn random and systematic errors is given by:

$$E_{KaRIn}(f) = 1.89 + 3.6153 \cdot 10^{-4} f^{-2} + 1.3236 \cdot 10^{-5} f^{-2.5}, \qquad f = [1\ km, 1{,}000\ km]$$

The figure below shows the KaRIn allocation as well as its break-down into its components: KaRIn systematic errors, KaRIn random noise, and the KaRIn gyro knowledge error. The sub-allocations of the KaRIn components will be discussed in detail throughout the following pages: in section 5.4 we describe the random noise in detail, and in section 5.5 we discuss the systematic errors (including the gyro knowledge error).

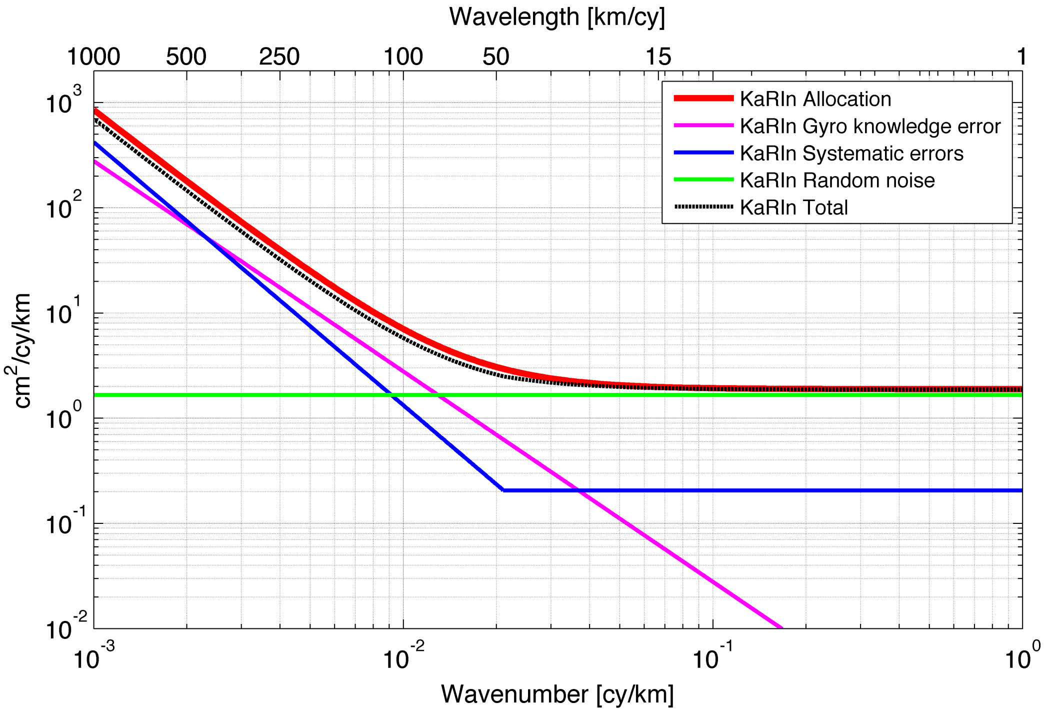

Figure 10. Break-down of the KaRIn errors in spectral form for wavelengths < 1,000 km.

Table 4. Top-level break-down of the SSH science requirement for ocean wavelengths < 1,000 km in an integrated form across two wavelength ranges.

Ocean Error Component < 1,000 km	**15-1,000 km [cm]**	**Comments**
Ionosphere signal	0.004	Integrated signal
Sea-State Bias signal	0.301	Integrated signal
Dry Troposphere signal	0.050	Integrated signal
Wet Troposphere Residual	0.426	After cross-track radiometer correction
Radial errors	0.140	Integrated signal
KaRIn Random errors	0.352	Integrated signal
KaRIn Systematic errors	0.798	Includes gyro errors
Algorithm errors	0.219	Processing/correction errors
Motion errors	0.247	Integrated signal
Total Allocated Error (RSS)	**1.078**	**Total error, as allocated**
Unallocated margin (RSS/SUM)	0.45 / 0.09	
Total (RSS) Sea Surface Height Error	**1.168**	**Requirement**

A break-down of the total SSH error budget for the most significant allocations as a fraction of the total SSH spectral requirement is presented in the figure below. It is worth noting that the unallocated margin is not constant throughout the entire wavelength region; for most wavelengths, the margins is larger than 10%, but it is slightly lower in a narrow region around 80 km due to the fact that the contribution of the wet tropo error peaks within that interval.

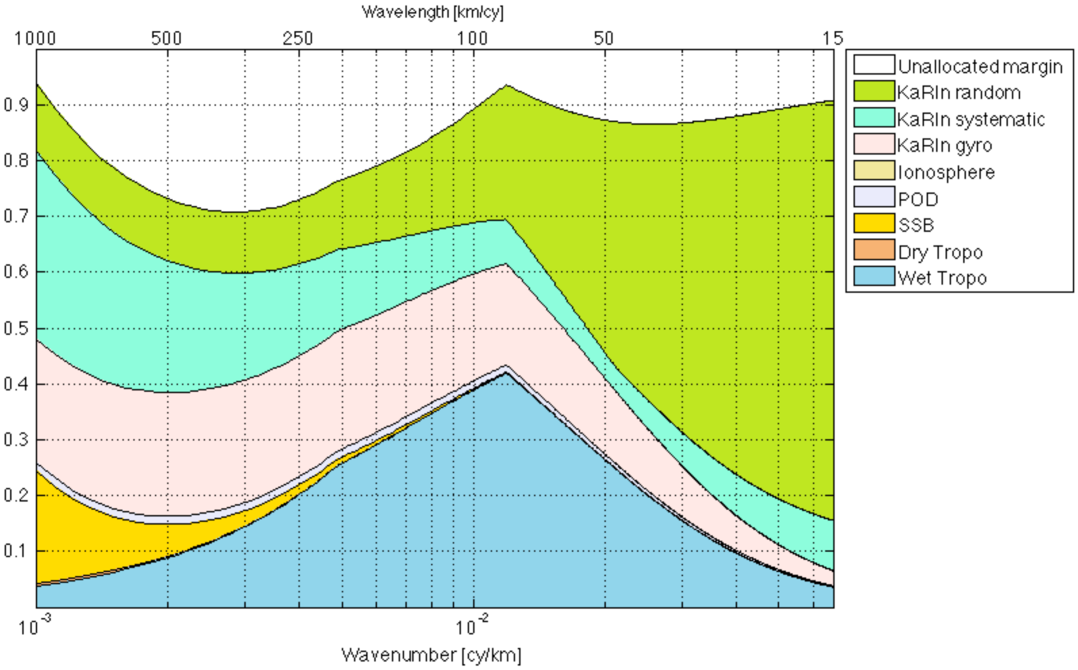

Figure 11. Stack-up of the most significant allocations as a fraction of the total SSH requirement as a function of wavenumber.

5.2 Error budget for ocean wavelengths > 1,000 km

As previously mentioned, the measurement of the SSH spectral region for ocean wavelengths longer than 1,000 km is performed by the nadir altimeter. The error budget is thus similar to the break-down of the Jason-2 (and Jason-3) GDR product [17]-[19], and shown in the table below.

Table 5. Error budget for ocean wavelengths > 1,000

Ocean Error Component > 1,000 km	**Error [cm]**
Ionosphere signal	0.5
Sea-State Bias residual (1% of SWH)	2
Dry Troposphere signal	0.7
Wet Troposphere residual	1.2
Radial Errors	1.6
Altimeter Noise	1.7
Total (RSS) Sea Surface Height Error	**3.4**

The performance in the table can be summarized as follows: the sea surface height shall be provided with a global and ultimate RMS accuracy of 3.4 cm (1-sigma) over 1 second averages along SWOT's ground-tracks for typical sea-state conditions of 2 m SWH and 11 dB sigma-naught. Note, however, that the SWOT allocation for the radial error component is 1.6 cm, rather than the 1.5 cm specified for the Jason series. This increased error sub-allocation is required for SWOT due to the much larger size of the spacecraft and the much lower altitude driving the uncertainty in the determination of the radial errors.

Finally, it is worth noting that, contrary to the error budget for SSH<1000 km, the nadir altimeter requires well-established model corrections to meet the media error allocations.

5.3 OCEAN MEDIA/WAVE ERROR REQUIREMENTS

This section presents a detailed discussion of the media errors and motion effects for ocean wavelengths shorter than 1,000 km.

5.3.1 Sea-State Bias

The Electromagnetic (EM) or sea-state bias (SSB) is a height bias that is introduced due to the varying reflectivity of wave crests and troughs, with wave troughs being better radar reflectors than wave crests at nadir. The mean scattering level is therefore shifted towards the wave troughs with respect to the true mean sea level, and for a standard altimeter, the range between the altimeter and the sea surface is overestimated. Also, the skewed distribution of wave heights with a median shifted towards wave troughs introduces another bias in measured sea level, which is referred to as skewness bias. Historically, the EM bias has usually been expressed as a fraction of the Significant Wave Height (SWH), which is traditionally defined as the mean wave height (trough to crest) of the highest third of the waves. Airborne observations carried out by Walsh et al. shows that the bias values are around 1% of the SWH at Ka-band, around 3% at Ku-band, and approximately 4-5% at C-band. While corrections can be calculated from models, we envelope the full SSB spectrum signal derived using the four-parameter BM4 parametric model for Ka-band, which is given by [6][7]:

$$\mathrm{SSB}(U, SWH) = (-0.021 - 0.0035 \cdot U + 0.00014 \cdot U^2 + 0.0027 \cdot SWH) \cdot SWH,$$

where U is the wind speed. This could be considered a rather pessimistic upper bound of the error, since it is not assumed that models (or retrieval estimates using Nadir Altimeter measurements) are used to reduce the error, as it is done for the Jason series of altimeters (reducing it from roughly 3% to 1% of the SWH). Instead, we consider the full signal because for KaRIn the incidence angle dependence of the SSB (over the swath) does not have the Jason heritage. A global analysis of the SSB based on the above model has been used to derive an envelope allocation of the SSB error spectrum, given by:

$$E_{SSB}(f) = 10^{-9} f^{-3.8} \ \ [cm^2/cy/km]$$

The integrated SSH error for wavelengths between 1 and 1,000 km for the envelope is 0.301 cm.

5.3.2 Motion effects

It is well known that for a SAR, a constant motion of a target on the ground will cause an apparent shift of its location in the SAR imagery due to the error associated to the knowledge of the relative velocity between the platform and the ground target. In other words, if the SAR processing assumes no motion of the ground target, which is the case for SWOT since the target velocity is not an observable, the target will appear shifted both along- and cross-track, along a contour of constant range distance (iso-range line) from the sensor. In addition, since the interferometric approach to retrieving the height relies on the reconstruction of the look angle, those shifts also translate in an error associated to the estimated phase, and therefore to the retrieved heights. While usually motion effects constitute a second-order effect for most applications, SWOT's required level of accuracy needs to account for this source of error.

In addition to height biases due to mean velocity shifts, an additional non-linear effect is introduced due to wave motion. This effect, termed *wave bunching*, fundamentally appears because the wave velocity, as seen by SWOT's near-nadir geometry, changes along the wave itself. Conceptually, this results in a spatially reshuffled wave topography, where the amount of azimuth shift is proportional to the line-of-sight velocity, and the end result is a non-linear distortion of the averaged heights.

In the following sections, we present first the height biases associated to mean velocity shifts, followed by a discussion on wave bunching, and the final error allocation for motion effects.

5.3.2.1 Height biases due to mean velocity shifts

This effect is easy to understand if one considers that SAR processing generally exploits the fact that the Doppler shift produced by any point on the surface as it travels through the antenna azimuth beam is described as if the point is stationary on the surface. For example, the Doppler frequency shift, f_d, produced by the relative motion of the sensor and a target, V_l, is $f_d = -\frac{2V_l}{\lambda}$. As illustrated in Figure 13, a point on the surface at the tip of vector R appears to be moving in the $-x$ direction with a velocity $-V$ to observers in this plane. The line of sight component along R is, to a good approximation, $V_l = -\frac{Vx}{R}$, and therefore the Doppler shift is $f_d = \frac{2Vx}{\lambda R}$. When $f_d = 0$, the target is directly perpendicular to the plane so we have located its azimuthal position. When the surface is moving, the Doppler shift produced by the relative motion of the plane and the moving target is given by $f_d = \frac{2Vx}{\lambda R} - \frac{2V_t sin\theta}{\lambda}$, where V_t is the component of the scatterer velocity in the y direction. Now, when $f_d = 0$, the position of the target is displaced by $x = R\frac{V_t}{V} sin\theta$.

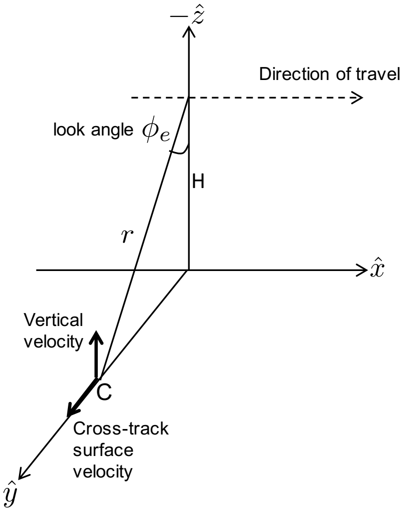

Figure 12. Illustration of cross-track surface velocity and vertical velocity vectors relative to the look angle at a point C in the swath. Note that the height of the platform, H, is approximately 900 km and the range of look angles for a swath of 10 to 60 km is approximately 0.4 to 4 deg.

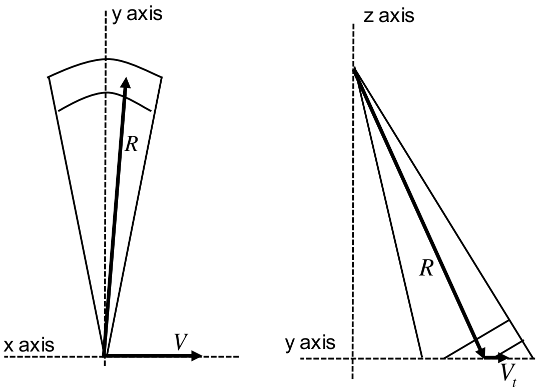

Figure 13. Illustration of a target at range R from the sensor, top view (left) and side view (right). Idealized velocity vectors of the platform with a surface motion of ($\boldsymbol{V}$) and the surface target ($\boldsymbol{V_t}$) are also shown. The platform is moving in the x direction, whereas the target is moving in the y direction.

Due to the SWOT geometry, it is convenient to separate the surface motion of the oceans into two distinct categories: a cross-track surface velocity (conceptually associated to a bulk velocity of the ocean surface), and a vertical velocity (associated to wave motion). Wave motions introduce vertical velocities due to the circular ("orbital") motion of the waves. Waves travel thanks to gravity pulling the water in the crests downward, and forced out from beneath the falling crests, the falling water pushes the former troughs upward, resulting in the waves moving to a new position. As discussed later in more detail, the velocity of the waves does not average out over SWOT's resolution scales due to the power weighting and phasing associated to crests and troughs in the radar return. While in the end both surface and vertical velocities couple in the same fashion into the radar as an observed radial velocity corresponding to the projection on the interferometer's look vector (i.e. a Doppler shift), as illustrated in Figure 12, the near-nadir geometry make their respective projections very different: surface velocities couple with a factor of $\sin(\theta_e)$, which is proportional to the cross distance to the range distance and is a relatively small factor (and would be 0 right at nadir), whereas vertical velocities induced by wave motion couple with a $\cos(\theta_e)$, which is a large factor (and would be 1 at nadir).

As previously discussed, with perfect platform attitude and for a broadside geometry, the net effect of a moving target is to introduce a Doppler shift that can be described as equivalent to an attitude error. Conceptually, this is simple to visualize since the cross-track component of the target velocity gives an apparent platform velocity heading error, ϕ_g, when focusing the moving target (see Figure 14). However, the presence of actual attitude errors in the satellite platform amplifies the motion effect and, in particular, the impact of a pitch error (a forward or backward movement of the antenna beams relative to an ideal broadside geometry associated to a rotation along the baseline axis) is far more prominent than that of a yaw (a rotation along the nadir axis) because of the relationship of the ground azimuth angle to pitch and yaw,

$$\phi_g \approx \frac{\alpha_{pitch}}{\sin\phi_e} + \alpha_{yaw} \approx \left(\frac{r}{C}\right)\alpha_{pitch} + \alpha_{yaw}$$

since, for SWOT, $\frac{r}{C} \approx 24$ at $C = 38\ km$.

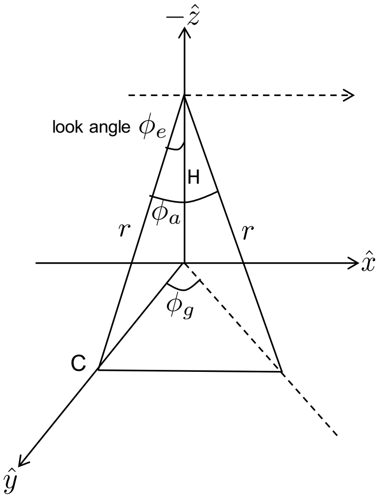

Figure 14. Illustration of the ground heading error $\boldsymbol{\phi_g}$ at a point C in the swath.

With perfect attitude and a perfect yaw-steered, undistorted baseline, the impact of surface motions for SWOT would be negligible. The Doppler shift caused by a surface cross track velocity, v_s, as high as 1 m/s would be $\Delta f_d = \frac{2}{\lambda} v_s sin\theta_e \approx 10\ Hz$, and a vertical velocity, v_r, of 10 cm/s would introduce a Doppler of $\Delta f_d = \frac{2}{\lambda} v_r \approx 24\ Hz$. These shifts correspond to about 0.5% of the Doppler bandwidth, and translate into an effective pitch of the look vector of $\alpha_{pitch} = \frac{\lambda \Delta f_d}{2\,v_p} \approx 0.7\ mdeg$, introducing height errors in the order of $\delta h_{surface\ velocity} \approx C\frac{v_s}{v_p}\alpha_{pitch} = 0.006\ cm$ and $\delta h_{vertical\ velocity} \approx H\frac{v_r}{v_p}\alpha_{pitch} = 0.015\ cm$, respectively, at the center of the swath. However, attitude control errors (particularly a pitch), can significantly increase the associated motion errors, given the previous equations. In the end, given that the platform height, H, is about 24 times larger than the cross-track distance C at roughly the center of the swath, and also given that as discussed later, the expected range of 1-sigma ocean surface velocities is ~0.2 m/s whereas the expected 1-sigma ocean radial velocity is ~0.1 m/s, generally speaking radial velocities associated to wave motion will dominate by an order of magnitude over surface velocities. For example, the overall pitch control error of 33 mdeg for the flight system (as will be discussed in the pointing error budget section) would introduce a height error of 0.7 cm for 10 cm/s of vertical velocity, whereas the same pitch error would introduce a height error of 0.06 cm for 20 cm/s of cross-track velocity.

In order to establish the range of velocities and bounds in the form of a PSD, an analysis of the ECCO-2 global model has been performed using the u and v components of the surface velocity from the model, extracted following the platform heading in the nominal SWOT orbit. The figure below shows the resulting PSD, as well as the cumulative density function of the surface velocities, for a surface velocity RMS of 0.2 m/s.

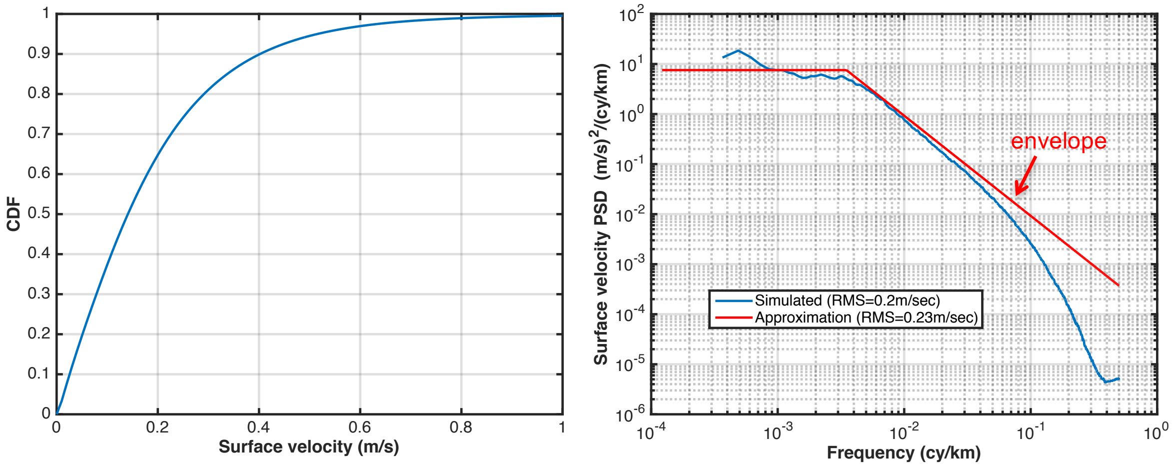

Figure 15. CDF (left) and PSD (right) of the ocean surface velocities from ECCO-2 model. Also shown is red is an envelope to the obtained spectrum. The RMS is ~0.2 m/s.

In order to characterize the PSD of the radial velocities, we need to consider first the effects of brightness modulations on the average height and the radial velocity for SWOT's viewing geometry. Starting with linear wave theory, the sea-surface elevation of a monochromatic wave traveling in the x direction is given by $h_s = \mathrm{a}\sin(kx - \sigma t) = \mathrm{a}\sin(\Theta)$, where σ is the wave frequency, and k is the wavenumber. The dispersion relation for deep water is given by $\sigma = \sqrt{g\,k\tan{(k\,d)}} \approx \sqrt{gk}$, where d is the water depth and g is the acceleration of gravity. Note that the SWH is thus given by $H_{1/3} = 4\sqrt{\langle h_s^2 \rangle} = 2\sqrt{2}a$. Now, following a geometric optics (GO) scattering model [13], the ocean radar brightness can be described by [4]:

$$\sigma_0(x) = \frac{R^2}{s^2(x)} e^{-\left(\frac{(\theta - \zeta_x)^2}{s^2(x)}\right)}$$

where $s^2(x)$ is the mean squared slope (mss), R is the reflection coefficient, θ is the incidence angle, and ζ_x is the large scale slope. As documented in the open literature, two types of brightness modulations appear:

1) a hydrodynamic modulation, which is dependent on the mean square slope (mss) of the

small waves,

$$s^{2(x)} = \bar{s_0}^2[1 + m_H \cos(\Theta + \phi_m)] \ ,$$

where $\bar{s_0}^2$ is the mean slope variance, m_H is the magnitude of the hydrodynamic transfer function, and ϕ_m is the phase of the modulation. Note how this modulation can be in phase with the height or the velocity depending on the modulation phase.

2) a tilt modulation, which is dependent on the local incidence angle and is modulated by large wave slopes. Mathematically, the tilt modulation results from expanding the exponential term above and considering the following expression in parenthesis:

$$e^{-\frac{(\theta-\zeta_x)^2}{s^2(x)}} \approx e^{-\frac{(ak)^2}{2s^2}} e^{-\frac{\theta^2}{s^2}} \left(1 - 2\frac{ak}{s}\frac{\theta}{s} sin\Theta + \frac{1}{2}\left(\frac{ak}{s}\right)^2 cos2\Theta\right).$$

   Note that in this case it is 90 deg out of phase with the heights and in phase with the velocity.

Given these different modulations, the total brightness modulation can be summarized as:

$$\sigma_0(x) = \overline{\sigma_0}\left(1 - m_H cos(\Theta + \phi_m) - 2\frac{ak}{s}\frac{\theta}{s} sin\Theta + \frac{1}{2}\left(\frac{ak}{s}\right)^2 cos2\Theta\right) = \overline{\sigma_0}M,$$

where $\overline{\sigma_0} = \frac{R^2}{\bar{s_0}^2(x)} e^{-\left(\frac{(\theta-\zeta_x)^2}{\bar{s_0}^2(x)}\right)}$ is the mean brightness according to GO, with $\bar{s_0}^2 = 0.019ln(U_{10})$ [4]. Given that the EM bias is always negative (since wave troughs are brighter than peaks), ϕ_m needs to be in the range of 90 to 270 deg. Consistent with existing observations at Ka-band (see e.g. [10]), $\phi_m \in [200{,}240]\ deg$, and since from EM bias research we expect a 3% EM bias, $m_H = 0.03\frac{4\sqrt{2}}{|\cos\theta_m|}$, which is in the range of 0.18 to 0.34 for ϕ_m between 200 and 240 deg.

Now, given that the wave surface velocity is expressed via its two components, the vertical orbital velocity ω and the horizontal velocity u,

$$v_r = \omega\ cos\theta - u\ sin\theta$$

the ensemble average brightness-modulated surface velocity for a 3% EM bias is thus given by:

$$\langle v_r\rangle_{\sigma_0} = \int_0^{2\pi} M\ v_r\ d\Theta = H_{1/3}\sigma\left(cos\theta\left[0.03\frac{sin\phi_m}{|cos\phi_m|} - \frac{ak}{2\sqrt{2}s^2}\theta\right] + 0.03sin\theta\frac{\cos\theta_m}{|\cos\theta_m|}\right) \ ,$$

and the ensemble average brightness-modulated sea-surface height is given by:

$$\langle h_s\rangle_{\sigma_0} = \int_0^{2\pi} M\ h\ d\Theta = -\frac{H_{1/3}}{4\sqrt{2}}\ m_H\ cos\phi_m$$

Using these results, an analysis was performed to obtain the PSD of the vertical velocities using a year of global WW-3 realizations. From the WW-3 runs, the primary wave mean wavelength and SWH is extracted, from which the two velocity components, ω and u, were computed under the assumption of a monochromatic wave, which are then used to derive $\langle v_r\rangle_{\sigma_0}$. The PSD of the vertical velocities is shown in the figure below, as is the CDF. The 68 percentile for SWH under 2 m is approximately 0.1 m/s for the worst case of 3% EMB and 240 deg of phase, and it is 0.16 m/s when considering all SWHs.

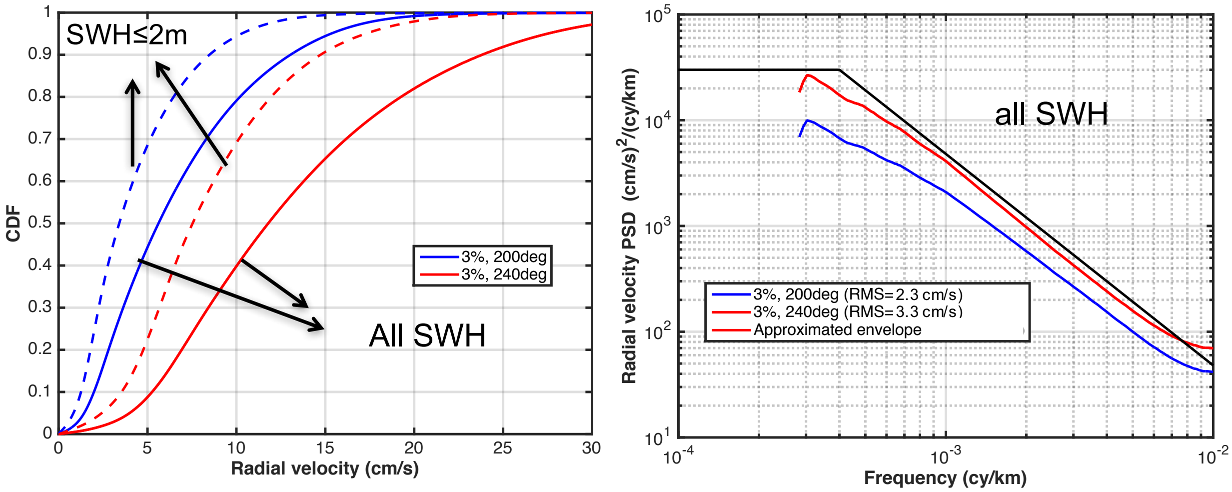

Figure 16. CDF of the radial velocities (left), both for SWH ≤ 2m and all SWHs and 200 and 240 deg of modulation phase; PSD of the radial velocities (right) for all SWHs and 200 and 240 deg of modulation phase, and the PSD envelope.

5.3.2.2 Wave bunching

Wave bunching is an additional effect associated to the fact that when scatterers have a distribution of radial velocities that differ in magnitude and sign, such as in the case of ocean waves, a non-linear re-positioning of the surface heights takes place with the interferometric SAR measurement (see figure below). These shifts in position are not negligible; a 1 m/s wave orbital velocity would create a shift of ~150 m, which is comparable to the wavelengths of the ocean waves. Because the resulting heights are reshuffled, the averaged pixels can present a significant height bias if the averaging is done at the height level.

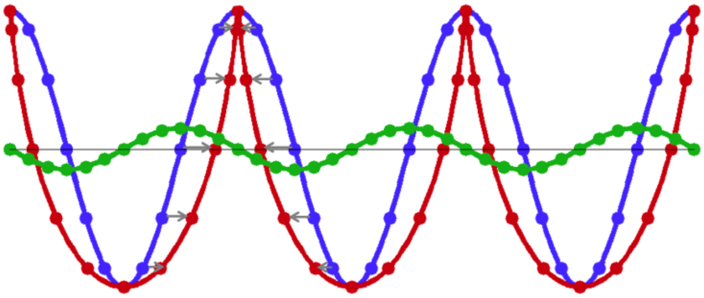

Figure 17. Conceptual illustration of wave bunching. A "true" monochromatic wave height is shown in blue, with a vertical velocity illustrated in green. As a result of the shift due to the different magnitude and sign of the vertical velocity, the apparent wave height is "bunched up" as illustrated by the red curve. In addition, the bunched peaks now have a higher density of points, whereas the troughs have lower density.

While accurately quantifying the impact of this effect for a particular case requires a specific analysis by simulation due to the severity of the non-linear effects involved, the wave-bunching analytical model adequately characterizes the impact for relatively weak bunching scenarios, and is particularly useful to reveal the non-linearities that are introduced. In this model, the resulting measured height spectrum, $S_M(k_x, k_y)$, is related to the Fourier transforms of the azimuth and range point target responses of the radar, $f_x(k_x)$ and $f_y(k_y)$, respectively, and the Fourier transform of the measurement impulse response, $\xi(k_x, k_y)$, which includes the sampling characteristics of the system, as follows:

$$S_M(k_x,k_y) = \left|f_x(k_x)f_y(k_y)\right|^2 \langle\left|\xi(k_x,k_y)\right|^2\rangle$$

where k_x and k_y represent the along-track and cross-track wavenumber, respectively. Expanding the previous expression reveals that the resulting measured height spectrum is related to the real spectrum, S_h, by the following expression:

$$S_M(k_x,k_y) = \left|f_x(k_x)f_y(k_y)\right|^2 \left[S_h + \left(2k^2\left|i\frac{r}{v_p}sin\phi\right|^2 (|\omega|^2 S_h)\right) \otimes S_h\right]$$

where r is the range distance, v_p is the platform velocity, ω is the spectrum of the vertical velocity, and ϕ is the angle of propagation of the waves relative to the sensor's trajectory (with 90 deg being perfectly aligned in the along-track direction). This result shows that the measured height spectrum is distorted by a term proportional to the convolution of the radial velocity spectrum and the true height spectrum. This term introduces leakage into the lower range of along-track frequencies, producing a spectral "hump" (an unexpected increase in energy within a certain range of frequencies in the measured SSH PSD). This is particularly important since the distortion is not necessarily confined to the range of wavelengths that correspond to the waves present in the scene (which would be filtered by the on-board processor); rather, it has the ability to propagate spectral distortions to lower frequencies, potentially impacting SWOT's range of wavelengths. It is also worth noting that the maximum distortion occurs when the waves are perfectly aligned in the along-track direction (ϕ=90 deg), and effectively vanishes when they are completely aligned in the cross-track direction (ϕ=0 deg).

However, the impact of wave bunching is relatively small for SWOT, primarily because the on-board processor averages to 500 x 500 m resolution the complex interferogram values instead of sample-weighted heights. This is important because averaging the complex interferogram takes into account the return power during the nominal course of computing the phase signal (whereas, for example, averaging heights does not), which minimizes wave bunching effects.

The figure below illustrates the resulting SSH error associated to a conservative wave bunching simulation for a 2 m SWH case, where waves of 2.8 cy/km are perfectly oriented in the along-track direction. The simulation considers the 500 x 500 m averaging resolution implemented on-board, as well as an additional cross-track averaging to ~3.5 km resolution (note that the SWOT requirement allows for an additional cross-track averaging down to 7.5 km). Even in this case, the error is an order of magnitude below the SSH PSD requirement of 2 cm^2/cy/km, decreasing rapidly for wavelengths longer than 1 km.

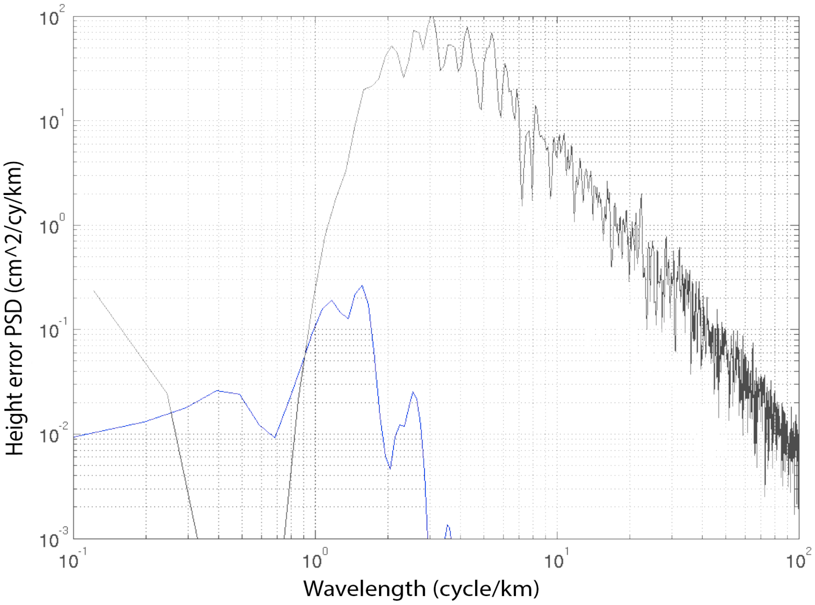

Figure 18. Conservative wave bunching simulation for 2.8 cy/km waves oriented at 0 deg and for 2m SWH. The black line represents the true spectrum of the waves, and the blue line the resulting wave bunching error for SWOT considering the 500 x 500 m averaging performed by the on-board processor, and an additional cross-track averaging to 3.5 km.

5.3.2.3 Overall motion error allocation

Considering the power spectral descriptions derived above for all of the above motion effects, i.e., surface velocities, radial velocities, and simulations of wave bunching, we derive here envelopes for the associated spectral height errors. The extension to PSD form of the height error formulations presented earlier of the surface and radial velocities in the presence of pitch and yaw attitude errors is given by:

$$E_{surface\ velocity}\ (f)=\left[\left(\bar{C}\frac{\alpha_{pitch}}{v_p}\right)^2+\left(\frac{\bar{C}^2}{H}\frac{\alpha_{yaw}}{v_p}\right)^2\right]E_{v_s}(f)$$

$$E_{vertical\ velocity}\ (f)=\left[\left(H\frac{\alpha_{pitch}}{v_p}\right)^2+\left(\bar{C}\frac{\alpha_{yaw}}{v_p}\right)^2\right]E_{v_r}(f)$$

where E_{v_s} and E_{v_r} are the spectra of the surface and radial velocities derived in the previous sections, and α_{pitch} and α_{yaw} are the pitch and yaw attitude errors as per the flight system pointing allocations described in the Pointing Error Budget section later in this document. It is important to note that in using the above expressions, we are considering that the attitude errors are fixed right at the requirement level; while this would be pessimistic in trying to derive an actual estimate of the expected impact, it does allow us to obtain an upper bound of the error that can be used to generate an allocation. In addition, it is also worth noting that the errors associated to yaw are second-order compared to those induced by a pitch, as shown in the figure below. The wave bunching error is enveloped by the results described in the previous section. Combining all these errors in spectral form allows us to obtain an overall bound, and therefore the PSD envelope allocation, in $cm^2/cy/km$, associated to the total ocean motion errors for 2 m SWH, which is given by:

$$E_{motion}(f) = \begin{cases} 4.1545 \cdot 10^{-4} \cdot f^{-1.6906}, & 0.001 \le f < 0.0029\ cy/km \\ 5.9002 \cdot 10^{-5} \cdot f^{-2.0246}, & 0.0029 \le f < 0.0282\ cy/km \\ 8.1 \cdot 10^{-2}, & 0.0282 \le f \le 0.0667\ cy/km \end{cases},$$

and is shown in the figure below. As discussed earlier, the error is dominated by radial velocities for a pitch error at the F/S pitch requirement level, and sits at about a factor of 20 lower than the science requirement.

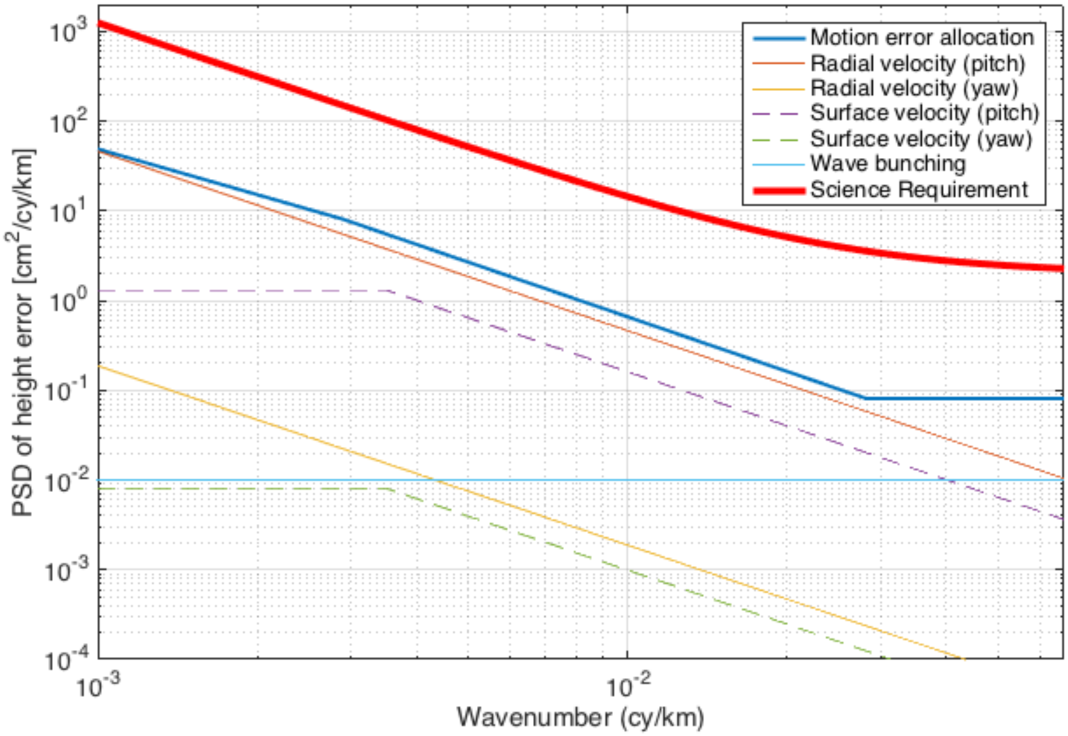

Figure 19. Allocation of the height error PSD associated to motion errors (blue line) and its break-down into the different error components. For reference, the overall science requirement is also shown (red curve).

5.3.3 Ionosphere

The ionosphere is a dispersive medium affecting the signal delay approximately proportional to the square of the radar wavelength, and includes long-wavelength effects due to variations in the total number of electrons (total electron content, TEC, where 10^{16} electrons/m^2= 1 TEC unit, or TECU) present along the radar path, as well as large to medium scale disturbances (traveling ionospheric disturbances, TIDs) and short wavelength effects due to small-scale TIDs and turbulences at the base of the ionosphere. The ionosphere introduces a group delay (range error) that is given by:

$$dh = \frac{40.3}{f^2} \int_0^H ds\, N_0(s)$$

where $N_0(s)$ is the electron density (in units of #/m^3), and f is the radar frequency. At the KaRIn frequency of 35.75 GHz, for a minimum solar cycle (20 TECU), the range error is roughly 7 mm, and for a near maximum solar cycle (~100 TECU) the range error is 33 mm. We have used the Ionex model [20] to derive an envelope for the ionospheric error spectrum over the global oceans, which is given by:

$$E_{ionosphere}(f) = 10^{-8} f^{-2.1} \quad [cm^2/cy/km]$$

The integrated SSH error for wavelengths between 1 and 1,000 km for the derived envelope is 0.004 cm.

5.3.4 Dry troposphere

The propagation velocity of an electromagnetic signal is slowed down by the "dry" gasses and the quantity of water vapor in the Earth's troposphere. The "dry" gas contribution is nearly constant and produces height errors of approximately -2.3 m. The gases in the troposphere contribute to the index of refraction. Its contribution depends on density and temperature. When hydrostatic equilibrium and the ideal gas law are assumed, the vertically integrated range delay is only a function of the surface pressure. The dry meteorological tropospheric range correction is equal to the surface pressure multiplied by -2.27 mm/mb. There is no straight forward way of measuring the nadir surface pressure from a satellite, so it is usually determined from model assimilated weather data from the European Center for Medium Range Weather Forecasting (ECMWF). The uncertainty on the dry tropospheric correction as an overall RMS is about 0.7 cm. We envelope the dry troposphere error spectrum from the results obtained from the Chelton model that is used to correct the Jason altimeter measurements, which is given by:

$$\text{Dry Tropo Correction} = -2.277 * \text{P}_{\text{atm}} * \left(1 + 0.0026 \cdot \cos(2 \cdot \text{latitude})\right) \quad [mm]$$

where P_{atm} is surface atmospheric pressure in mbar, phi is latitude. This results in an envelope error spectrum given by:

$$E_{dry\ troposphere}(f) = 5 \cdot 10^{-9} \cdot f^{-3} \quad [cm^2/cy/km]$$

The integrated SSH error for wavelengths between 1 and 1,000 km for the derived envelope is 0.05 cm.

5.3.5 Wet troposphere

While the spectral form of the wet tropospheric path delay is well known over the oceans from AMSR-E and Jason-1/2 measurements, the error of interest here is the residual to the corrections that the onboard radiometer will introduce. Let's first assume an isotropic 2D spectrum, $(f_s, f_c) = A_{2D} f^{-p}$, where $f^2 = f_s^2 + f_c^2$. For cases where p>1, the 1D single-sided spectrum can be obtained by integrating the 2D spectrum in the cross track frequency dimension (note a factor of 4 arises from the fact that we only integrate the positive side, and that this is the single-sided spectrum).

$$S_{1D}(f_s) = 4\int_0^\infty df_C A_{2D} f^{-p} = 2A_{2D} B\left(\frac{1}{2}, \frac{p-1}{2}\right) f_s^{-p+1},$$

where B(x,y) is Euler's integral of the first kind (beta function). To derive the overall error spectrum, we consider a 2D slope of p=8/3+1, which is consistent with all available observations from AMRS-E and the Jason-1/2 AMRs for wavelengths > 100 km. This results in a 1D wet tropo signal given by:

$$S_{wet\ tropo}(f) = 3.156 \cdot 10^{-5} f^{-8/3} \quad , \lambda > 100\ km$$

At scales shorter than 100 km, high-resolution measurements made by JPL's High Altitude MMIC Sounding Radiometer (HAMSR), indicate a slightly lower slope of -2.33, for a wet tropo signal given by:

$$S_{wet\ tropo}(f) = 1.4875 \cdot 10^{-4} f^{-2.33} \quad , \lambda \leq 100\ km$$

Given the signal, the residual swath-average error for a nadir-looking radiometer is the average over the swath of the signal minus the measured correction at nadir. In other words, the residual at an along-track point x and cross-track point C, is given by $\Delta h(x, C) = h(x, C) - h(x, 0)$. Since we want to arrive at the resulting PSD, we start by examining the autocorrelation function of $\Delta h(x, C)$, which is given by $R_{\Delta h}(x, C) = 2(R_h(x, 0) - R_h(x, C))$. Now we can exploit the fact that, assuming that the signal is stationary, the Wiener-Kinchine theorem establishes that the Fourier transform of the autocorrelation function is the PSD we are after. However, before doing that, we also need to account for the fact that the radiometer has a certain resolution, particularly in the cross-track direction (given by its beam pattern characteristics). The effect of that cross-track beam pattern can be modeled analytically by filtering the PSD of the signal with that pattern. Defining $W(C)$ as the window used to compute the swath-average performance,

$$\overline{R_{\Delta h}} = \int R_{\Delta h}(x, C)\, W(C) dC = 2\left(R_h(x, 0) - \int R_h(x, C) W(C) dC\right)$$

the PSD is thus given by:

$$E_{wet\ tropo\ swath}(f) = 2 \int df_c\, S_{wet\ tropo}(f)\big(1 - W(f_c)\big)$$

For a rectangular window, this further reduces to:

$$E_{wet\ tropo\ swath}(f) = 2 \int df_c\, S_{wet\ tropo}(f)\big(1 - sinc(2\, C_{max}\, f_c)\big)$$

where C_{max} corresponds to the maximum extent of the swath (60 km). For a single radiometer channel looking at nadir (such as for the Jason series of altimeter), the overall error over the swath would then be the sum of the contributions of the swath average error and the nadir radiometer error (including algorithm retrieval errors), ie:

$$E_{wet\ tropo\ nadir}(f) + E_{wet\ tropo\ swath}(f)$$

where the nadir error contribution is derived from analysis from models (MERRA, NCEP, and WRF), with an envelope given by:

$$E_{wet\ tropo\ nadir}(f) = \begin{cases} 9.5 \cdot 10^{-5} f^{-1.79}, 10^{-3} \leq f < 0.0023 \\ 0.036\, f^{-0.814}, 0.0023 \leq f < 0.0683 \\ 0.32, f \geq 0.0683 \end{cases}$$

which is shown in Figure 20. Since for scales shorter than 130 km, the total error exceeds the actual signal of the wet tropo (due to the fact that the radiometer nadir correction is not contributing information about the signal, but only adding as an uncorrelated signal), the retrieval needs to be filtered for frequencies higher than that intersection point.

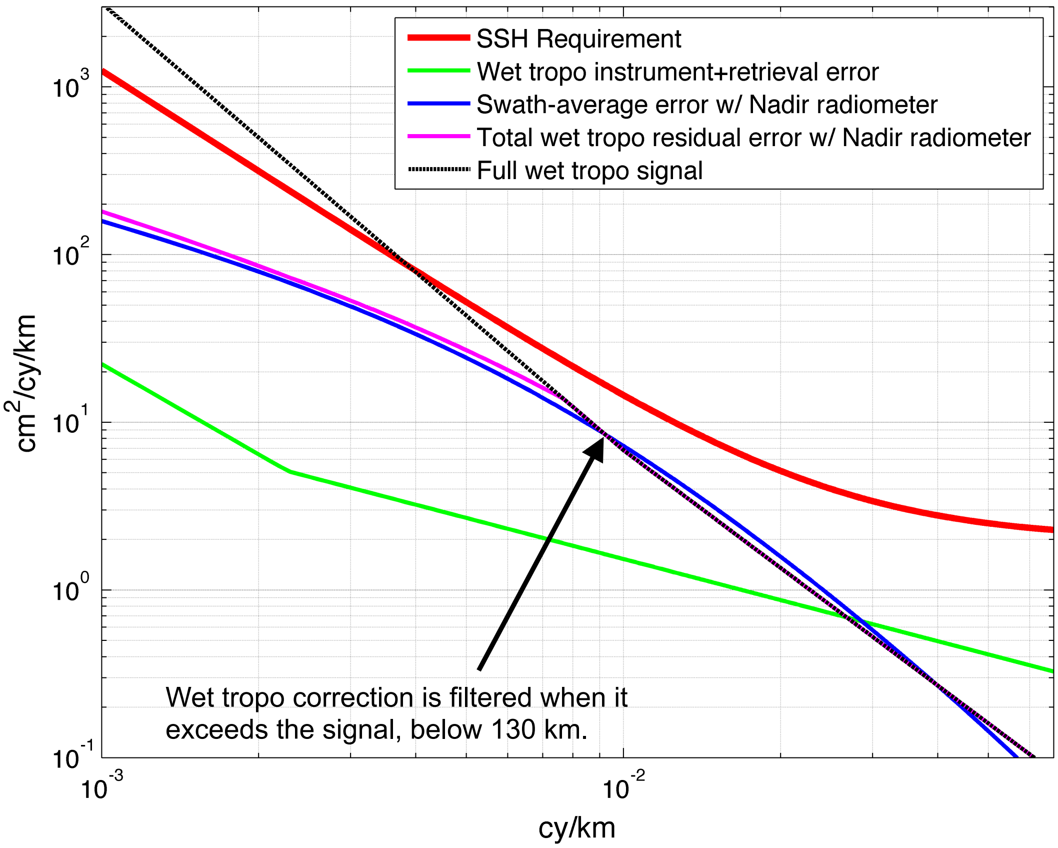

Figure 20. Break-down of the total wet troposphere errors for wavelengths up to 1,000 km for a nadir radiometer configuration (purple line): radiometer instrument + algorithm error (green line), and swath-average sampling error (blue line) that result from a nadir-based radiometer measurement in correcting KaRIn's 10-60 km swath. For reference, the full wet tropo signal (black line) and the total SSH requirement are also shown (red line).

The SRD, however, requires the implementation of a cross-track radiometer, which is a dual-channel (three-frequency) radiometer, where two measurements are collected at approximately +/- 40 km in the cross-track direction. This has the benefit of reducing the wet tropo swath average error and therefore the total wet tropo error contribution for wavelengths above 84 km, as shown in **Figure 21**. The final expression of the total wet tropo error for a cross-track radiometer implementation, including filtering the error for scales shorter than 84 km, can be approximated by three segments as follows:

$$E_{wet\ tropo\ total}(f) = \begin{cases} 0.205\, f^{-0.7911}, & f < 0.0049\,\dfrac{cy}{km} \\ 0.0179\, f^{-1.2492}, & 0.0049 \le f < 0.0119 \\ 1.448 \cdot 10^{-4} f^{-2.33}, & f \ge 0.0119 \end{cases}$$

The effective impact of a cross-track radiometer is therefore to reduce the wet tropo error integrated from 15 km to 1,000 km wavelengths from 0.62 cm to 0.426 cm, particularly reducing the errors around the wavelength region between 125 and 150 km.

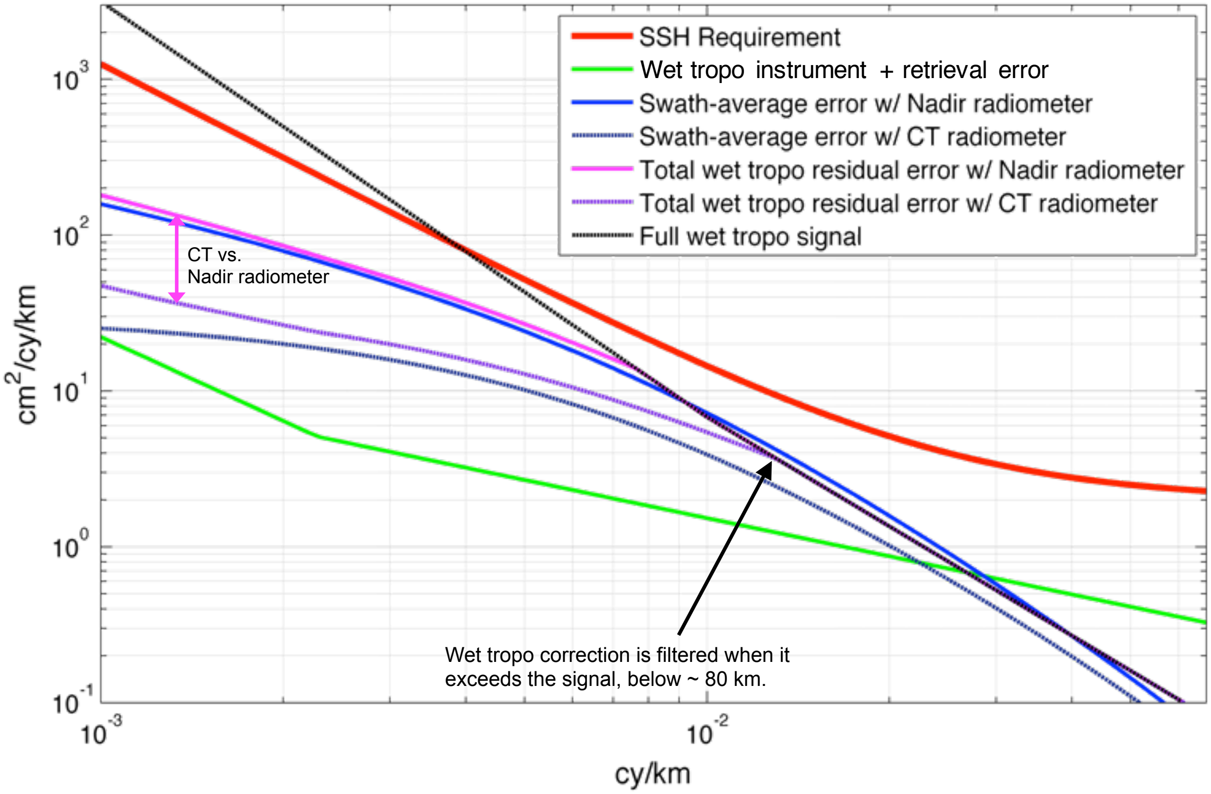

Figure 21. Wet-tropo total residual (dark purple line) and error break-down (instrument + retrieval error in green; swath average sampling error in dark blue) that would be achieved for a cross-track (dual-beam) radiometer measurement with two radiometric measurements performed at approximately +/- 40 km in the cross-track direction. For comparison, the errors associated to a nadir radiometer configuration are also shown. For reference, the full wet tropo signal (black line) and the total SSH requirement are also shown (red line).

Thus far we have considered that the instrument error incudes on the one hand errors that are truly intrinsic to the instrument as well as errors associated to the fact than even an ideal radiometer has a limited observation of the full wet tropo signal over KaRIn swath. That is, the radiometer is making two observations, on at the center of each swath, rather than imaging the full scene. However , hereafter we will consider this error a separate contribution, termed the *sampling* error. As a result, the sub-allocation of the wet tropo error actually separates three different components: the radiometer instrument error, the algorithm retrieval error, and the sampling error. Based on simulations, the sub-allocations to these three error components are as follows:

$$E_{wet\ tropo\ algorithm}(f) = \begin{cases} 5.669 \cdot 10^{-8} f^{-2.83}, & 10^{-3} \leq f \leq 5 \cdot 10^{-3}\ cm^2/cy/km \\ 2 \cdot 10^{-7} f^{-2.6}, & 5 \cdot 10^{-3} < f \leq 0.077\ cm^2/cy/km \end{cases}$$

$$E_{wet\ tropo\ instrument}(f) = \begin{cases} 2.86\ f^{-0.1977}, & 10^{-3} \leq f < 0.0023\ cm^2/cy/km \\ 3.1516 \cdot 10^{-2}\ f^{-0.9398}, & 0.0023 \leq f < 0.037\ cm^2/cy/km \\ 0.7, & 0.037 \leq f \leq 0.077\ cm^2/cy/km \end{cases}$$

$$E_{wet\ tropo\ sampling}(f) = \begin{cases} 2.6814\, f^{-0.2778}, 0.001 \le f \le 0.002 \\ 0.1403\, f^{-0.7527}, 0.002 < f \le\ 0.0035 \\ 0.04901\, f^{-0.9384},\ 0.0035 < f \le 0.0067 \\ 1.9991\ 10^{-3}\ f^{-1.5784}, 0.0067 < f \le 0.016 \\ 6.6514\ 10^{-4} f^{-1.846}, 0.016 < f \le\ 0.045 \\ 1.4\ 10^{-4} f^{-2.345}, 0.045 < f \le\ 0.077 \end{cases}$$

The figure below shows the break-down. The instrument error dominates the short scales (< ~ 100km), and the sampling error dominates the larger scales (>100 km). The retrieval error has the smallest contribution to the total error except for the largest scales (close to 1,000 km).

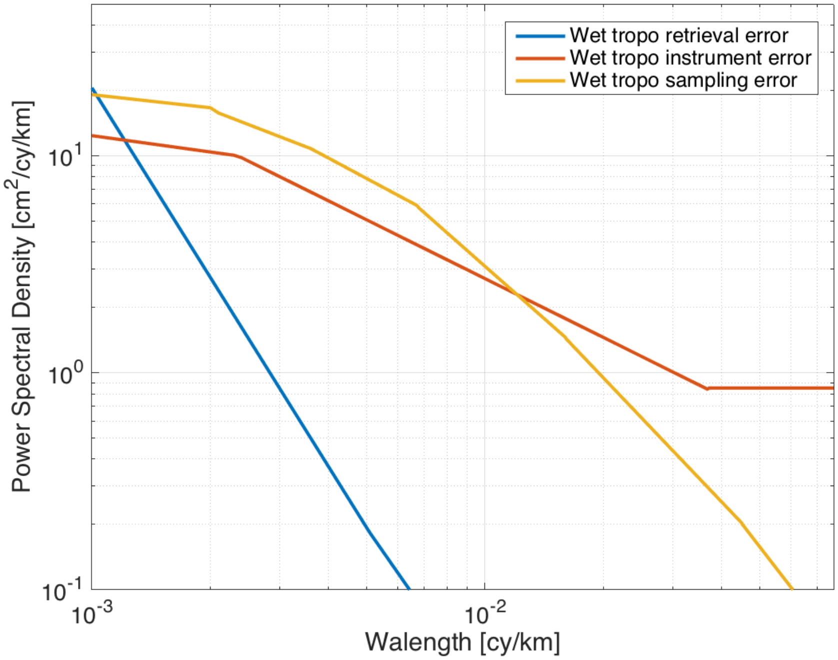

Figure 22. Break-down of the wet troposphere retrieval (blue), sampling (yellow), and instrument errors

5.4 OCEAN RANDOM ERROR REQUIREMENTS

Random errors ultimately limit the accuracy of the height measurement that is required to resolve sub-mesoscale processes. An estimate of the interferometric phase error is obtained by the correlation of the complex returns from the two antennas, γ. For homogeneous targets, it is well known that the maximum likelihood estimator of the interferometric phase is given by:

$$\hat{\phi} = \tan^{-1}\left(\frac{Im\left(\sum_{k=1}^{N_L} v_1^k v_2^{*(k)}\right)}{Re\left(\sum_{k=1}^{N_L} v_1^k v_2^{*(k)}\right)}\right)$$

where N_L is the number of looks to be averaged, and v_1 and v_2 represent the voltage returns from the same resolution element received from each antenna. The MLE estimator is unbiased and for a large number of looks, as is the case for KaRIn, the phase variance follows the Crameo-Rao bound, which is given by:

$$\sigma_\phi^2 = \frac{1}{2N_L}\frac{1-\gamma^2}{\gamma}$$

where N_L is the number of looks. This correlation coefficient is dependent on three key factors:

$$\gamma = \gamma_N \cdot \gamma_G \cdot \gamma_\varphi$$

where γ_N is primarily driven by the system thermal noise; γ_G is the geometric correlation factor, due to the cross-track phase variations within each pixel (including co-registration errors of the two returns); and γ_φ is the angular (or volumetric) decorrelation. Note that there are additional decorrelation terms, such as those introduced by a common group delay, but they are very small and introduce negligible decorrelations. The main correlation terms are discussed hereafter; a high-level flow of its key components is shown in the figures below.

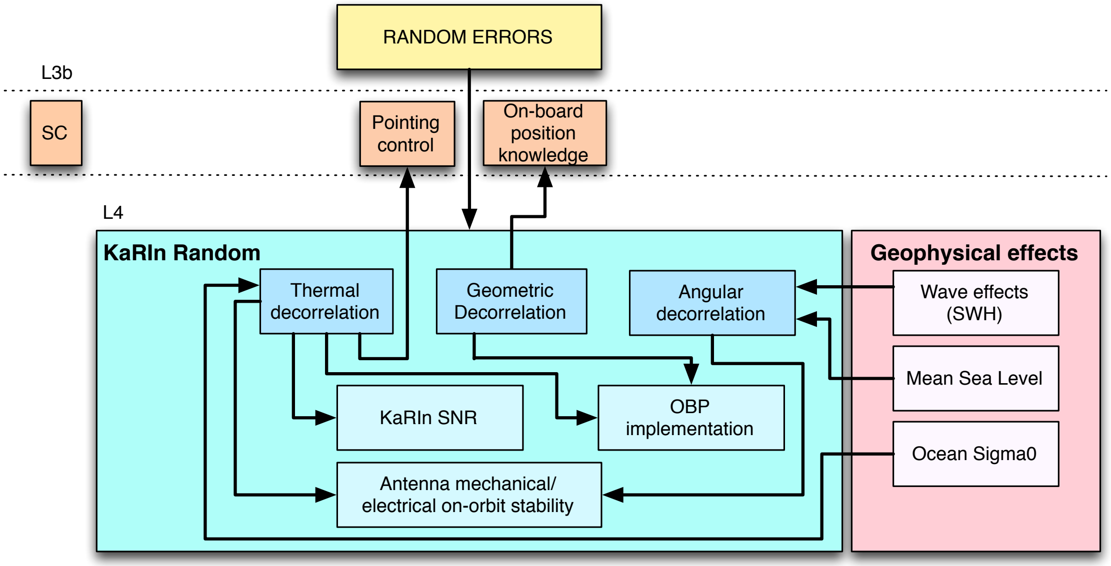

Figure 23. Conceptual high-level flow-down of the random errors to the key mission elements.

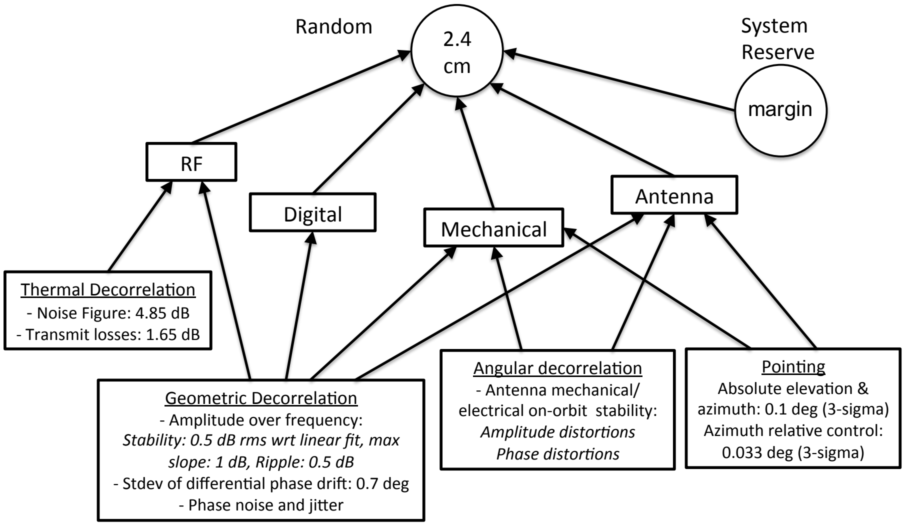

Figure 24. Flow-down of the random error requirements to the different KaRIn elements.

The errors associated to pointing are discussed in a separate section.

5.4.1 Ocean backscatter

The backscatter (sigma0, or σ^0) of the ocean at Ka-band is derived from the Vandemark model [4], which parameterizes the backscatter as the following function of wind speed:

$$\sigma_{ka}^0 = \frac{|R(\theta)^2|}{mss'_{Ka}} \sec^4(\theta)\, e^{-\frac{\tan^2\theta}{mss'_{Ka}}}$$

where θ is the incidence angle, $|R(\theta)^2|$ is the Fresnel reflectivity factor (with $|R(\theta)^2|$=0.52), and mss'_{Ka} is a radar derived estimate of the surface wave slope variance (mss), which is parameterized as a function of the wind speed percentile, p, following the rayleigh global wind speed function derived by [5]:

$$mss'_{Ka} = 0.019 \log\left(8.35\sqrt{-\,log(1-p)}\right)$$

The figure below shows the sigma0 over the KaRIn swath for three percentile cases, where the 68% is used hereafter in the SNR computations.

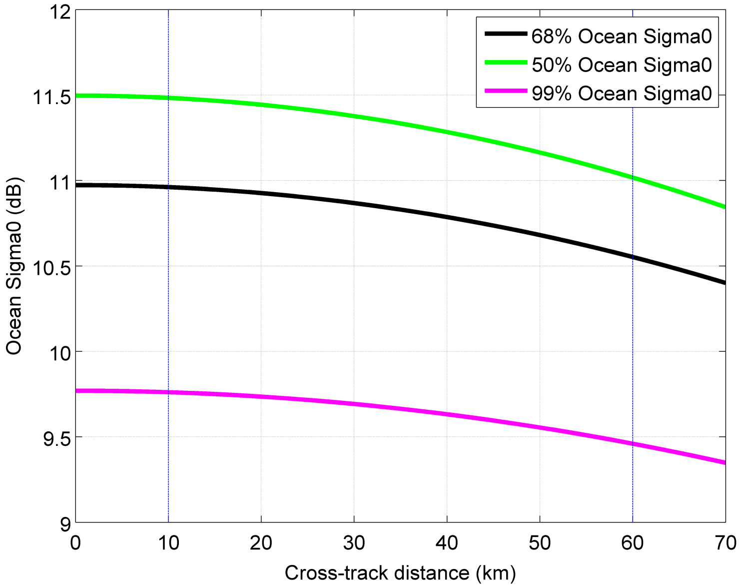

Figure 25. Ka-band Sigma0 as a function of cross-track distance for 68%, 50%, and 99% wind speeds.

The figures below show the global ocean wind speed PDF derived from a full year of Cross-Calibrated Multi-Platform (CCMP) ocean surface wind velocity L3.0 product and the resulting PDF of nadir sigma0's derived from these wind speeds.

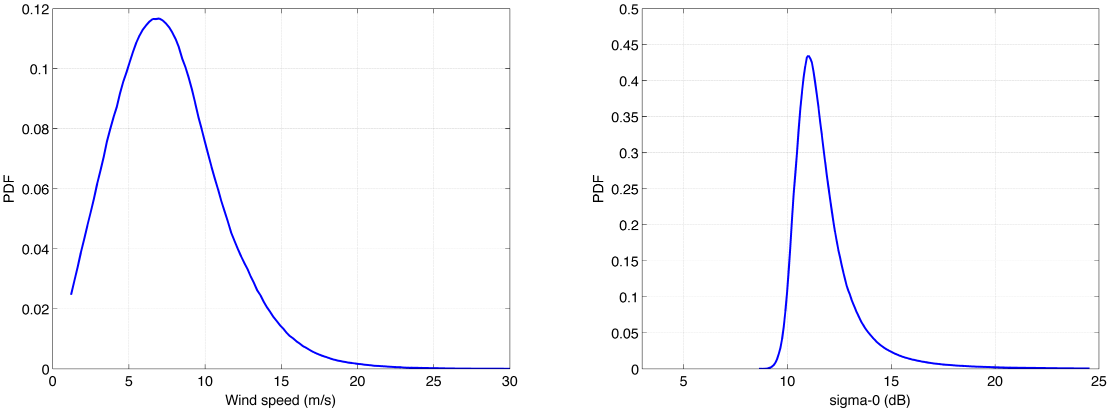

Figure 26. (left) PDF of the global ocean wind speeds from the CCMP product; the median value (50 percentile) corresponds to a wind speed of 7.4 m/s, and the 68 percentile to 8.9 m/s; (right) PDF of the sigma0's at nadir (0 deg incidence) derived from the ocean wind speeds using the Vandemark model described above. The 50 percentile corresponds to 11.4 dB, and the 68 percentile is 11 dB.

At a global scale, the ocean sigma0 levels predicted by the model are in agreement with the recent observations obtained by SARAL/AltiKa, as shown in the figure below, as well as to the comparisons with GPM at nadir.

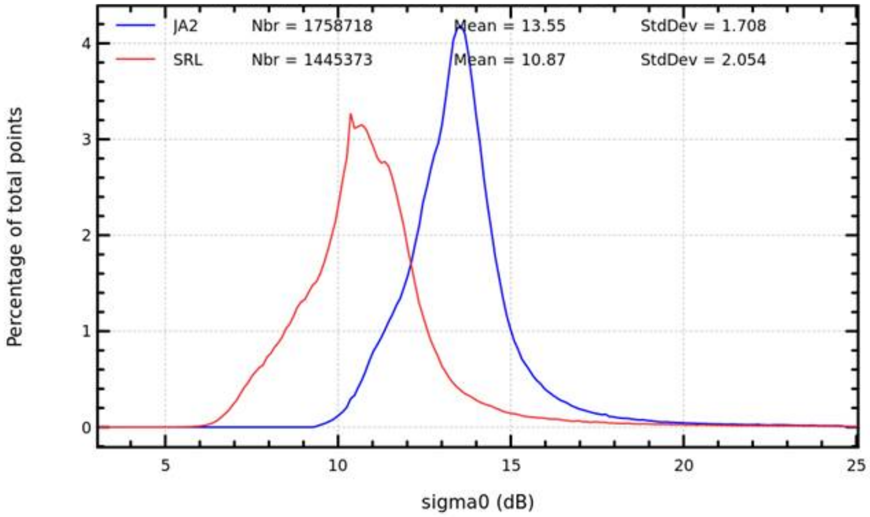

Figure 27. Histogram of the attenuation-corrected sigma0's (red) measurements taken by AltiKa from 06/27/2013 through 08/01/2013, and (blue) measured by Jason-2 (figure courtesy of CNES) for latitudes between -66 to +66 degrees. The mean ka-band sigma0 measurements is 10.87 dB.

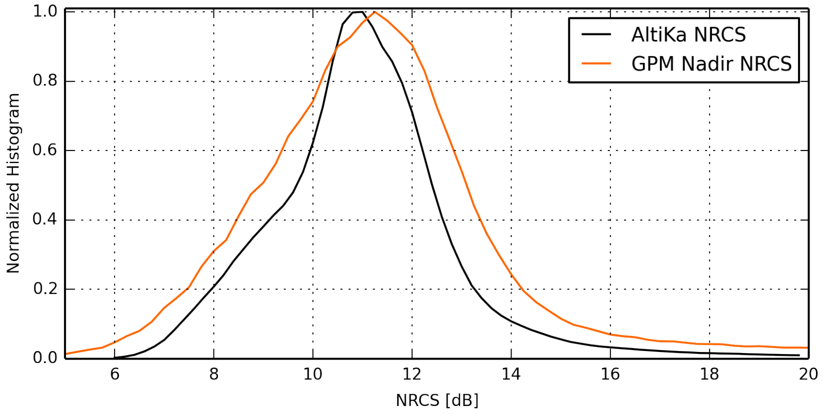

Figure 28. Comparison of calibrated Ka-band sigma0's from the Global Precipitation Mission (orange) and AltiKa for the same time period (roughly expanding 1.5 years of observations), showing excellent agreement between both sensors at Nadir to within ~0.25 dB.

5.4.2 Thermal decorrelation

As with any interferometric radar system, the thermal noise in the return signal cause the interferometric phase to contain random errors as described by the thermal correlation, γ_N, which includes the finite signal-to-noise (SNR) ratio available to the radar system, and other effects such as the degradation of the radar point-target response due the nominal antenna and variations along the orbit, Doppler centroid estimation errors, and pointing control errors. The thermal correlation factor, γ_N, taking into account all these factors, is given by:

$$\gamma_N = \frac{1}{1 + SNR^{-1}}$$

The Noise Equivalent Sigma0 (NES0) for the ocean, including margins, is shown below.

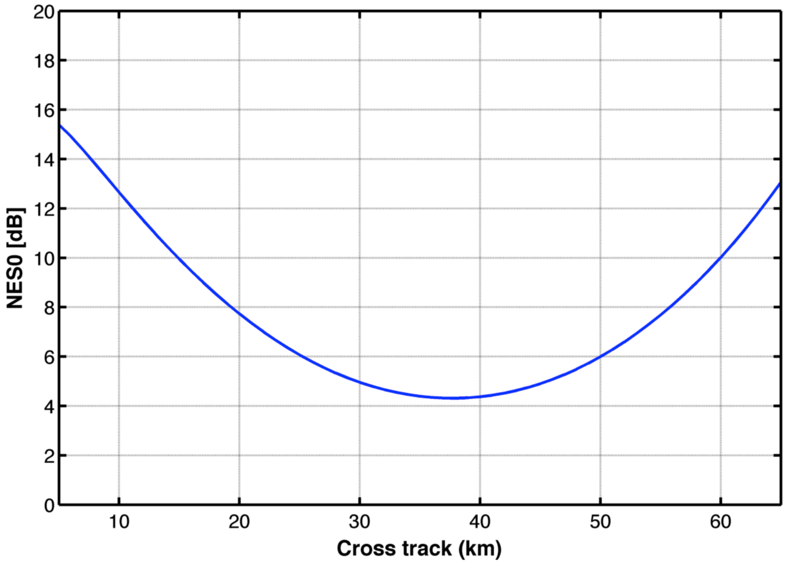

Figure 29. Noise equivalent sigma0, including margins.

5.4.3 Geometric Decorrelation

The main contributors to the geometric decorrelation are residual mis-registrations between the two images, errors in the spectral filtering implemented in the Onboard Processor, and spectral distortions in the Tx/Rx response of the system. In addition, dynamical geometric errors appear due to errors in the actual radial height (as a result of a combination of orbit errors, ocean variability, and onboard processing implementation choices in the reference surface that is used). These errors are briefly discussed hereafter.

Residual misregistration

Due to the fact that the two receivers are separated by the interferometric baseline, signals from the same point on the ground will arrive at different times at the receivers. This can be mitigated simply by adding a single delay between the channels so that the signals are perfectly corregistered for a given look angle. However, residual misregistration will still occur away from the selected direction. For KaRIn, the worst-case (far-swath) delay between antennas is:

$$\Delta r \approx B sin(\theta)|_{\theta=\theta_{max}} = 0.72\ m$$

so that, if the two SAR images are co-registered at the swath center, the differential delay would be 0.36 m. Since this is close to being half the instrument's range resolution of 0.75 m, differential range delays will cause severe decorrelation. To address this, the onboard processor implements a re-sampling stage. This is a standard technique for conventional SARs, where in order to perform channel registration, an interpolation algorithm using a finite interpolation kernel (e.g. sinc interpolation) is implemented, with the corresponding phase shift.

Radial height error

In addition, an unknown height error will affect the accuracy of the corregistration, introducing an additional misregistration between the two interferometric channels. The impact of an unknown height error will thus be to introduce an additional decorrelation term, thereby becoming a random error term; the correlation decreases as the look angle decreases, and therefore the error increases in the near swath. There are several sources of height errors that are relevant to this decorrelation: orbit errors, mean sea level, ocean variability, and tides. Some of these, such as orbit errors, have been mentioned in previous sections in relation to systematic errors. A key difference here is that for random errors we are not interested height error due to POD, but we are rather interested in establishing an upper bound to the total on-orbit height error, in order to limit the amount of decorrelation that can be tolerated.

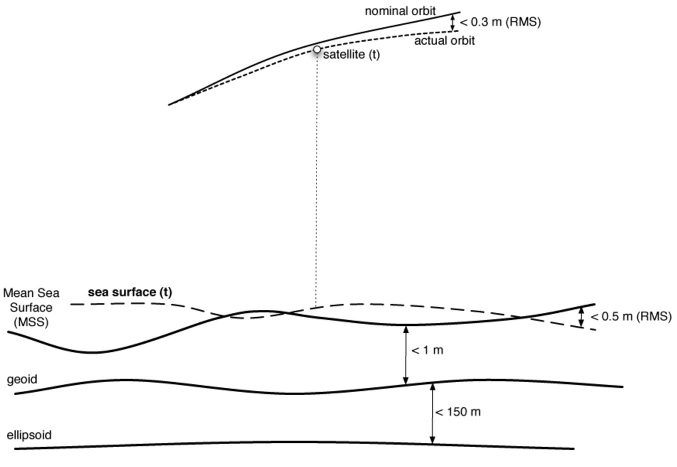

Figure 30. Sources of height errors: orbit errors, and sea surface deviations from the MSS reference surface.

The different height error sources are illustrated in Figure 30, and quantified in Table 6. First, there are errors associated to the platform's position. In nominal conditions, the radial orbit error corresponds to the maximum knowledge error with respect to the true in-flight orbit. This error is allocated 1 m, and will be achieved by a geodetic packet that DORIS provides to KaRIn on a periodic basis, using a similar capability to what is already implemented for the Nadir Altimeter.

Second, there are errors associated to the reference ground surface that is used as part of the onboard processing. Since the mean sea surface (MSS) is the reference surface implemented in the onboard processor for along-track height, the only residual height error (besides minor errors in the implementation of the MSS and a potential uncertainty of the MSS itself) is introduced by the deviation of the actual sea surface from this reference surface. This error can be decomposed into two major components: (1) the ocean variability, i.e., the (tide-free) height variability above the MSS and ocean tides. The ocean variability is unknown on-orbit, but can certainly be bounded: the RMS of the sea level variability, relative to a one-year mean sea level is, at a global scale, much lower than 0.5 m: the Agulhas, Gulf Stream, and Kuroshio barely exceed 0.4 m, with a maximum of roughly 1.1 m found in a few extreme cases such as the Amazon Fan; and (2) Ocean tides, which naturally introduce an unknown on-orbit height error which have been assessed by Cherniawsky et al. [8] for the four principal tidal constituents (M2, K1, S2, O1). This enables us to bound the error, as shown in Table 6, to less than roughly 1.1 m RMS. Combining all the errors as a direct sum of all the RMS height error results in less than 4 m height error. In reality, this is a fairly pessimistic upper bound of the RMS height error, as it assumes that all the errors occur together. The decorrelation term associated to a 5 m height error is therefore part of the overall random error budget.

Table 6. Sub-allocation of all the height error sources for the ocean

Height Error Source	RMS	Max
Deviation from nominal orbit (allocated to S/C; fulfilled via specific DORIS packet)	< 1m	1 m
Implementation of MSS in KaRIn (allocated to KaRIn)	< 1.6 m	< 2.5 m
Geophysical height errors:		
Ocean Variability	< 0.5 m	< 1m
Tides	O1 < 0.20 m K1 < 0.31 m M2 < 0.44 m S2 < 0.15 m	O1 < 0.54 m K1 < 0.90 m M2 < 2.25 m S2 < 0.84 m
MSS Uncertainty	< 0.5 m	< 2.5 m
TOTAL SUM/RSS	**< 5.0 m / <2.5 m**	**< 12 m / < 5m**

Spectral filtering

A third source of this form of decorrelation is due to the fact that the interferometric phase is not constant for all the scatterers within a given resolution cell. This variation in the interferometric phase causes the total interferometric contribution from that cell to add slightly incoherently, thus reducing the signal correlation. However, for monochromatic signals, one can choose the wavelengths of the two channels to be such that the projected wave-vectors on the ground are identical for both channels [9]. In this case, the interferometric phase would be constant for all scatterers in the resolution cell, and the returns would add coherently. For a finite bandwidth signal, one can to take the signal from both channels and shift the spectra in such a way that the appropriate wavelengths are multiplied together so that the phase variation over the resolution cell is canceled. The wave-number shift applies to SAR's, where the angular variation of the resolution cell in the azimuth direction is very small, so that iso-range and iso-phase lines are approximately aligned. However, this spectral shift means that noise is now brought into the processing bandwidth. In order to remove this additional noise, a low-pass filter is used so that only the parts of the spectra that overlap between both images contribute to the interferometric return. The penalty for this low-pass filter is a loss in resolution, but this loss is small and acceptable. Theoretically, the required shift and the amount of overlapping bandwidth of the two spectra depends on the incidence angle, and the filter response should be adaptive in the cross-track direction (by means of a bank of filters) to optimize for the changing frequency shift and bandwidth. However, KaRIn's onboard processor implements a fixed filter bandwidth of 196 MHz, which virtually eliminates this source of decorrelation, and the residual loss of coherence is negligible.

Transmit/Receive Transfer Function Stability

Additional sources of decorrelation are associated to the stability of the transmit/receive function of the KaRIn instrument. The geometric correlation is given by:

$$\gamma_G = \frac{\int W_1(\omega - w)H_1(\omega)W_2^*(\omega + w)H_2^*(\omega)e^{-j\omega\tau_d}d\omega}{\sqrt{\int |W_1(\omega - w)H_1(\omega)|^2 d\omega \int |W_2(\omega + w)H_2(\omega)|^2 d\omega}}$$

where W_i are the range point target responses for each interferometric channel, and $H_i(\omega)$ are the (low-pass) Prati filters. For the purpose of this derivation, we assume that the Prati filter is the same for both, $H_1(\omega) = H_2(\omega) = H(\omega)$, and that it is real and symmetric to approximate the correlation as:

$$|\gamma_G| \approx \frac{\int |W_1(\omega - w)||W_2(\omega + w)||H(\omega)|^2 d\omega}{\sqrt{\int |W_1(\omega - w)H(\omega)|^2 d\omega \int |W_2(\omega + w)H(\omega)|^2 d\omega}} \cdot \left(1 - \frac{1}{2}\left(< \left(\phi_1(\omega) - \phi_2(\omega)\right)^2 > - < \phi_1(\omega) - \phi_2(\omega) >^2\right)\right)$$

This expression shows that there are two key contributors: the first one is related to the magnitude, and the second one to the phase. The impact of linear and quadratic terms on the magnitude of the point target response, as well as due to ripple, are allocated from the first condition, whereas we refer to the second one as the standard deviation of the differential phase (this term, to first order, is equivalent to a differential group delay, but in fact accounts for higher order non-linearities in the interferometric frequency response). The allocations for these, as imposed on the KaRIn system, are summarized in the table below.

Table 7. Amplitude requirements

Amplitude error	Description	Requirement
Differential amplitude slope vs frequency	$|\gamma_G| \approx 1 - \frac{1}{24}(a_1' - a_2')^2 \Delta\omega^2$	$(a_1' - a_2') < 2dB/200\ MHz$
Standard deviation of the differential phase	$< \left(\phi_1(\omega) - \phi_2(\omega)\right)^2 > - < \phi_1(\omega) - \phi_2(\omega) >^2$	< 0.7 dB
Amplitude Ripple (including quadratic terms) vs frequency	$|\gamma_G| \approx 1 - \frac{1}{4}(a_{r1}^2 - a_{r2}^2)$	$RMS_{ri}(dB) = 6a_{ri} < 0.5\ dB$

The sensitivity of the correlation to an amplitude slope is shown in the figure below.

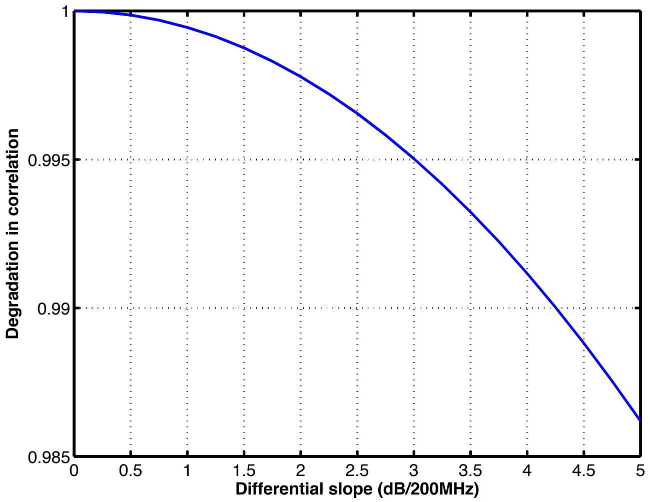

Figure 31. Degradation in correlation as a function of the differential slope over the bandwidth.

5.4.4 Angular decorrelation

The angular decorrelation includes several effects. Primarily, the effect of the ocean waves introduces a volume scattering layer on the angle subtended by a range resolution cell, thereby introducing a volumetric decorrelation, as well as a non-linear mixing of the ocean wavelengths termed the surf-board effect. In addition, and due to the fact that for a monostatic system such as KaRIn, the lines of constant range (iso-range lines), and the lines of constant phase (iso-phase lines), are only approximately aligned, the interferometric fringes vary over the range cell, even after the spectral shift described in the previous section, introducing an additional (yet small) amount of decorrelation. Each one of these effects is discussed below.

Volumetric (wave) decorrelation

The statistics of the ocean surface height can be modeled with the following probability function:

$$f_s(h) = \frac{1}{\sqrt{2\pi\sigma_h^2}} e^{-\frac{h^2}{2\sigma_h^2}}$$

where h is the topographic mean height at a given point, and σ_h is the ocean height standard deviation, related to the significant wave height as SWH=$4\sigma_h$. The resulting correlation in the presence of a SWH is given approximately by:

$$\gamma_a \approx e^{-2\sigma_h^2\left(\frac{kB}{\rho sin\theta_o}\right)^2}$$

where θ_0 is the look angle at the time of closest approach for a target at a given range distance r, and ρ is defined for spherical Earth as:

$$\rho = \frac{2\,(H+R_E)^2}{(H^2+2HR_E+r^2)}\frac{r^2}{R_E}$$

where R_E is the Earth radius and H is the satellite altitude. The amount of decorrelation due only to the iso-range and iso-phase misalignment (corresponding to a SWH=0 m case) is negligible for KaRIn's swath. The main source of decorrelation is due to the presence of waves, which can be significant for large SWHs. The Science Requirement Document specifies a SWH of 2 m in the spectral requirement, which is accounted for as part of the KaRIn random error budget.

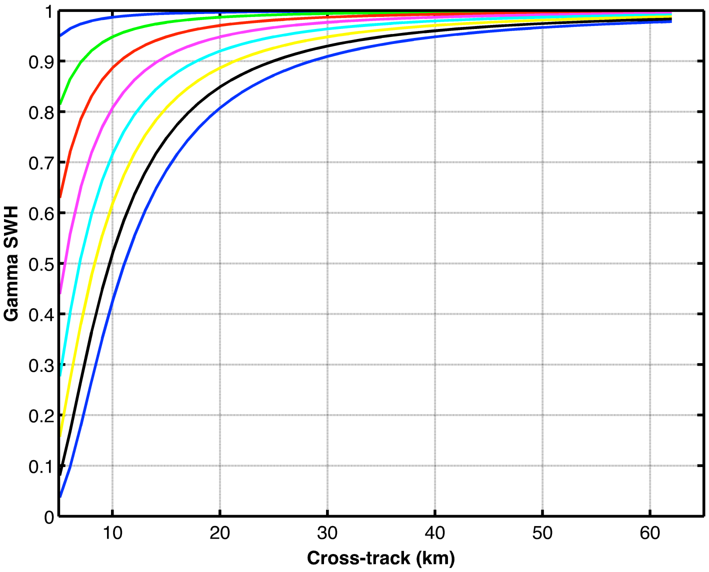

Figure 32. Volumetric correlation associated to the SWH, shown as a function of cross-track distance for SWH ranging from 1 to 8 m.

Surf-board effect

The presence of surface gravity waves introduces an additional source of height error. As previously described, the reported sea surface height (SSH) is in fact a weighted average of the sampled SSH over an area of $(500\ \mathrm{m})^2$. Even though the spectral content of the wave spectra is typically concentrated at smaller wavelengths, the measured height is a nonlinear function of the wave height, which introduces spectral components at wavelengths above 500 m that are not filtered and will become an additional source of height error. This source of error is termed "surf-board effect", symbolizing the iso-range line being the "surf-board" that cuts across the ocean wave such that the points of intersection create the highest return, as illustrated in the figure below.

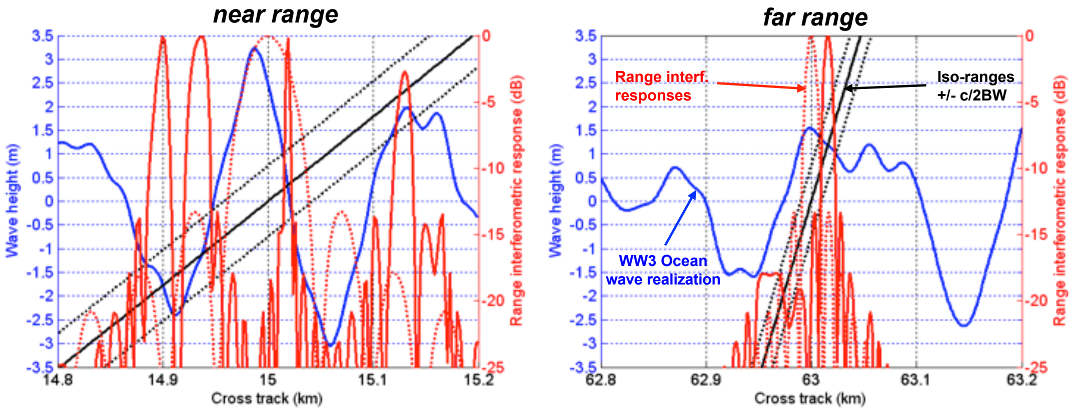

Figure 33. Illustration of the surf board effect in the cross track direction for simulated ocean waves realizations using WaveWath-3 for a SWH of 3 m (in blue), for two points in the swath (15 km and 63 km). The iso-range line (black) cuts the wave at various points, distorting the effective interferometric range response (solid red; nominal response in dashed red).

The height error increases in the near range inversely proportional to the sine of the incidence angle, and grows rapidly as a function of the SWH, starting to dominate in the near range over the thermal noise for SWH larger than 3 m, as shown in the figure below. This error is also accounted for in the KaRIn random error budget for SWH = 2 m, as specified in the Science Requirements Document. It is important to note that for SWHs higher than 4m, this error starts dominating over the random noise in the measurement for a significant portion of the swath.

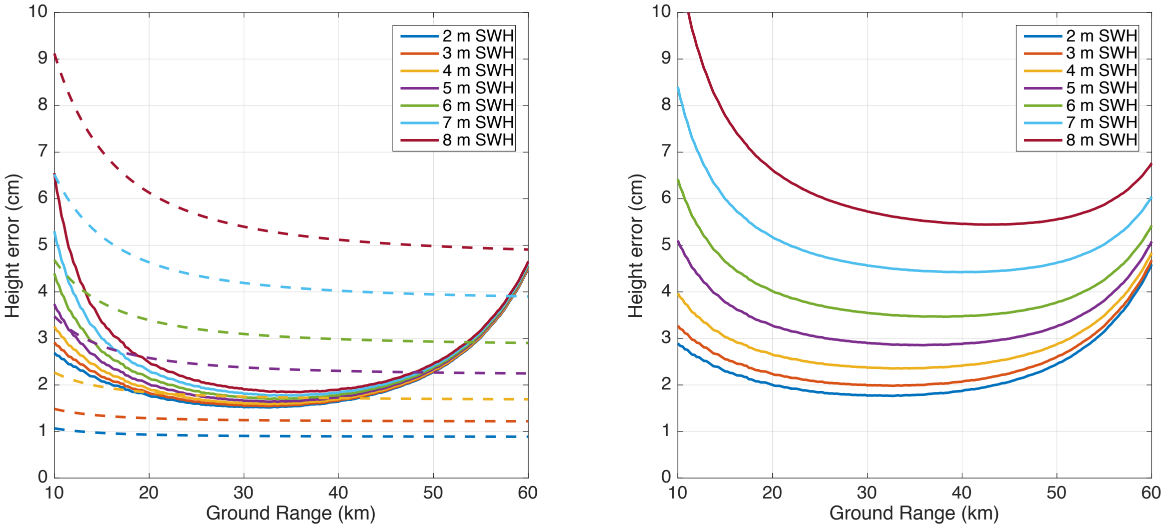

Figure 34. (left) Height error for 1km^2 pixels as a function of cross track due to random noise (solid) and surfboard effect (dotted) for several SWHs. (right) total height error as the RSS of the random noise (which is discussed in the following section) and the nonlinear wave energy transfer.

Antenna pattern knowledge and stability

The dependence of the angular correlation on the antenna pattern is made explicit by the expression of the angular decorrelation:

$$\gamma_{\varphi}^{(J)} = \frac{\oint_{r=r_0} G_1(\vec{r})G_2^*(\vec{r})\sigma_0(\vec{r})\chi_{az}^{(J)}(\vec{r})e^{j2k(r_1-r_2-\delta r)}ds}{\oint_{r=r_0} G_1(\vec{r})G_2^*(\vec{r})\sigma_0(\vec{r})\chi_{az}^{(J)}(\vec{r})ds}$$

where the J super-index refers to each of the beams that are generated onboard by the OBP. Approximating the product of antenna gain, sigma-0, and azimuth point target response as a Gaussian function of the antenna azimuth angle, ϕ, centered at ϕ_J and with variance ϱ_J, the decorrelation is approximately given by:

$$\left|\gamma_{\varphi}^{(J)}\right| \approx e^{-2\left(\frac{kB}{\sin\theta_0}\varrho_J\phi_J\right)^2}$$

which will dictate the pointing as well as antenna pattern knowledge and control requirements. However, this source of decorrelation is exceedingly small in comparison with the other sources of angular decorrelation.

5.4.5 Overall Random performance

The overall random error uses the decorrelation terms derived in the previous sections to derive the height error performance over a spherical Earth approximation. The coherences are shown in the figure below.

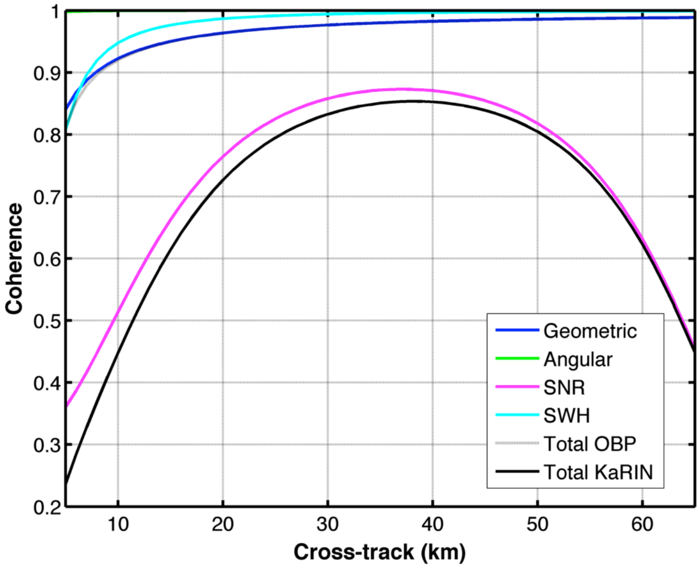

Figure 35. Geometric, angular, thermal (SNR), and volumetric (SWH) correlations across the swath.

The total number of effective looks over a 1 km^2 ground-range area, ranging from roughly 3,700 to 40,800 looks across the swath, take into account the slight loss in resolution introduced by the filtering stage of the wave-number shift. Finally, the standard deviation of the height error due to the random phase error, relative to the MSS surface implemented in the onboard processor, is given by:

$$\sigma_h = \frac{\rho \sin(\theta_0)}{kB} \sigma_{phase}$$

The standard deviation of the height error due to the overall random error performance across the swath (including the surf-board effect) is shown in the figure below, with a swath averaged (10 km to 60 km) height error of 2.4 cm.

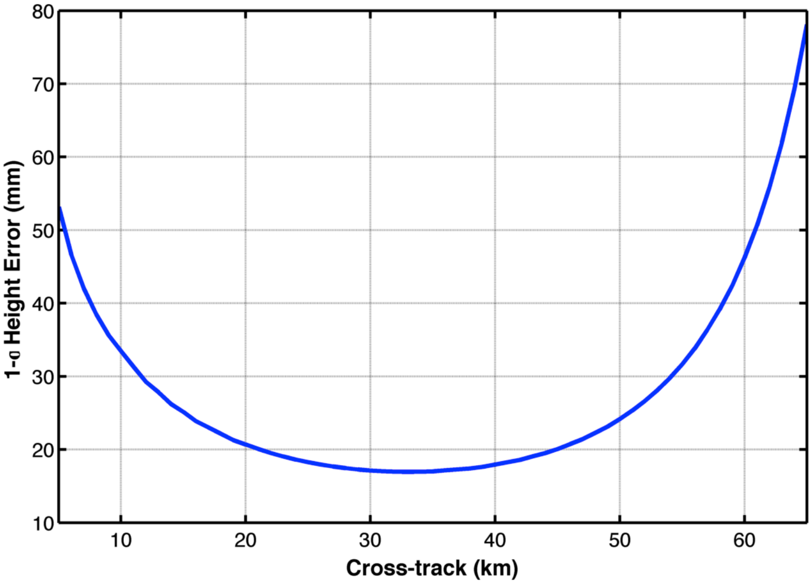

Figure 36. Final ocean height error performance at 1 km x 1 km due to all the random errors.

5.5 OCEAN SYSTEMATIC ERROR REQUIREMENTS

The overall flow of the key systematic errors across mission elements is illustrated in the figure below, and each component discussed in detail hereafter. It is important to note that the derivations are first described and obtained under the assumption that these errors are uncorrelated. Following this, and later in this section, the allocations are derived without this assumption.

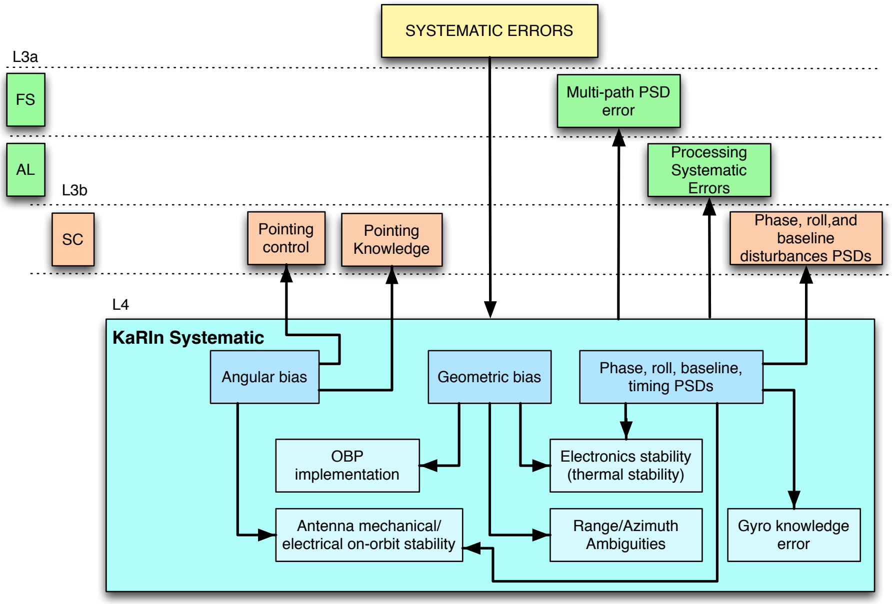

Figure 37. Conceptual high-level flow-down of the random errors to the key mission elements.

5.5.1 Overview of Roll Drift Errors

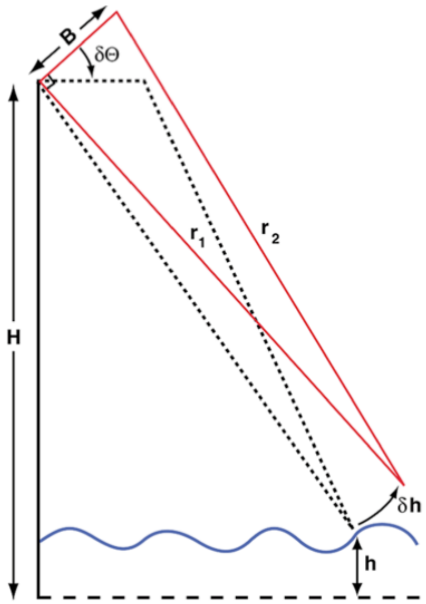

Figure 38. The effect of a roll error is to introduce a tilt to the measured surface

Knowledge errors in the interferometric roll angle induces height errors, as illustrated in Figure 38. At any given point in time, the height error, δh, due to a roll error δθ, is obtained by:

$$\delta h(t) = r(t)\sin\big(\theta(t)\big)\,\delta\theta(t) \approx C\left(1+\frac{\mathrm{H}}{\mathrm{R_E}}\right)\delta\theta(t)$$

where C is the cross-track distance to the point of interest (i.e., the distance between the nadir point and the pixel of interest), and R_E is the radius of the Earth. The height error due to a roll error grows approximately linearly across the swath, thereby having the effect of creating a local tilt of the entire swath. As an example, a roll knowledge error of only 1/10,000 deg (0.36 arc seconds) would result in a height error of roughly 6 cm for a point situated at 35 km in the cross-track direction. It is thus clear that in order to meet centimetric stability accuracy, a very accurate knowledge of the roll drift is required for SWOT.

The main source of roll errors is knowledge errors in the spacecraft attitude. The KaRIn instrument will carry a dedicated, high-performance gyroscope, which will provide the required knowledge of the spacecraft rigid-body roll angle. Gyroscopes (or gyros) measure rotational values without reference to external coordinates. Most gyros for space applications measure the speed of rotation (also known as 'rates') in each axis. The residual roll knowledge error typically appears after integration of the rates as an angular drift, increasing linearly over time. The roll error requirement that is thus imposed to the interferometer's gyro is a residual knowledge error (drift), rather than an absolute knowledge or control requirement. In other words, the platform is not required to limit (control) its roll attitude to very accurate (sub-arcsec) levels to ensure that the height error is bounded (within the limits established by the pointing requirements discussed later, which are not anywhere near these stringent levels), and it is not required to be known in an absolute sense either; the only requirement is that the gyro's roll drift knowledge error is small enough to meet the desired centimetric accuracy.

A second source of error in the roll knowledge is introduced by the KaRIn mechanical system formed by the boom and the antenna and feed support structures, due to thermal and vibration distortions. Changes in the on-orbit thermal environment, or dynamics (introduced, for example, during the rotation of the solar arrays, or by the reaction wheels on the S/C), can distort these structures and displace the antennas asymmetrically, effectively introducing a roll error.

Dynamic effects are usually small and can be mitigated by placing isolation mechanisms between the bus and the payload to dampen specific resonant frequencies of the interferometer's mechanical structures, if needed. To tackle this from the onset, the KaRIn first mode requirement has been specified to be a minimum of 7 Hz, which ensures that any disturbances are not amplified below the 6.5 Hz which relate directly to the ocean SSH measurement spectrum.

The on-orbit thermal environment is typically slowly changing and therefore doesn't introduce rapid changes in the roll; however the mechanical structures still need to be designed with very low coefficient of thermal expansion (CTE) materials, and standard thermal techniques, such as employing multi-layer insulation (MLI) blankets or low solar absorptivity coatings, where possible, to minimize both the effect of solar flux transients as well as the effect of shadowing of portions of some specific mechanical structures by other spacecraft surfaces. The Earth's infrared (IR) and albedo loads are less of disturbance drivers due to their diffuse nature and the relatively constant orientation of the SWOT KaRIn payload to Earth. Periods of eclipse entry and exit can result in sudden changes in incident solar flux, introducing fast disturbances; however, as specified in the Science Requirements Document, the performance requirements do not apply to these eclipse periods, provided the performance degradation does not exceed 5% of the time, including all possible effects.

Specifying the allowed height error as a function of time (or, equivalently, along-track distance), the roll power spectrum for a given cross-track distance, *C*, is just the height error power spectrum divided by C^2. Specifically, if the root-mean-squared (RMS) error obtained by integrating the height error spectrum in a specific band for a given *C* is $\sigma_{h|C}$, the RMS roll spectrum (in radians) will be $\sigma_{\theta|C} = \sigma_{h|C}/C$. This raises the question of what cross-track distance should be used to define the requirement. In reality, the specification is given as a swath-averaged performance, rather than the performance at a given cross-track distance (e.g., the far swath). Denoting $f(\delta h,C)$ as the probability density function of height error and cross-track distance, the swath averaged height variance, σ_h^2 is given by:

$$\sigma_h^2 = \int dC \int d\delta h\,(\delta h)^2 f(\delta h, C) = \sigma_\theta^2\left(1+\frac{\mathrm{h}}{\mathrm{R_E}}\right)\int dC\, f(C)C^2$$

$$= \sigma_\theta^2\left(1+\frac{\mathrm{h}}{\mathrm{R_E}}\right)\left[\frac{C_{max}^3 - C_{min}^3}{3(C_{max}-C_{min})}\right] \triangleq \sigma_\theta^2\left(1+\frac{\mathrm{h}}{\mathrm{R_E}}\right)\bar{C}^2$$

where it has been assumed that f(C) is uniformly distributed over the swath. Therefore, the swath-averaged performance is equivalent to the performance evaluated at a point C given by:

$$\bar{C} = \sqrt{\frac{C_{max}^3 - C_{min}^3}{3(C_{max}-C_{min})}}$$

For KaRIn, with a swath extending from 10 km to 60 km, C ≈ 37.9 km. The flow-down of the roll error into all the different elements is shown in the figure below.

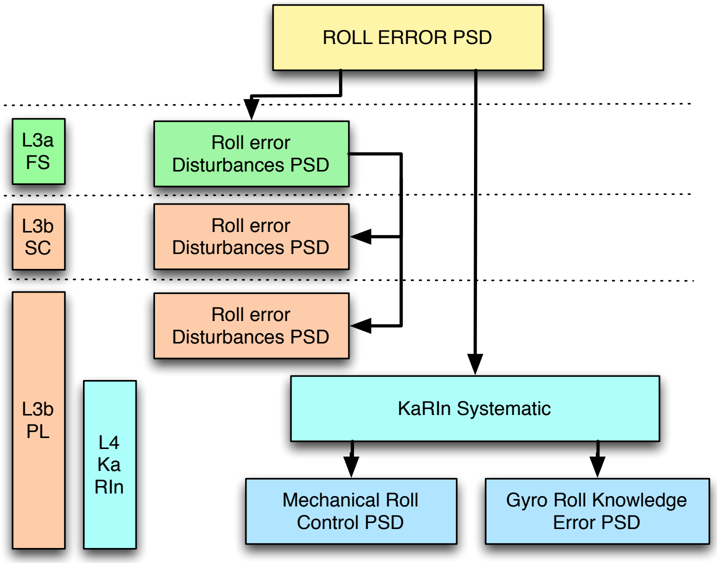

Figure 39. Conceptual high-level flow-down of the roll PSD to the key mission elements.

For KaRIn, the gyro roll error spectrum is directly sub-allocated by KaRIn as part of its systematic errors, and is based upon the following end-of-life noise model requirements:

- Quantization, q= 1.0E-3 asec
- Angular Random Walk (ARW), N < 0.00015 deg/√h
- Bias stability, B between 0 and 5E-5 deg/h
- Rate Random Walk, K, between 0 and 2E-5 deg/$h^{1.5}$
- White angle noise is below the quantization noise for sampling frequencies < 100 Hz and neglected (the sampling frequency requirement for the gyro is 64 Hz).

The noise model, following the IEEE standard [15] for a single sided PSD, is then given by:

$$\mathrm{PSD_{gyro}(f)} = 1.695\cdot 10^{-8} + 6.303\cdot 10^{-7}\mathrm{f}^{-2} + 4.756\cdot 10^{-13}\mathrm{f}^{-3} + 5.168\cdot 10^{-19}\mathrm{f}^{-4}\ [\mathrm{asec}^2/cy/km]$$

and is shown in the figure below.

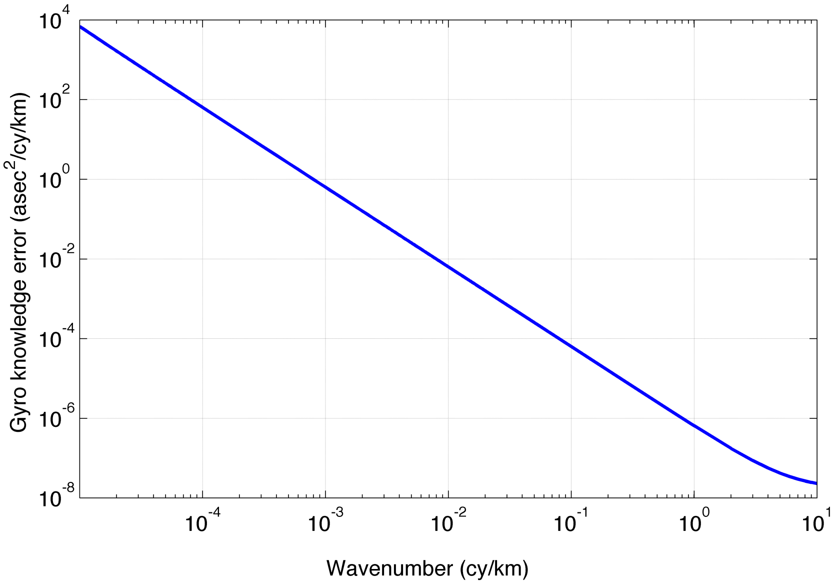

Figure 40. PSD of the gyro roll knowledge

The conversion to an SSH error is then given by:

$$E_{\text{gyro}}(\text{f}) = \text{PSD}_{\text{gyro}}(\text{f})\cdot\left(1+\frac{\text{h}}{\text{R}_\text{E}}\right)^2\cdot\bar{C}^2[km]\cdot 10^{10}\left(\frac{cm}{km}\right)^2\cdot\left(\frac{\text{pi}}{648000}\right)^2 \qquad \left[\frac{cm^2}{cy/km}\right]$$

Of the overall systematic error, the roll error (excluding the gyro) is sub-allocated 20% of the systematic errors. The Flight System roll control error associated to dynamic effects on the KaRIn roll is sub-allocated a large fraction of the high frequency region, and less of the low frequency region, as given in the figure below. The rest is sub-allocated directly to the KaRIn mechanical structures. The corresponding PSDs, in units of asec^2/Hz, are:

$$E_{F/S\,roll} = \begin{cases} 6.73\cdot 10^{-8} f^{-2.17}, & f < 0.1367\,Hz \\ 5.05\cdot 10^{-6}, & f \geq 0.1367\,Hz \end{cases} \qquad [\text{asec }\hat{}2/Hz\,]$$

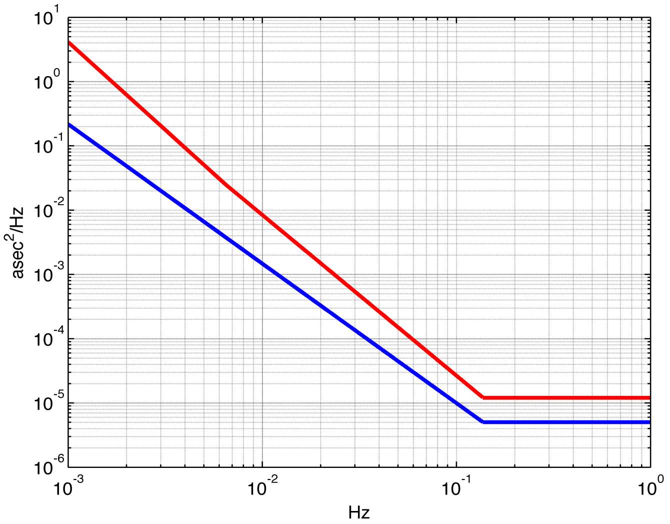

Figure 41. (blue) PSD of the roll allocation to the Flight System; for reference the total systematic error allocated to the roll is also shown (red)

The Flight System PSD is then further sub-allocated into S/C and Payload (non-KaRIn) components. Of the total, 95% of the PSD goes to the S/C, where most of the disturbances (eg. reaction wheels, solar arrays, etc.) are expected. The residual 5% goes to the Payload to cover non-S/C induced dynamics (such as micro-dynamics associated to the payload structures).

5.5.2 Overview of Differential Phase Drift Errors

Systematic phase errors arise due to changes in the relative phase between the two signal paths in the interferometric pair. An illustration of the impact of a phase error on the height measurement is presented in **Figure 42**. The height error introduced by a phase error is given by:

$$\delta h = \frac{\lambda r \tan(\theta)}{2\pi B}\delta\phi \cong \frac{C}{kB}\left(1 + \frac{H}{R_E}\right)\delta\phi$$

A differential phase drift has the effect of creating a height error that also increases linearly across the swath, like a roll error. There are several contributors to the phase imbalance between the two interferometric radar channels, which are associated to the different Flight System and KaRIn elements:

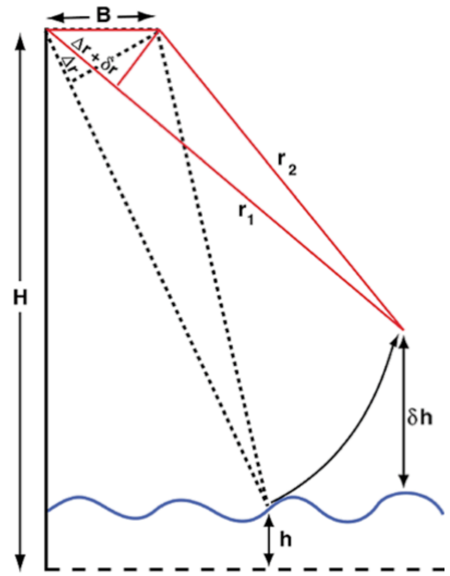

Figure 42. Illustration of the impact of a phase error on the height estimate.

1) A phase drift between the two interferometric radar channels introduced by any of the radar electronics subsystems. Phase drifts in the radar electronics are mostly temperature driven, and therefore slowly varying. On the one hand, a phase drift in the transmit chain cancels out since it is common to both receive channels. Therefore, only the relative drift between the two radar receive chains is of concern. To mitigate this error source, a calibration loop for each path is part of the instrument design, which can serve to correct some of the drifts. In addition, KaRIn defines thermal control drift rates requirements (both absolute and relative) for the thermal subsystem with regards to the relevant radar electronics boxes.

2) A phase drift introduced by the antenna and mechanical/thermal subsystem. These are thermal or vibration induced mechanical distortions in the antenna subsystem (either in the reflectarray antennas or the feeds) that can change the phase response of the overall antenna system. Here, two distinct contributions pertaining to a systematic phase drift arise: (1) an effective displacement of the phase center of the antenna, and (2) a change in the actual far-field phase pattern response over the main-lobe (and over the transmit frequency bandwidth) that illuminates either swath. This second terms would be the variation of the “phase screen”, and requirements imposed on the KaRIn antenna and mechanical system ensure that this error term is appropriately bounded. In addition to thermal distortions, dynamic disturbances generated within the S/C may propagate through the KaRIn structures and generate resonances or oscillations in its structures and need to also be considered.

3) System phase mismatch. These are phase drifts induced by multi-path and external signals. If e.g. a small portion of the radiated power is reflected back by any of the spacecraft surfaces, a phase bias will be induced on the desired interferometric measurement. Any changes in the reflected signal over time (both in phase and amplitude), can result in a change of this bias term, thereby introducing a systematic phase drift. Multi-path signals can be classified as being either coherent with the direct signal, incoherent with the direct signal but coherent with itself (as measured by the two interferometric channels), or incoherent. The main effect of incoherent multi-path is only to reduce the available SNR, since it behaves as a noise source, thereby impacting the

random error performance. Correction of multi-path errors is typically performed post launch, when a high-fidelity model of the spacecraft is available. Moving surfaces, such as solar array rotations, are expected to constitute the main source of multi-path induced phase drifts. However, SWOT will only rotate its solar arrays at the top and bottom of the orbit every few days, thereby greatly mitigating any multi-path induced phase drifts over the time scales associated to the sub-mesoscale measurement.

The flow-down of the phase error to all of the appropriate elements is shown in the figure below.

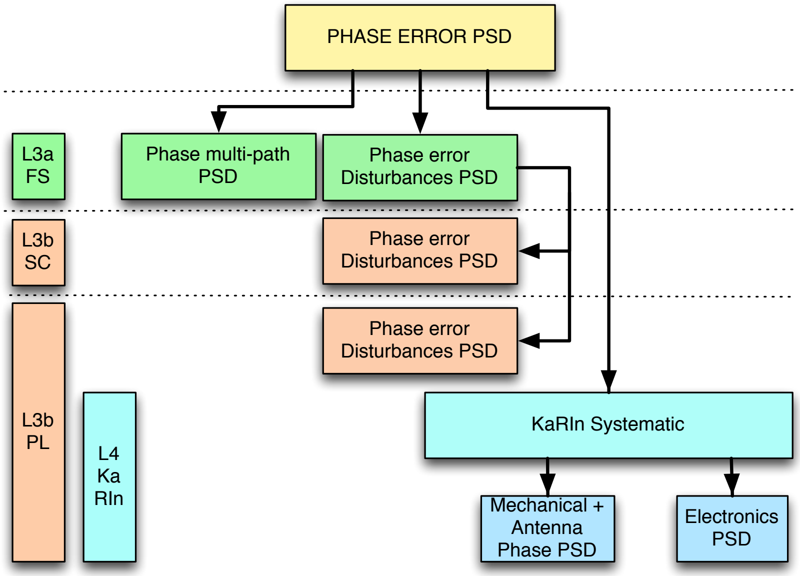

Figure 43. Conceptual high-level flow-down of the phase PSD to the key mission elements.

The total phase error is allocated 60% of the overall systematic error. The RMS phase drift for the swath average performance can be derived in a similar fashion as to what has been derived before for the roll error:

$$\sigma_h^2 = \frac{\sigma_\phi^2}{(C_{max} - C_{min})}\left(1 + \frac{\mathrm{h}}{\mathrm{R_E}}\right) \int dC \left(\frac{C}{kB}\right)^2 = \frac{\sigma_\phi^2}{(kB)^2}\left(1 + \frac{\mathrm{h}}{\mathrm{R_E}}\right)\left[\frac{C_{max}^3 - C_{min}^3}{3(C_{max} - C_{min})}\right]$$
$$\triangleq \frac{\sigma_\phi^2}{(kB)^2}\left(1 + \frac{\mathrm{h}}{\mathrm{R_E}}\right)\bar{C}^2$$

The overall phase error spectrum is shown in the figure below, which is further sub-allocated to the Flight System (for dynamic effects on the KaRIn phase), system multi-path, and KaRIn. The phase error spectrum sub-allocated to the S/C is given by 95 % of the Flight System PSD below, in units of deg^2/km, with the P/L receiving the remaining 5%.

$$E_{F/S}(f) = \begin{cases} 3.483 \cdot 10^{-7} f^{-2.17}, & f \leq 0.1367\ Hz \\ 2.614 \cdot 10^{-5}, & f > 0.1367\ Hz \end{cases}$$

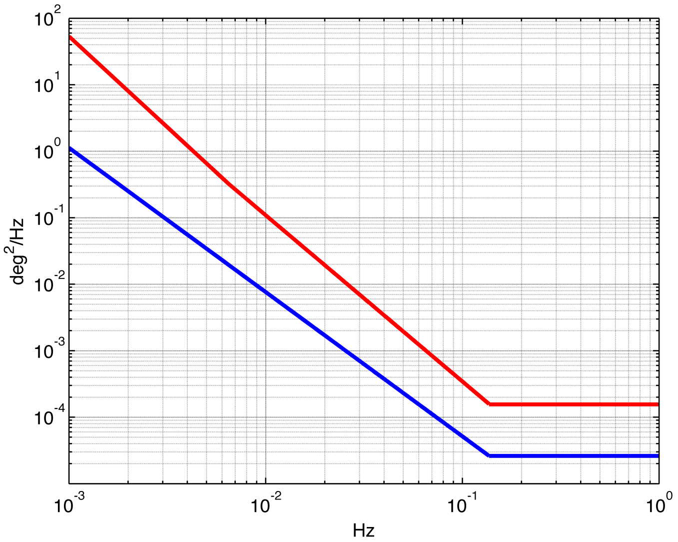

Figure 44. (blue) PSD of the phase allocation to the S/C; for reference the total systematic error allocated to the phase is also shown (red)

KaRIn receives the remaining portion of the error spectrum of the differential phase drift, which is sub-allocated into the following components:

- The KaRIn mechanical/thermal, for distortions in the baseline, reflectarray antenna and feed support structures (20 %);
- The KaRIn antenna electrical performance, for deformation errors in the panels, changes in the dielectric constants of the panels (20%),
- The KaRIn electronics (RF and digital) and waveguides (57%).

The remainder (3%) is flowed up to the overall Flight System for multi-path effects. The current sub-allocations are based on engineering judgment and preliminary analysis, and will be adjusted as needed throughout the life of the mission. The figure below shows the KaRIn sub-allocations, as well as the system multi-path.

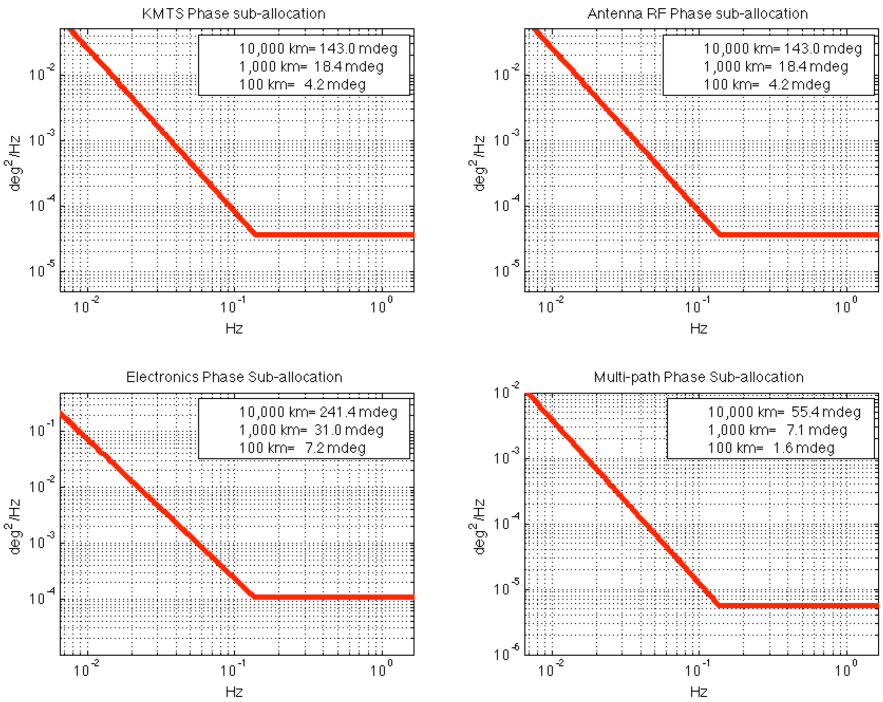

Figure 45. Sub-allocation of the differential phase drift onto the different KaRIn elements (KaRIn Mechanical/Thermal System –KMTS-, Antenna, and Electronics) and the Flight System multi-path.

5.5.3 Overview of Baseline Dilation Drift Errors

As with any interferometer, a change in the baseline length directly impacts the precision of the height measurements that can be obtained. For SWOT, the baseline length is to be understood as the projection onto the YZ plane of the line that crosses the two reference coordinate systems previously defined at each end of the mast. The height error introduced by a baseline error δB is given by:

$$\delta h = -\frac{r sin(\theta)\tan(\theta)}{B}\delta B \approx -\left(1+\frac{H}{R_E}\right)\frac{C^2}{HB}\delta B$$

A baseline dilation error has therefore the effect of creating a quadratic height error across the swath.

The baseline error is allocated 5% of the overall systematic error. The flow-down of the baseline error to all of the appropriate elements is shown in the figure below.

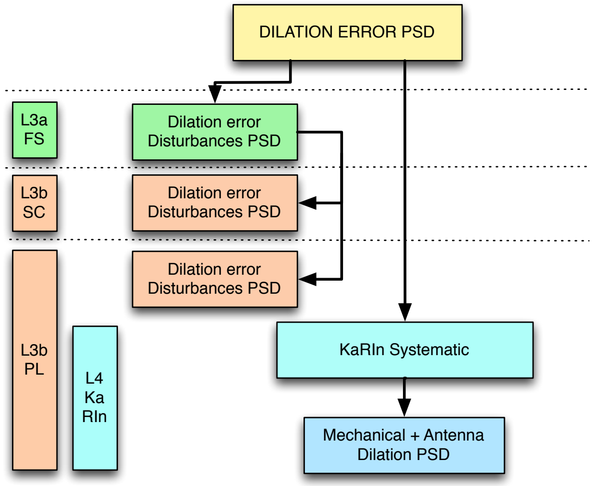

Figure 46. Conceptual high-level flow-down of the baseline PSD to the key mission elements.

The RMS baseline drift for the swath averaged performance can be derived in a similar fashion as to what has been derived before:

$$\sigma_h^2 = \frac{\sigma_B^2}{(C_{max} - C_{min})}\left(1 + \frac{\mathrm{h}}{\mathrm{R_E}}\right)\int dC\left(\frac{C^2}{HB}\right)^2 = \frac{\sigma_B^2}{(HB)^2}\left(1 + \frac{\mathrm{h}}{\mathrm{R_E}}\right)\left[\frac{C_{max}^5 - C_{min}^5}{5(C_{max} - C_{min})}\right]$$

The total baseline error spectrum and the KaRIn allocation is shown in the figure below.

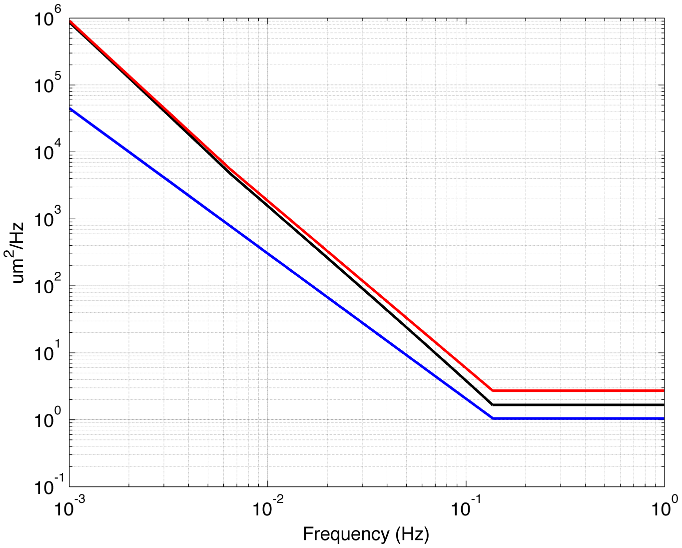

Figure 47. (red) total systematic error allocated to the baseline dilation; (black) dilation error directly allocated to KaRIn; (blue) PSD of the dilation allocation to the F/S for dynamic effects.

A portion of the total baseline error spectrum is also allocated to the Flight System for dynamic effects on the KaRIn baseline length, which is given by the following equation, in units of $\mu m^2/km$.

$$E_{F/S}(f) = \begin{cases} 0.0139 \cdot f^{-2.17}, & f \leq 0.1367\ Hz \\ 1.0445 \quad , & f > 0.1367\ Hz \end{cases}$$

Of that F/S allocation for dynamic effects, 95% is sub-allocated to the S/C, with the P/L (non KaRIn) receiving the remaining 5%.

5.5.4 Allocation of phase, baseline, and systematic roll errors

While one could allocate separately requirements for each one of the above errors, the fact that some of these can be correlated introduces the need for a formulation that will take this into account. For example, thermoelastic and disturbance effects will induce mechanical deformations that can introduce correlated phase, roll, and baseline dilations errors. As a result, the true effect of these errors could add to a height error that is larger than the sum of the height errors for each separate component, whereas an approach based on the sum of PSDs inherently assumes that the different errors are uncorrelated. Mathematically, the variance of the errors is given by:

$$\begin{aligned} &var(phase + baseline + roll) \\ &\quad = var(phase) + var(baseline) + var(roll) + 2cov(phase, roll) \\ &\quad + 2cov(phase, baseline) + 2cov(baseline, roll) \end{aligned}$$

and it is neither correct nor prudent to assume that the covariance terms are necessarily negligible in some cases. In order to derive a formulation that takes the correlation into account, we start from the equation relating a target position vector $\vec{T}$, a reference position for the platform $\vec{P}$, and the look vector $\vec{l}$, which is given by:

$$\vec{T} = \vec{P} + \vec{l} = \vec{P} + \rho\hat{l}$$

where ρ is the range to the target, and $\hat{l}$ is the unit vector in the direction of $\vec{l}$ (see Figure 48).

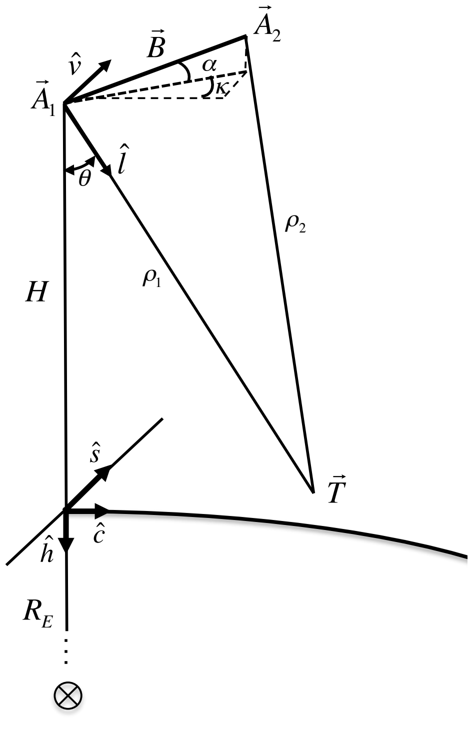

Figure 48. Imaging geometry

Denoting $\vec{B}$ as the baseline vector from antenna 1 to antenna 2, i.e. $\vec{B} = \vec{A}_2 - \vec{A}_1$, and choosing arbitrarily $\vec{P} = \vec{A}_1$, the interferometric phase is then given by the well known expression:

$$\begin{aligned} \phi = \phi_1 - \phi_2 = \frac{2\pi}{\lambda}(\rho_2 - \rho_1) &= \frac{2\pi}{\lambda}\left(|\vec{l}_2| - |\vec{l}_1|\right) \\ &= \frac{2\pi}{\lambda}\rho_1\left[\left(1 - \frac{2 < \hat{l}_1, \vec{B} >}{\rho_1} + \left(\frac{B}{\rho_1}\right)^2\right)^{1/2} - 1\right] \end{aligned}$$

Where the expression $< \hat{l}_1, \vec{B} >$ denotes the dot product of vectors $\hat{l}_1$ and $\vec{B}$. Since B << ρ, it is common to approximate this to first order by:

$$\phi = -\frac{2\pi}{\lambda} < \hat{l}_1, \vec{B} >$$

Differentiating (1) with respect to the interferometric phase, baseline length, and roll, assuming again that B << ρ, yields [1]:

$$\overrightarrow{\Delta T} = \frac{\rho}{< \hat{B}, \hat{l}\; x\; \hat{v} >}\left[\left(-\frac{\lambda}{2\pi B}\Delta\phi - < \hat{l}, \frac{\overrightarrow{\Delta B}}{B} >\right)\hat{l}x\hat{v}\right] - \Delta\alpha\,\rho\,\hat{l}x\hat{v}$$

Hereafter we will start by assuming a flat Earth geometry, with the case where the baseline is fully contained in a plane perpendicular to the velocity vector, such that:

$$\vec{B} = [0, Bcos(\alpha), Bsin(\alpha)]$$

where B is the baseline length, α is the baseline orientation angle (roll), and assume a simple unit velocity vector given by:

$$\hat{v} = [1,0,0]$$

and a unit look vector given by:

$$\hat{l} = [0, \sin(\theta), -\cos(\theta)]$$

where θ is the look angle (the angle the line-of-sight vector makes with respect to nadir). Therefore the dot product $< \hat{l}, \vec{B} >$ results in:

$$< \hat{l}, \vec{B} >= Bsin(\theta - \alpha)$$

and so the interferometric phase results in the well-known expression:

$$\phi = -\frac{2\pi}{\lambda} Bsin(\theta - \alpha)$$

Focusing now on the equation for $\overrightarrow{\Delta T}$, it is easy to show that:

$$< \hat{B}, \hat{l} \; x \; \hat{v} >= -cos(\theta - \alpha)$$

$$\hat{l} \; x \; \hat{v} = [0, -\cos(\theta), -\sin(\theta)]$$

$$< \hat{l}, \frac{\overrightarrow{\Delta B}}{B} >= \frac{\Delta B}{B} \sin(\theta - \alpha)$$

and therefore:

$$\overrightarrow{\Delta T} = -\frac{\lambda \rho}{2\pi Bcos(\theta - \alpha)} [0, \cos(\theta), \sin(\theta)] \Delta\phi$$

$$-\frac{\rho}{B} \tan(\theta - \alpha) \, [0, \cos(\theta), \sin(\theta)] \Delta B$$

$$+\rho[0, \cos(\theta), \sin(\theta)] \Delta\alpha$$

If the quantity of interest is the vertical height error, Δh, then the above equation can be used to simply extract the third component of the target position vector (the other components in the expression being the position errors in the along-track and cross-track directions):

$$\Delta h = -\frac{\lambda \rho \sin(\theta)}{2\pi Bcos(\theta - \alpha)} \Delta\phi - \frac{\rho}{B} \tan(\theta - \alpha) \sin(\theta) \, \Delta B + \rho \sin(\theta) \, \Delta\alpha$$

While the phase error is typically associated to a differential drift in the radar electronics, here we also consider the fact that a displacement, δd, of any antenna relative to its nominal position will change its phase pattern by a term approximately given by the additional path length incurred, i.e. $\sim \left(\frac{2\pi}{\lambda}\right) \delta d$, as measured between the centroid of its feed and that of the reflectarray antenna. For the interferometric phase, the important term is the differential change in the two-way phase pattern between both antennas.

To tackle this, let's first decompose the baseline vector into the sum of its components (see Figure 49), namely, the vector between feed 1 and antenna 1, $\overrightarrow{L_1}$, the vector between feed 2 and antenna

2, $\overrightarrow{L_2}$, and the vector between feed 1 and feed 2, $\vec{F}$ (here we ignore that there are two sets of these to illuminate each swath, as the derivation applies to each one independently):

$$\vec{B} = \overrightarrow{L_1} + \vec{F} + \overrightarrow{L_2}$$

Where $\overrightarrow{L_1} = \overrightarrow{F_1} - \overrightarrow{A_1}$, $\vec{F} = \overrightarrow{F_2} - \overrightarrow{F_1}$, and $\overrightarrow{L_2} = \overrightarrow{A_2} - \overrightarrow{F_2}$ (where $\overrightarrow{A_1}$and $\overrightarrow{A_2}$ are the centroids of antennas 1 and 2, respectively, and $\overrightarrow{F_1}$and $\overrightarrow{F_2}$ the centroids of feeds 1 and 2, at a given point in time). The differential interferometric phase associated to changes in the antenna phase patterns, G_1 and G_2, is given by:

$$\Delta\phi = 2\,arg < G_1 > -(arg < G_1 > +arg < G_2 >) = arg < G_1 > - \,arg < G_2 >$$

It is easy to show that given a nominal (undistorted) set of these centroids, which we will term $\overrightarrow{A_1^N}, \overrightarrow{A_2^N}, \overrightarrow{F_1^N}, \overrightarrow{F_2^N}$ (superscript *N* for "nominal"), then the additional path length incurred by the antennas is:

$$\Delta L = \left(\left|\overrightarrow{L_2}\right| - \left|\overrightarrow{L_2^N}\right|\right) - \left(\left|\overrightarrow{L_1}\right| - \left|\overrightarrow{L_1^N}\right|\right)$$

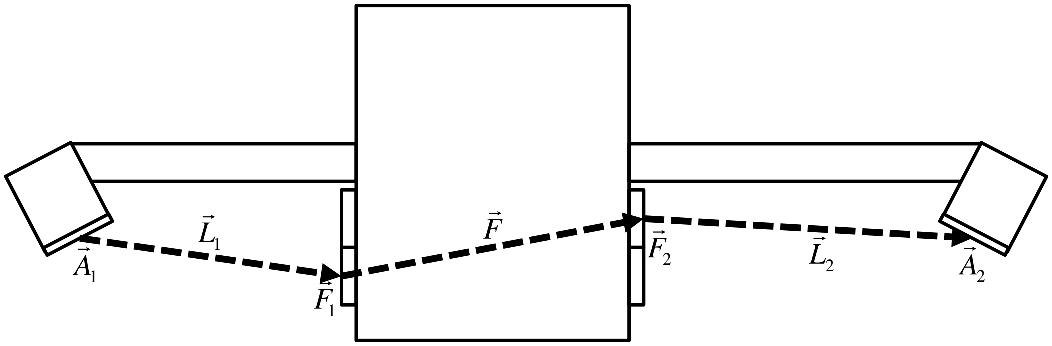

Figure 49. Geometry for the KaRIn feeds and antennas. Only one swath (polarization) description is shown. The figure shows a planar geometry but the vector definition is really in three-dimensional space. The red dots represent the mechanical centroids of the corresponding elements.

And therefore the differential interferometric phase is given by:

$$\Delta\phi = \frac{2\pi}{\lambda}\Delta L = \frac{2\pi}{\lambda}\left[\left(\left|\overrightarrow{L_2}\right| - \left|\overrightarrow{L_2^N}\right|\right) - \left(\left|\overrightarrow{L_1}\right| - \left|\overrightarrow{L_1^N}\right|\right)\right]$$

Using the same equation of the height error associated to a phase error derived above, we obtain that:

$$\Delta h = -\frac{\lambda\rho\sin(\theta)}{2\pi Bcos(\theta-\alpha)}\Delta\phi = -\frac{\rho\sin(\theta)}{Bcos(\theta-\alpha)}\Delta L$$

Therefore, the total error associated to mechanical distortions (including the mechanical effect on the antenna phase pattern) can be computed as:

$$\Delta h = -\frac{\rho\sin(\theta)}{Bcos(\theta-\alpha)}\Delta L - \frac{\rho}{B}\tan(\theta-\alpha)\sin(\theta)\,\Delta B + \rho\sin(\theta)\,\Delta\alpha$$

And therefore:

$$\Delta h = \rho \sin(\theta) \left[\Delta\alpha - \frac{\tan(\theta - \alpha)}{B} \Delta B + \frac{1}{B\cos(\theta - \alpha)} \Delta L \right]$$

Since:

$$\rho \sin(\theta) \approx C \left(1 + \frac{H}{R_E} \right)$$

where *C* is the cross-track distance, if desired one can approximate the expression above as:

$$\Delta h \approx C \left(1 + \frac{H}{R_E} \right) \Delta\alpha - \frac{C^2}{HB} \left(1 + \frac{H}{R_E} \right) \Delta B + \frac{C}{B} \left(1 + \frac{H}{R_E} \right) \Delta L$$

It is worth noting that C changes sign depending on the swath (left or right), which will change the sign of the roll and phase error contributions, but not that of the baseline effect due to the dependence with C^2.

This can be then flowed down as a PSD of a sub-allocation of the height error by considering the following approach:

- At every point in time, compute the height error as per the above equation at *N* points in the swath, from 10 to 60 km.
- For every point in the swath, collect the time series of the height error and compute the PSD. This results in *N* PSDs.
- Compute the average of the *N* PSDs to obtain the swath-average PSD.

Alternatively, one can look at linearizing the above expression with respect to the cross-track point *C* so as to be able to derive an approximation that can be integrated analytically. First, we estimate the best linear fit to a quadratic term in a least-squares sense. In order to be able to extract an analytical expression, we need to force the linear fit to go through the origin, therefore only fitting a best slope, β, which is given by:

$$\beta = \frac{\int_{0\,km}^{60\,km} C^3 dC}{\int_{0\,km}^{60\,km} C^2 dC} = 45 \cdot 10^3$$

and therefore, the best fit of this kind to a C^2 function from 0 to 60 km is given by $45 \cdot 10^3 C$ (expressed in units of meters), and shown in the figure below.

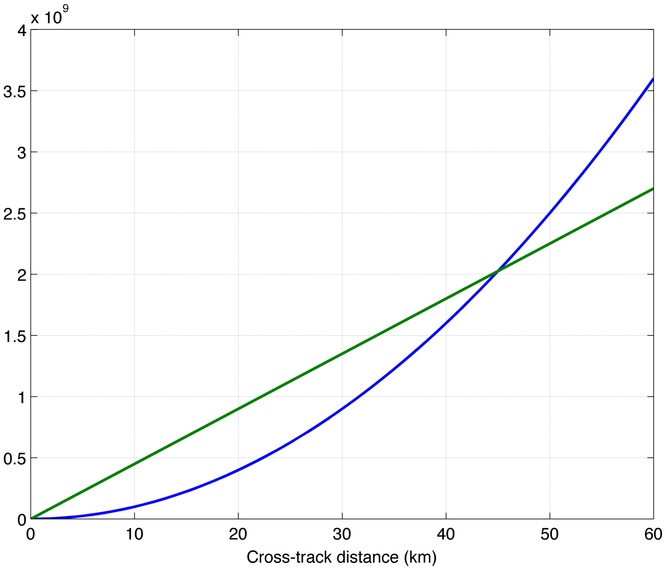

Figure 50. Approximation of the C^2 function as a slope

Without a priori knowledge of the time series, a qualitative estimate of how close the linear approximation is to the exact expression for the computation of the height PSD can be obtained as follows:

$$\frac{\int_{10}^{60}\left(\frac{C^2}{HB}\right)^2 dC}{\int_{10}^{60}\left(45\cdot 10^3\left(\frac{C}{HB}\right)\right)^2 dC} \approx 1.07$$

which indicates that the difference is sufficiently small. Using this approximation, the height error function can be expressed as:

$$\Delta h \approx C\left(1+\frac{H}{R_E}\right)\Delta\alpha - \frac{45\cdot 10^3 C}{HB}\left(1+\frac{H}{R_E}\right)\Delta B + \frac{C}{B}\left(1+\frac{H}{R_E}\right)\left(\left|\overrightarrow{\Delta L_2}\right| - \left|\overrightarrow{\Delta L_1}\right|\right)$$

With this approximation, we have that:

$$\Delta h \approx C\left(1+\frac{H}{R_E}\right)\left[\Delta\alpha - \frac{45\cdot 10^3}{HB}\Delta B + \frac{1}{B}\left(\left|\overrightarrow{\Delta L_2}\right| - \left|\overrightarrow{\Delta L_1}\right|\right)\right]$$

Given a time series of the height errors, $\Delta h(t)$, with a Fourier transform $\Delta H(\omega)$:

$$\Delta H(\omega) = \int_{-\infty}^{+\infty} C\left(1+\frac{H}{R_E}\right)\left[\Delta\alpha(t) - \frac{45\cdot 10^3}{HB}\Delta B(t) + \frac{1}{B}\left(\left|\overrightarrow{\Delta L_2(t)}\right| - \left|\overrightarrow{\Delta L_1(t)}\right|\right)\right] e^{-j\omega t} dt$$

the PSD is given by:

$$PSD\{\Delta h(t)\} = \lim_{T\to\infty}\frac{1}{T}E[|\Delta H(\omega)|^2]$$

and the swath-average PSD is given by:

$$PSD\{\Delta h(t)\} = \frac{1}{60\ km - 10\ km}\int_{10\ km}^{60\ km} \lim_{T\to\infty}\frac{1}{T}E[|\Delta H(\omega)|^2]\,dC$$

$$= \frac{1}{50\,km}\left(1+\frac{H}{R_E}\right)^2 PSD\{\widetilde{\Delta h}(t)\}\int_{10\,km}^{60\,km} C^2 dC = 1.87\cdot 10^9 PSD\{\widetilde{\Delta h}(t)\}$$

where:

$$\widetilde{\Delta h}(t) = \Delta\alpha(t) - \frac{45\cdot 10^3}{HB}\Delta B(t) + \frac{1}{B}\left(\left|\overrightarrow{\Delta L_2(t)}\right| - \left|\overrightarrow{\Delta L_1(t)}\right|\right)$$

$$= \Delta\alpha(t) - 4.97\cdot 10^{-3}\Delta B(t) + 0.1\left(\left|\overrightarrow{\Delta L_2(t)}\right| - \left|\overrightarrow{\Delta L_1(t)}\right|\right)$$

Perhaps a more readily expression with units of *asec* and μm is given by:

$$\widetilde{\Delta h}(t) = 4.848\cdot 10^{-6}\Delta\alpha(t)_{[asec]} - 4.97\cdot 10^{-9}\Delta B(t)_{[\mu m]}$$

$$+10^{-7}\left(\left|\overrightarrow{\Delta L_2(t)_{[\mu m]}}\right| - \left|\overrightarrow{\Delta L_1(t)_{[\mu m]}}\right|\right)$$

In summary, this approximation results in:

$$PSD\{\Delta h(t)\} = 1.87\cdot 10^9\ PSD\{4.848\cdot 10^{-6}\Delta\alpha(t)_{[asec]} - 4.97\cdot 10^{-9}\Delta B(t)_{[\mu m]}$$

$$+10^{-7}\left(\left|\overrightarrow{\Delta L_2(t)_{[\mu m]}}\right| - \left|\overrightarrow{\Delta L_1(t)_{[\mu m]}}\right|\right)\}$$

Based on the above derivation, the observatory allocation for dynamical stability phase, roll, and baseline is given by the following PSD:

$$E_{F/S}(f) = \begin{cases} 7.195\cdot f^{-2.17}\ cm^2/Hz, & 0.0065\ Hz < f \le 0.1367\ Hz \\ 0.0054\ cm^2/Hz\,, & 0.1367\ Hz < f \le 6.5\ Hz \end{cases}$$

This allocation is further sub-allocated as 95% to S/C and 5% to Payload (not including KaRIn).

5.5.5 Timing (Common Group Delay) Drift Errors

This system timing error corresponds in practice to a common group delay error. A system timing error δt will introduce a height error given by:

$$\delta h = -\cos(\theta)\,\delta r \approx \frac{c}{2}\cos(\theta)\,\delta t$$

where *c* is the speed of light, and θ is the look angle. Since KaRIn operates in a near nadir geometry, the look angle variation across the swath is small, and therefore a timing drift error has the effect, to first order, of creating a constant height bias across the swath. The RMS timing error for the swath average performance, ignoring the look angle dependence is thus given by:

$$\sigma_h^2 = \frac{\sigma_t^2}{(C_{max}-C_{min})}\int dC\left(\frac{c}{2}\cos(\theta_{look})\right)^2 = \sigma_t^2\left(\frac{c}{2}\right)^2$$

The timing error is allocated 10% of the overall systematic error. The flow-down of the timing error to all of the appropriate elements is shown in the figures below.

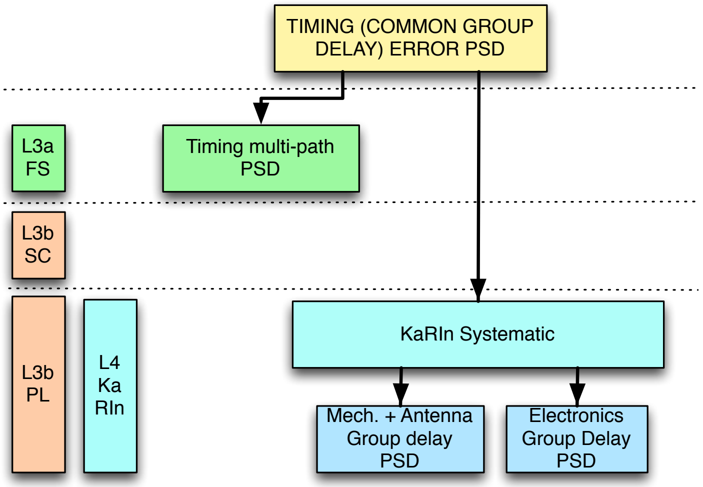

Figure 51. Conceptual high-level flow-down of the group delay PSD to the key mission elements.

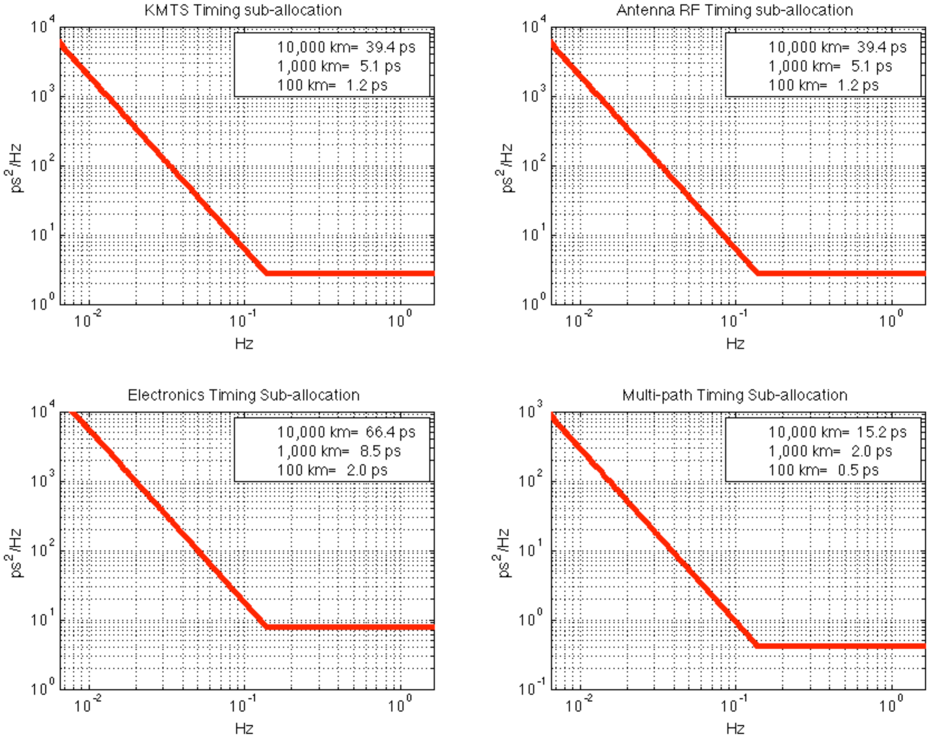

Figure 52. Sub-allocation of the group delay drift onto the different KaRIn elements (KaRIn Mechanical/Thermal System –KMTS-, Antenna, and Electronics) and the Flight System multi-path.

5.5.6 Radial Knowledge Errors

A radial knowledge error of δh directly translates into a height error of the same amount, since the desired topographic measurement assumes perfect knowledge of the orbit's altitude (hereafter we will use the term "POD error" to refer to the radial error in the orbit determination), and of the reference point of each instrument (as discussed in later in this section, there are several contributors to these knowledge errors, between variations in the overall CoG of the flight system and changes in the phase centers of the various instruments).

In order to characterize orbit errors at the spatial scales of interest, a simulation was performed to obtain the spectral density of the POD height error, including short wavelengths (down to ~ 250 km). The simulation used a model of the spacecraft shape, volume, and orientation along its orbit, and a worst-case solar flux (the maximum observed for year 2001), and the OSTM spacecraft attitude control system (ACS). The simulation also included surface forces, such as drag, solar and Earth radiation, and Earth gravity field. As a result, orbit deviations from the nominal can be obtained, and the simulated residual error from the onboard high-precision GPS (similar to the one flying on Jason-2) is derived. The long-wavelength results (down to 10,000 km) exhibit the typical peak that occurs at the once per revolution frequency. The medium-wavelength plot shows that starting at wavelengths of 5,000 km and lower, the error starts behaving quite accurately as a power law, and is becoming quite small. This is expected, since the GPS does not really resolve the orbit down to these short scales, and the error is purely the actual orbit deviation –and the knowledge error is really just the error in the integrator used for POD reconstruction. This effectively imposes a full dynamic POD, where the orbital motion of the S/C is strongly constrained by dynamic models, to minimize the noise of the integrator. A similar analysis was performed using the DORIS solutions. Both results are shown in the figures below.

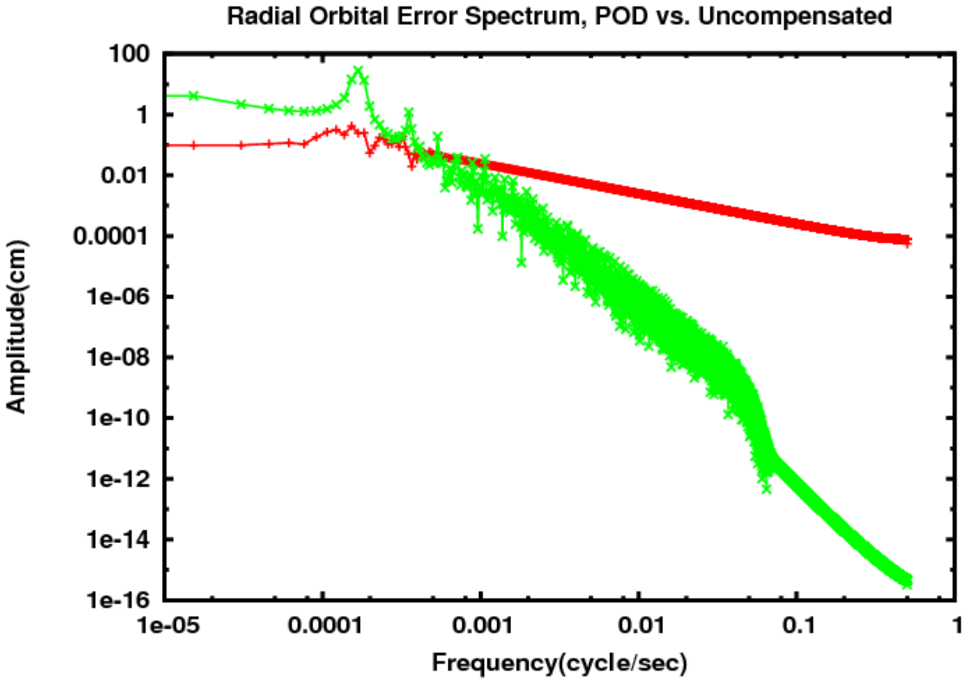

Figure 53. (green) theoretical radial orbital error spectrum due to the along-track perturbation without POD; (red) actual radial orbital error spectrum after POD using GPS, all error sources included. The two spectra intersect at about 3 cycle/rev. The POD solution does not reduce the high frequency errors, due to the GPS measurement noise and sampling rate.

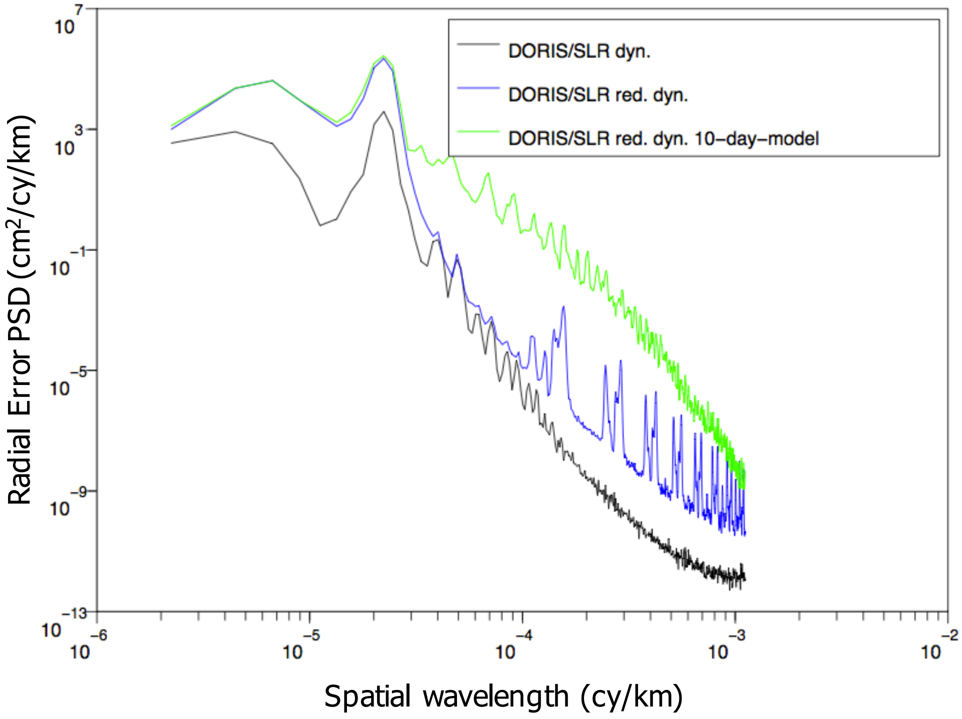

Figure 54. Spectral analysis of the radial differences between a degraded and a reference orbit solution. The degraded orbit corresponds to ENVISAT DORIS-only orbit computed with the EIGEN-GL04S-Annual gravity field with the drift terms removed. The reference orbit is the DORIS/SLR reduced dynamic orbit with the most up-to-date gravity field model (10-day Grace solution). The radial difference between the degraded orbit and the reference orbit gives insight into the radial error.

An additional term associated to height uncertainty appears due to drifts in the Flight System Center of Gravity (CoG). For example, deformations in the solar array panels and the payload structures, and fuel consumption, will displace the CoG in the POD solution from the reference CoG point that is used to make the height corrections.

Finally, an error terms appears due to deformations of the interferometric baseline, which could cause a drift in its radial center. These deformations appear mainly due to on-orbit thermoelastic effects.

The following constitutes the overall spectral envelope for the radial height error spectrum:

$$E_{Radial}(f) = 1.9631 \cdot 10^{-5} f^{-1.9922} \quad [cm^2/cy/km]$$

The integrated SSH error for wavelengths between 1 and 1,000 km for the derived envelope is 0.14 cm. This error is sub-allocated as 90% to the Flight System, and 10% to Algorithms for POD processing. Of the first 90%, 90% is further sub-allocated to the S/C as the major contributor to the uncertainty in the overall drift of the F/S CoG in the radial direction. Of the remaining 10%, 5% is sub-allocated to the Payload for changes in the CoG in the radial direction associated to payload distortions, and 5% to shifts in the radial height of the KaRIn interferometric baseline. The flow-down of the allocations is shown in the figure below.

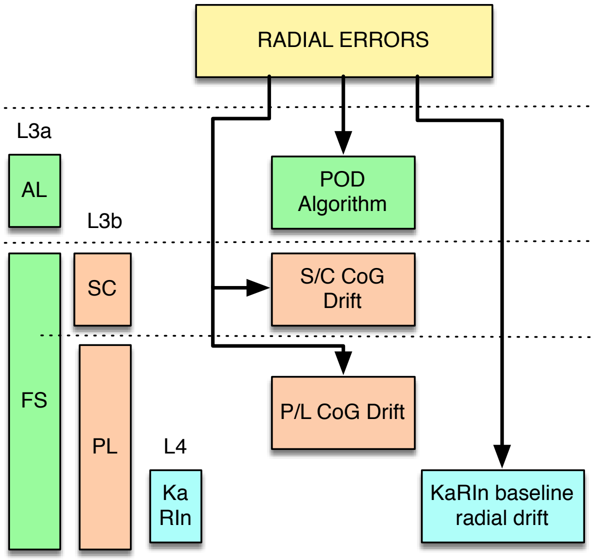

Figure 55. Flow-down of the Orbit height error.

The associated PSD, all expressed in cm^2/cy/km, are as follows:

$$E_{POD}(f) = 0.1 \cdot E_{Radial}(f) = 1.9631 \cdot 10^{-6} f^{-1.9922}$$
$$E_{FS\ CoG}(f) = 0.9 \cdot E_{Radial}(f) = 1.7668 \cdot 10^{-5} f^{-1.9922}$$

and the sub-allocations to the lower levels are:

$$E_{SC\ CoG}(f) = 0.9 \cdot E_{FS\ CoG}(f) = 1.59 \cdot 10^{-5} f^{-1.9922}$$
$$E_{PL\ CoG}(f) = 0.05 \cdot E_{FS\ CoG}(f) = 8.834 \cdot 10^{-7} f^{-1.9922}$$
$$E_{KaRIn\ radial\ drift}(f) = 0.05 \cdot E_{FS\ CoG}(f) = 8.834 \cdot 10^{-7} f^{-1.9922}$$

The figure below shows the PSD of all the components.

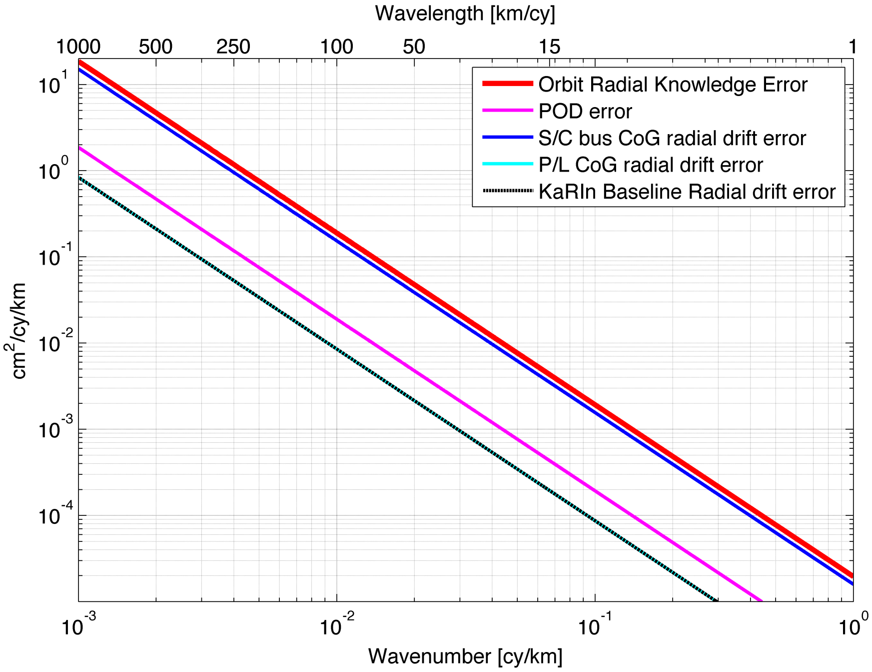

Figure 56. PSDs of the different contributors to the orbit radial height knowledge drift.

5.5.7 Wave Averaging Errors

The presence of surface gravity waves will introduce an additional source of height noise, since the average of the wave height over a 500 m x 500 m pixel will not be exactly zero. In this section we analyze this error source in detail, and show that the averaging introduces a small residual height error, which can be further reduced by simply using weighted averaging, which is implemented in the KaRIn Onboard Processor.

Real ocean wave spectra are a mixture of a continuous spectrum of wind-generated waves with swell, which is not generated by the local wind. For a continuous spectrum, the surface height can be written as

$$h(x) = \int dk\, a(k) e^{ik\cdot x}$$

where $k = 2\pi/\lambda$ is the wave-number, and *a(k)* is the complex wave amplitude, related to the wave spectrum, *S(k)*, by:

$$< a(k) a^*(k') >= \delta(k - k') S(k)$$

To obtain the average height over a given resolution cell of characteristic dimension L, we form the weighted average centered at coordinate x_0, given by:

$$\bar{h}(x_o) = \frac{1}{L} \int dx\, w(x - x_0) h(x)$$

where:

$$L = \int dx\, w(x)$$

and *w(x)* is the spatial weighting function. Defining *W(k)* as the Fourier transform of w(x), it is not difficult to show that the average height variance will be given by:

$$< \left(\bar{h}\right)^2 > \approx \int d^2\, k\, S(k) |W(k)|^2$$

The figure below shows the height error as a function of ocean wavelength for a Pierson-Moskowitz wave spectrum for a fully-developed sea in two cases: unweighted (rectangular) and weighted (Blackman-Harris) averaging.

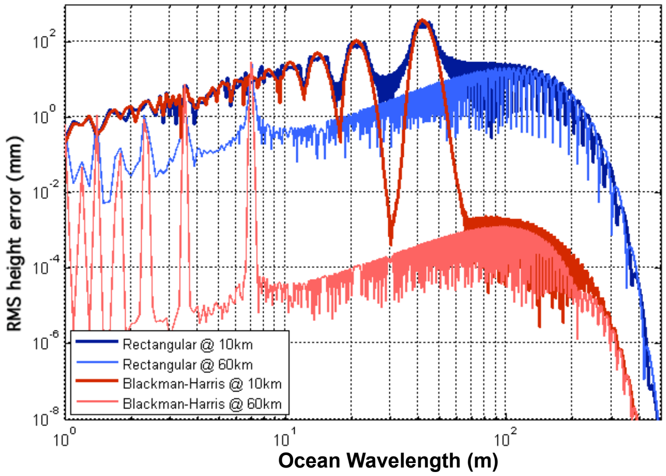

Figure 57. Height error as a function of ocean wavelength (in meters) using a Pierson-Moskowitz wave spectrum (not considering the effect of the instrument resolution).

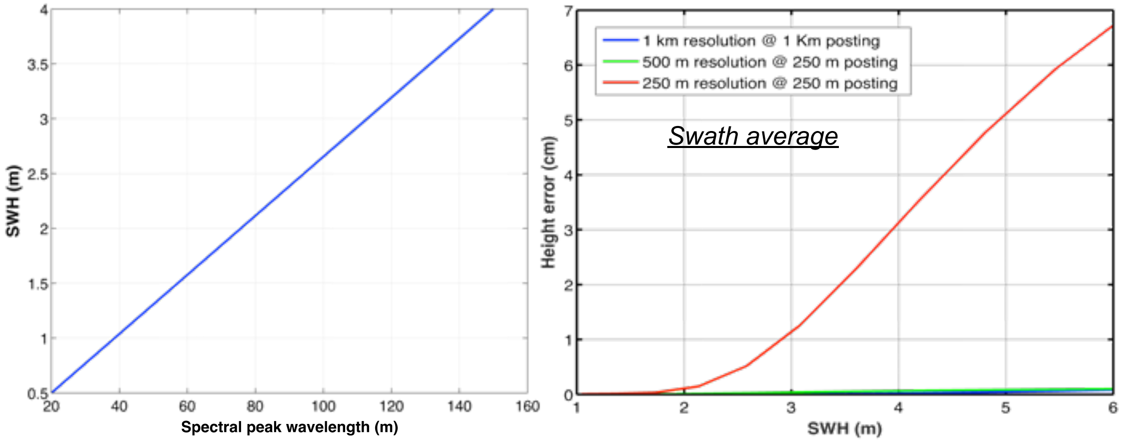

Figure 58. (left) Using a Pierson-Moskowitz wave spectrum, the relationship between ocean peak wavelength and SWH is shown; (right) for both 1 km and 500m pixels, the dominant wavelengths are far from the averaging pixel size, and therefore the error incurred is almost negligible for any SWH. For reference, the error is also shown $(250\ \text{m})^2$ pixels, where it quickly becomes comparable to the pixel size causing significant height errors.

This effect introduces height errors that are higher in the near-swath. Besides the fact that the number of cross-track pixels that can be averaged to form the 500 m x 500 m output pixel is smaller in the near swath due to the lower intrinsic resolution, a significant contribution to the overall error comes from the spectrum exhibiting numerous peaks at wavelengths smaller than 100 m, most remarkably at around 22 m and 43 m. This is in fact an aliasing effect that occurs when the wavelength, for a given look geometry, is such that $e^{ikx} = 1$, combined with the fact that the wave spectrum has a significant amount of energy in this wavelength region. The effect is worse at the near swath due to the lower incidence angle; at higher incidence angles, the peaks occur at much lower wavelengths, where the wave spectrum exhibits smaller amplitudes. In these cases, where the spectrum peaks, windowing cannot reduce the error.

However, the intrinsic resolution of the interferometer also needs to be taken into account, as the resolution at the near range is comparable to (or coarser than) these aliased wavelengths. In practice, this will smear the peaks and therefore reduce the error. Approximating the one-dimensional interferometric impulse response, $\chi(x)$, by a sinc-squared function of intrinsic resolution B_x (and ignoring here, for simplicity, the effect of the antenna pattern), the average height variance is now given by:

$$< (\bar{h})^2 > \approx \int d^2 k\, S(k) \left| W(k) \Lambda\left(\frac{B_x}{2\pi} k\right)\right|^2$$

where $\Lambda(k)$ is the Fourier transform of $\chi(x)$, i.e., the triangular function defined as $\Lambda(k) = \max(1 - |k|, 0)$. As a result, the system's limited resolution reduces the contribution of the wave spectra to within the range of wavelengths that can be resolved, effectively filtering out longer ones. The resulting residual error is large for the unweighted averaging case, where it reaches over 5 mm. However, using a Blackman-Harris weighting window lowers the residual error to negligible levels.

5.5.8 Processing and Bias correction errors

As previously discussed, the OBP will produce 9 different complex products from which a final averaged interferogram will be produced on the ground; as a result, a height map will be produced, among other products, on the ground.

As part of the ground processing, the following simplified set of corrections are required to compensate for some of the OBP simplifications and other error sources that introduce biases:

1. Remove the angular systematic bias that results from the iso-range lines and the iso-phase lines not being aligned.
2. Resample the beams to adjust for the different viewing geometries.
3. Compute heights for each beam correcting for the slightly different baselines.
4. Perform optimal beam averaging.
5. Resample the pixels to a fixed grid

Information on the spacecraft attitude will be needed to perform these corrections, as well as several basic static or quasi-static parameters (antenna phase screens, common and differential range delays, static roll angle, etc.), which will be obtained during the cal/val phase, or estimated periodically as needed.

A PSD for systematic errors associated to the algorithms used during ground processing to perform the bias and other corrections is allocated as 20% of the overall systematic errors, which is given by the following expression:

$$PSD_{alg}(f) = \begin{cases} 2.2 \cdot 10^{-6} f^{-2.5}, 0.021 > f \geq 10^{-3} cy/km \\ 3.42 \cdot 10^{-2}, \qquad f > 0.021\, cy/km \end{cases}$$

The spectrum integrates to 0.219 cm from 15 to 1,000 km, and is shown in the figure below.

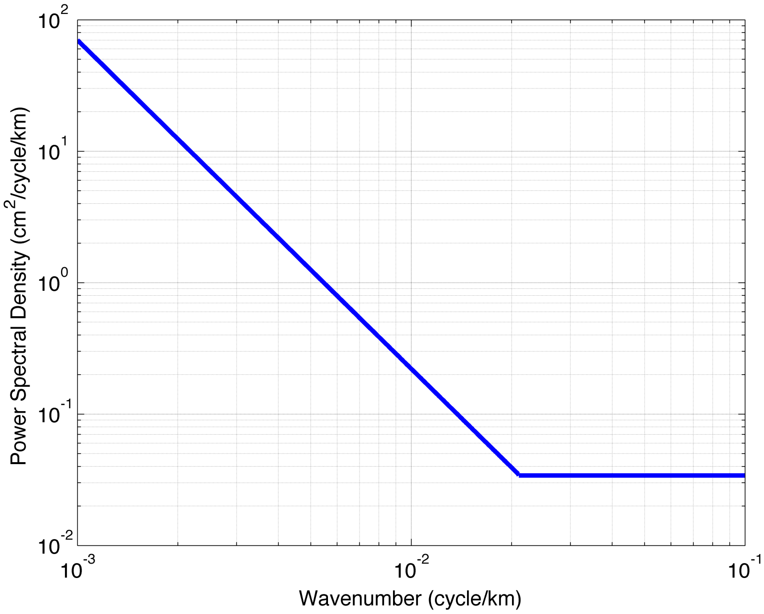

Figure 59. Sub-allocation of the systematic errors to Algorithms.

5.5.9 Wavelength drifts

While the initial transmit frequency of the radar will be measured and therefore known before launch, a drift over time of the KaRIn effective center frequency will introduce a height error given by the following equation:

$$\delta h = \mathrm{r}_0 \tan(\theta) \sin(\theta) \frac{\delta\lambda}{\lambda}$$

Factors such as drifts in KaRIn's reference stable oscillator (STALO), spectral filtering, and notching in the waveforms affect the effective wavelength. For KaRIn, the primary source of drift is introduced by the STALO. However, the system is designed to limit the long-term drift of the oscillator, achieving a $\delta\lambda/\lambda < 0.1\ \mu m/year$. In this fashion, this systematic error can be neglected, as it contributes < 0.2 mm of error.

6 HYDROLOGY MEASUREMENT REQUIREMENTS AND ERROR BUDGET

The error budget for hydrology can be split into three main sections: height errors, slope errors, and water classification errors. All of these are discussed in the following sections.

6.1 Height and slope accuracy requirements

The hydrology height error requirement is 10 cm for an area of 1 km^2. The derivation of the error budget follows the same methodology and structure as that of the ocean in terms of the top-level errors, which are separated between media, systematic, and random errors. The main differences for hydrology are that: 1) Sea State Bias errors over surface water are not considered since, with the exception of the Great Lakes region and other very large water bodies, the effects of SWH in rivers and other water bodies is considered to be negligible; 2) contrary to oceanography, there is an understanding that the requirements apply over time periods that are longer than a land pass. In order to be able to compute storage change, any drift between two given passes needs to be removed. This requires the use of calibration techniques (e.g., cross-overs), which are able to delete the time history of any drifts between two passes using optimal interpolation techniques.

The characteristics of the errors change depending on the direction. For height errors, the cross-track errors are dominated by the residual error after cross-over correction, leaving an uncorrected slope error going into the land pass that is not insignificant, whereas in an along-track sense, the slope is changing slowly. For slopes, the most significant error term is associated with the random noise of the measurement since, as will be discussed later, the derivative of a spectrally "flat" white noise becomes a red spectrum that grows as the square of the frequency.

A top-level break-down of the error budget is summarized in the table below.

Table 8. Top-level break-down of the hydrology error

Hydrology Error Component	**Height Error [cm]**	**Slope Error [μrad]**	**Comments**
Ionosphere signal	0.8	0.1	RMS of the full signal for maximum solar activity (100 TECU), using IONEX model
Dry Troposphere Signal	0.7	0.1	RMS after correction with weather models, based on Jason heritage
Wet Troposphere Signal	4.0	1.5	Model-based correction
Radial Component	1.62	0.5	Radial error RMS
KaRIn Random and Systematic Errors after Cross-Over Correction	8.9	15.5	Includes cross-over correction residual
Motion errors	0.8	1.6	Based on 1-sigma surface velocities of up to 2.6 m/s
Total Allocation (RSS)	**9.98**	**15.7**	**Total error, as allocated**
Unallocated margin RSS/SUM	0.65 / 0.02	6.6 / 1.3	
Total (RSS) Error	**10**	**17**	**Requirement**

6.1.1 KaRin Performance for Hydrology

The KaRIn performance over land surface water is again divided into systematic and random errors. The break-down of the overall KaRIn requirement is shown in the table below.

Table 9. Break-down of the KaRIn hydrology error

KaRIn Hydrology Error Component	**Height Error [cm]**	**Slope Error [μrad]**	**Comment**
KaRIn Random	4.4	15.3	Height based on a 1km^2 averaging area of water-only pixels; slope based on a 10 km downstream averaging of a 100 m ideal river.
KaRIn Systematic cross-track errors after cross-over correction	7.4	1.7	Residual after cross-over correction; these are the RMS cross-track slopes (and associated height) for the entire along-track land pass.
KaRIn Systematic along-track height bias error	1.5	0.08	This is the RMS timing and dilation along-track height errors accumulated down to 0 Hz.
High Frequency errors	1.15	0.5	RMS of systematic errors > 6.5 Hz
(Unallocated margin, RSS)	1.23	1.75	
Total (RSS) Error Requirement[1]	**8.9**	**15.5**	**Requirement**

6.2 Cross-over correction for Systematic Error removal

This technique exploits the fact that, at ocean cross-over points, a direct comparison can be made between KaRIn measurements, and that some of the interferometer systematic errors can be estimated (and therefore, reduced) from the cross-over differences themselves. The geometry of the cross-overs is illustrated in figure Figure 60. This approach can only use cross-over points over the oceans but, conceptually, has the effect of reducing any drifts incurred due to "past history" so that the absolute error over land throughout the mission only needs to consider the residual errors after this correction, plus any drifts accumulated over the land passes themselves.

For each cross over point, a cross over diamond grid, indicated by the dashed area, results from the overlap between an ascending and a descending pass. It is important to note that there are two relevant time scales involved: first, the time (or distance) separation between all of the adjacent cross-over points along the orbit that fall over the oceans. For the SWOT science orbit, this time (the separation between consecutive ocean cross-overs points) is always less than 80 sec, or ~500km, and it is a strong function of latitude. The second time scale is associated to the fact that a given cross-over point is formed by the intersection of two separate orbital ground tracks, which correspond to observations of the ocean that can be as far apart as several days. Assuming only passes that are within +/- half a cycle are used in forming the cross-overs, that results in a maximum separation of up to 11 days between the crossing swaths.

---

[1] Note that, the 8.9 cm is the total error after cross-over correction; the KaRIn-only height error and slope allocations, as will be discussed later, is 8.2 cm and 15.4 urad, respectively.

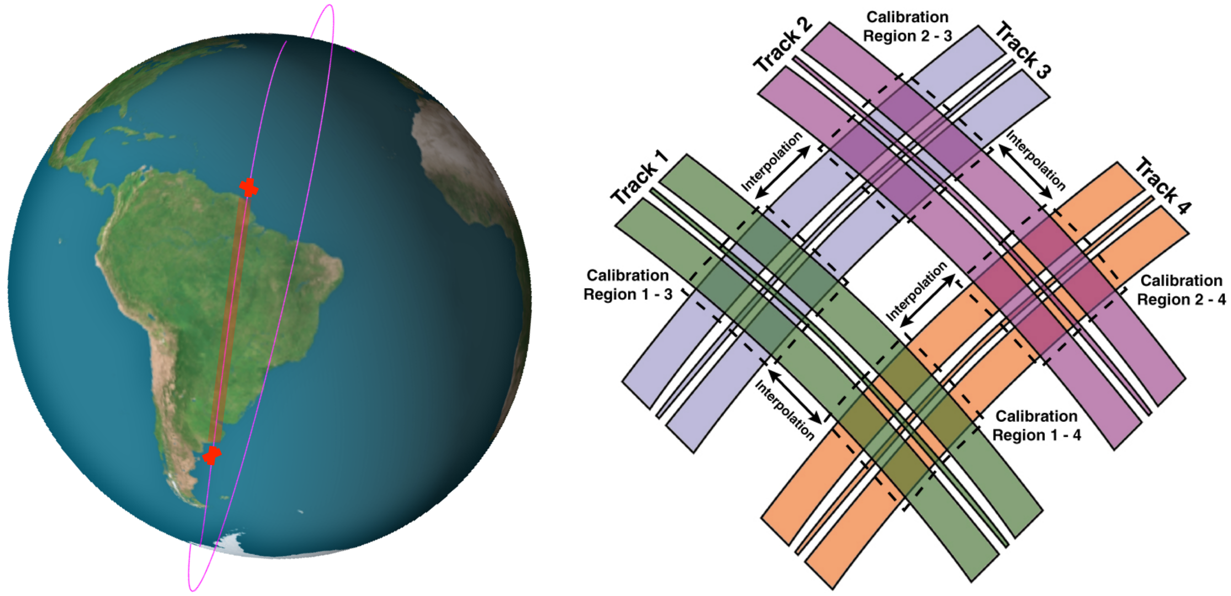

Figure 60. (left) Illustration of the closest cross-over points for a given land pass; (right) Illustration of the cross-over geometry. The diamonds where the slope errors are estimated are indicated by the dashed line; in between them, the slopes are interpolated.

The cross-over algorithm, in its most basic form, performs the correction in two distinct steps: 1) first, it estimates at every cross-over point, using a least squares fit, the equivalent cross-track slopes that the roll, phase, baseline, and other errors introduce; and 2) uses these estimates for all the cross-over points to perform an optimal interpolation and obtain the optimal slope throughout the orbit. Since the effect of a roll error and a phase error is effectively the same, i.e., to create a linear height error across the swath, the algorithm is not able to separate roll from phase errors, and a combined phase plus roll error is estimated. In addition, the phase and group delay errors may not generally be the same for both swaths, requiring the algorithm to estimate separate errors for each swath (left and right).

The accuracy of the estimated parameters depends on the number of cross-overs that can be used simultaneously in the estimation, their spatial and temporal separation, which as previously mentioned varies as a function of latitude, and the magnitude of the errors. The fundamental limitation to this technique is actually established by the decorrelation time of the ocean over the cross-over points used for estimation, which for the most part determines the minimum residual slope error that can be achieved (corresponding to roughly 0.8 urad). This also effectively limits the algorithm to using only cross-overs that are relatively close in time (within +/- half a cycle between the passes that form the cross-over point).

Initial results based on simulations indicate that the cross-over technique is able to remove systematic errors and meet the required residual error allocations. The figures below illustrate the results of using this technique, where the residual RMS over land is 1.4 urad (and the residual for the ocean is 0.7 urad).

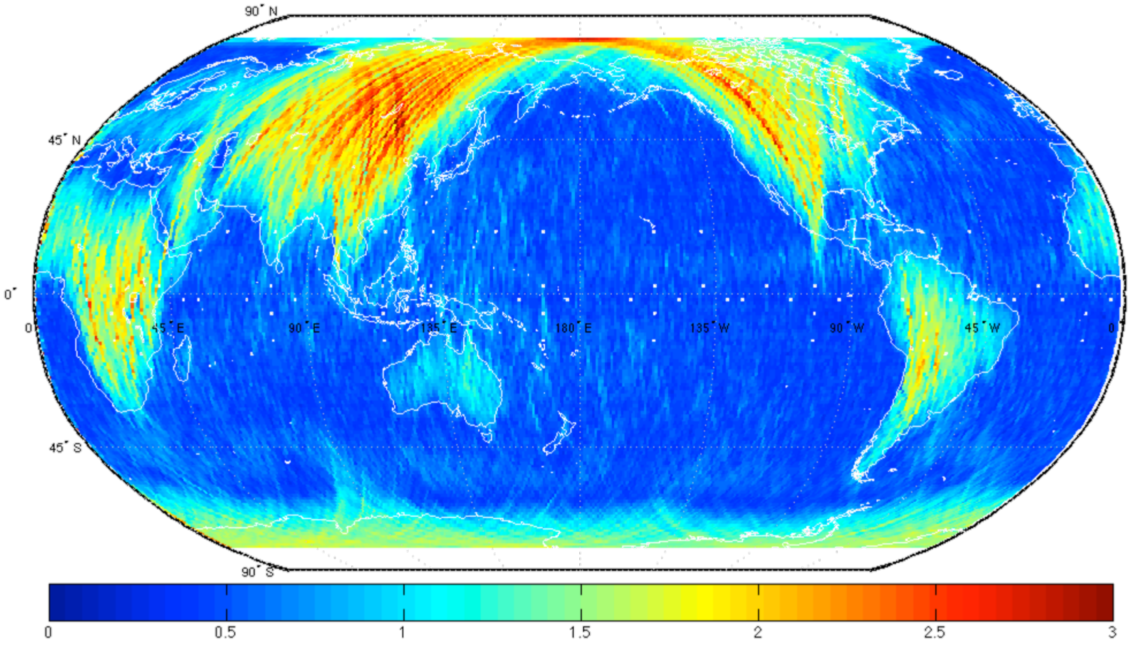

Figure 61. Illustration of the global residual systematic errors after cross-over correction.

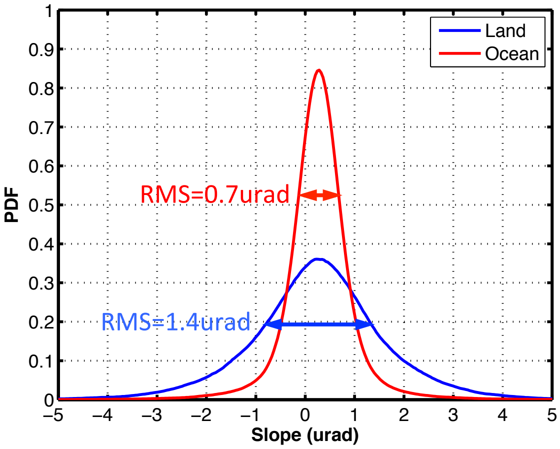

Figure 62. PDF of the residual cross-track slope error after cross-over correction, both over land (blue line) and over the oceans (red line). The associated RMS is 0.7 urad over the oceans and 1.4 urad over land.

We now consider the along-track error integrated over the land pass between cross-over points. An upper bound to the accumulated error can be obtained from simply integrating the power spectral density of the error. Considering that most errors follow a generic power law PSD given by

$$E(f) = Af^{-\alpha} \ ,$$

with α>1, the variance of the error accumulated over a pass of length L is bounded by:

$$\sigma_L^2 = \int_{1/2L}^{\infty} df \ Af^{-\alpha} = \frac{2^{\alpha-1}}{\alpha-1} AL^{\alpha-1}$$

for the particular case of α=2, this reduces to:

$$\sigma_L^2 = 2AL$$

For the error budget, the main quantity of interest is the RMS of the error for all the land passes. An effective pass length can thus be estimated from the above result, which will yield the effective length to be considered when retrieving the integrated error for all passes in an RMS sense. Given that the global RMS is given by:

$$\sigma^2 = \frac{\sum_n \left(\frac{2^{\alpha-1}}{\alpha-1} AL_n^{\alpha-1}\right) L_n}{\sum_n L_n} = \frac{2^{\alpha-1}}{\alpha-1} A \frac{\sum_n L_n^{\alpha}}{\sum_n L_n}$$

the effective pass length is thus:

$$L_{eff} \approx \left(\frac{\sum_n L_n^{\alpha}}{\sum_n L_n}\right)^{\frac{1}{\alpha-1}}$$

which for α=2 reduces to:

$$L_{eff} \approx \left(\frac{\sum_n L_n^{2}}{\sum_n L_n}\right)$$

While this derivation can provide useful initial estimates of what pass lengths matter, the most accurate results can only be obtained by performing analytical simulations that account for the actual land passes in the actual SWOT science orbit. Such an analysis reveals that the optimal interpolator acts indeed as a filter with an equivalent transfer function approximated by a high pass filter that rolls off very fast (40 dB/decade) for spatial scales longer than 12,500km (~ 32 min, or 5.2e-4 Hz), as shown in the figure below. Therefore, the KaRIn requirements extend the height error PSD beyond the ~3 min time scales and to 32 min (with a higher slope), to meet the overall requirement, which integrated to an allocation of 8.2 cm. The 8.9 cm value reported on the table on section 6.1 corresponds to the integrated value over the full global length scale (i.e. past the 12,500 km scales). The difference from 8.2 and 8.9 cm therefore accounts for the error associated to scales longer than 12,500 km which, while being heavily filtered by the roll off of the filter response, they still account for a small additional error. Similarly, for the slope requirement, the KaRIn allocation is 15.4 urad whereas the total requirement, which includes scales longer than 12,500 km, is 15.5 urad. Initial results based on a prototype implementation of the cross-over correction algorithm demonstrate not only the feasibility of achieving the required filter cut-off, but also that the equivalent filter response can in practice achieve improvements starting at scales as short as ~3,000 to 4,000 km for the nominal science orbit. These results are also shown in the figure below.

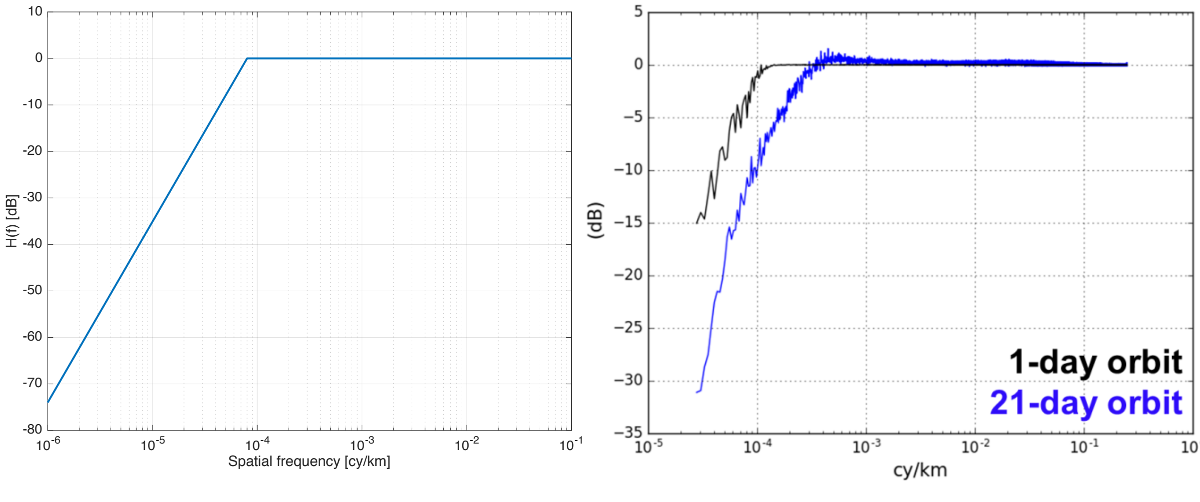

Figure 63. (left) analytical spectral response of the effective filter resulting from applying cross-overs. Effectively, it is a high pass filter that rolls off very fast (40 dB/decade) for spatial scales longer than 12,500km (~ 32 min, or 5.2e-4 Hz). (right) response obtained from simulations based on the initial cross-over correction algorithm, shown for both the 21-day nominal science (blue curve) and the 1-day cal/val orbits (black curve).

It is also important to note that the cross-over correction obtains a slope at cross-over points, and therefore is not automatically eliminating height biases that will result from integrating some of the drifts over long periods of time. While relative height biases between passes at cross-over points could also be estimated, this approach has limitations due to the inherent variability of the ocean. Instead, the algorithm needs to use the coincident nadir altimeter measurements, averaging them for relatively long durations as required so as to reduce the random error of the altimeter (the vast majority of the nadir altimeter error is random, and not drifts, as demonstrated by its capability in the Jason series to track sea-level rise). Therefore, the KaRIn measurements in the near swath will be averaged for the same durations, and corrected to follow the nadir altimeter height measurements, thereby reducing height errors associated to long-term drifts to very small levels.

6.3 Hydrology Random Error Requirements

6.3.1 Height Error

In order to establish the random error performance, several studies were conducted to determine the brightness of the surface water bodies at Ka-band and for SWOT's range of incidence angles. The two figures below show two separate results, the first from measured sigma0 values from the Global Precipitation Mission (GPM), which is representative of large inland water bodies, given GPM's resolution, and the second from high-resolution measurements of smaller water bodies collected by the AirSWOT instrument. In all cases, the 32 percentile sigma0 over SWOT's range of incidence angles is generally brighter than 10 dB. Therefore, hereafter and for the purposes of the hydrology error budget, we will consider a flat sigma0 of 10 dB across the swath.

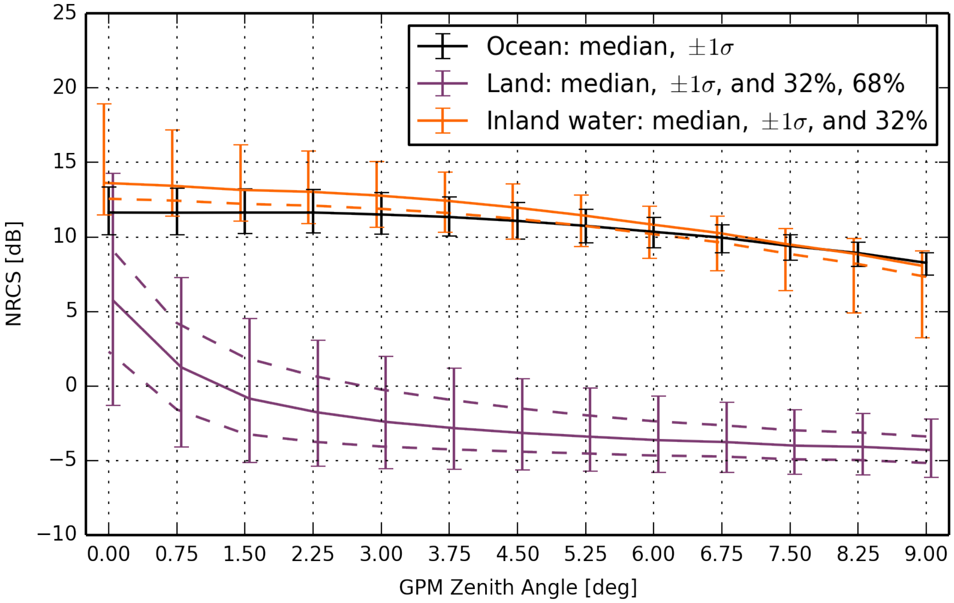

Figure 64. Ocean, land, and inland water measured sigma0 from the Global Precipitation Mission (GPM), which includes a Ka-band radar scanning ±9 deg around nadir, for a ground resolution of ~5 km at nadir.

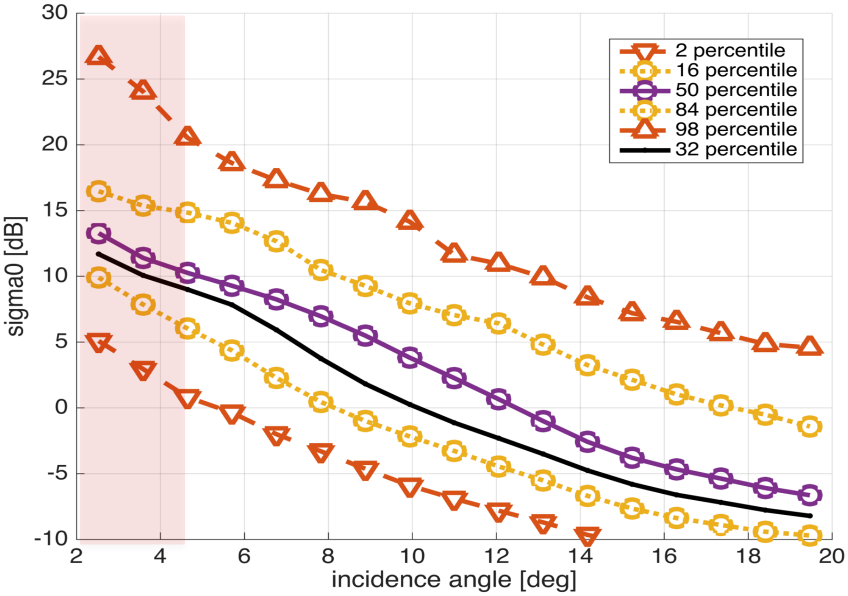

Figure 65. Different percentiles of sigma0 measured by the AirSWOT instrument over smaller water bodies (includes about 9,000 water bodies, rivers, and lakes obtained from flights in Alaska, Sacramento, New Orleans, and Tahoe).

Considering the fact that over land, KaRIn performs azimuth pre-summing by a factor of 2.1 and BFPQ to 3 bits, and given a constant 10 dB of sigma0 for water brightness, the Noise-Equivalent Sigma0 and the random performance across the swath are shown in the figures below. The swath average (10 km to 60 km) height error performance is 3.5 cm (including SNR margin).

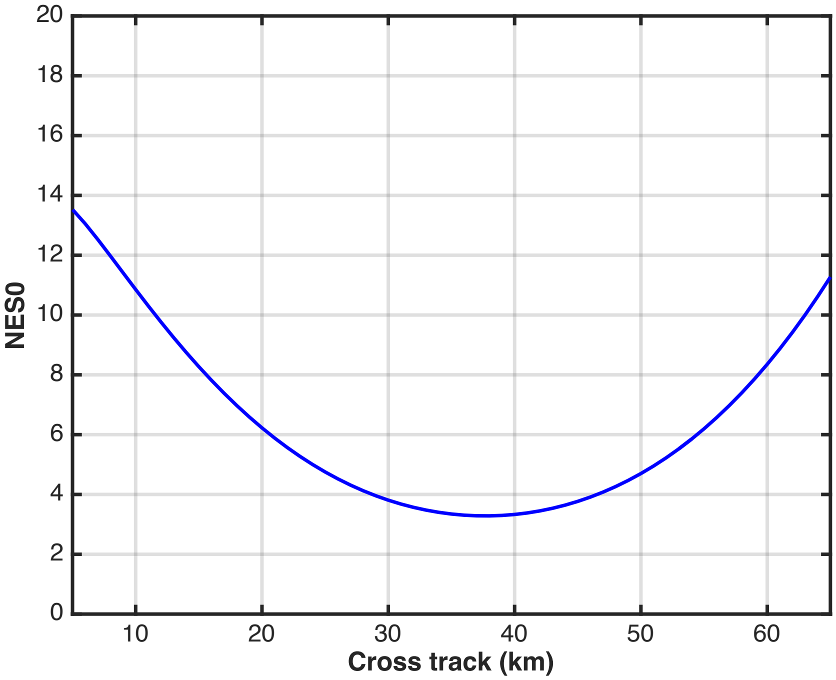

Figure 66. KaRIn Noise Equivalent Sigma0 over land for a flat water sigma0 of 10 dB across the swath.

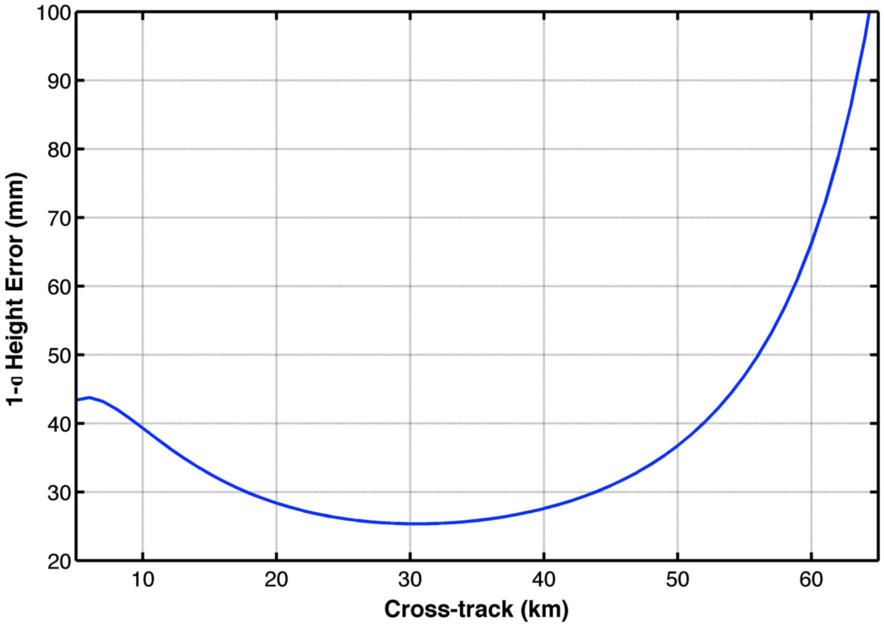

Figure 67. KaRIn random performance across the swath (requirement is specified from 10 to 60 km).

6.3.2 Slope Error

The slope requirement is dominated by the high-frequency noise of the KaRIn system. Considering a river or surface water body of width W and length L, the scaling of the random error from 1km^2 to its area $A = WL$ is thus given by:

$$\sigma_A^2 = \sigma_{1km}^2 \frac{1\,km^2}{WL}$$

The formulation of fitting a straight line to the paired observations $\{x_i, y_i\}$ (in our case, position and height measurements) is well established and has been documented in the open literature innumerable times. Under the assumptions that: 1) all N pixel measurements have the same uncertainty; and 2) only uncertainties in y (and not in x) are important, one can find the best-fit values of y_0 and b of the linear regression $f(x) = y_0 + bx$ are given by the minimization of the associated cost function:

$$\gamma^2 = \sum_i \frac{(y_i - y_0 - bx_i)^2}{\sigma^2}$$

The solution to the minimization process results in:

$$b = \frac{\overline{xy} - \bar{x}\bar{y}}{\overline{x^2} - \bar{x}^2}$$

and:

$$y_0 = \frac{\bar{y}\overline{x^2} - \bar{x}\,\overline{xy}}{\overline{x^2} - \bar{x}^2}$$

The uncertainty in the fit parameters, the error matrix, can be determined from the inverse of the information matrix *H* obtained from the derivatives of the γ^2 function, and are given by:

$$\sigma_{y_0}^2 = \sigma^2 \left(\frac{\overline{x^2}}{N\left(\overline{x^2} - \bar{x}^2\right)} \right)$$

$$\sigma_b^2 = \sigma^2 \left(\frac{1}{N\left(\overline{x^2} - \bar{x}^2\right)} \right)$$

In our case, we are after the uncertainty in the slope error, given by σ_b^2. If there are N_{xt} pixels in the cross-track direction, and N_{at} pixels in the along-track direction, then $N = N_{at}N_{xt}$, and

$$\sigma^2 = \sigma_{1\,km}^2 N_{xt} N_{at}$$

Hereafter we will assume that the points are equally spaced[2] and, without any loss of generalization, centered on 0 such that $\bar{x} = 0$:

$$x_n = -\frac{L}{2} + \frac{L}{2N_{at}} + \frac{L}{N_{at}} n \, , n = 0, \ldots, N_{at} - 1$$

Note there are N_{xt} sets of each of the above. Given this, it is simple to show that:

$$x_n^2 = \frac{L^2}{N_{at}^2} \left(n^2 - (N_{at} - 1)n + \frac{(N_{at} - 1)^2}{4} \right)$$

and therefore:

$$\frac{1}{N_{at}} \sum_n x_n^2 = \frac{\frac{L^2}{12}\left(N_{at}^2 - 1\right)}{N_{at}^2}$$

As the number of points tends to infinity, the above expression tends to $\frac{L^2}{12}$, and we finally obtain:

$$\sigma_b^2 = \sigma_{1km}^2 \frac{1\,km^2}{WL} \frac{12}{L^2} = \sigma_{1km}^2 \frac{12}{L^3 W}$$

Perhaps the most interesting outcome of this derivation is that the error decreases inversely proportional to the water body area plus a L^2 factor; while white random noise decreases strictly with the area, the slope error is a red spectrum, and therefore the error decreases significantly faster with the length of the water *L*. This fact is illustrated in the figure below, where the dependence of the linear-regression slope error as a function of river width and length is shown. For a $\sigma_h{}^{(1\,km)} = 4.4\ cm$, the standard deviation of the slope, σ_{slope}, is 15.3 μrad.

---

[2] Although this will rarely be the case for real rivers in SWOT data, generally constitutes a reasonable simplification for the purpose of the error analysis.

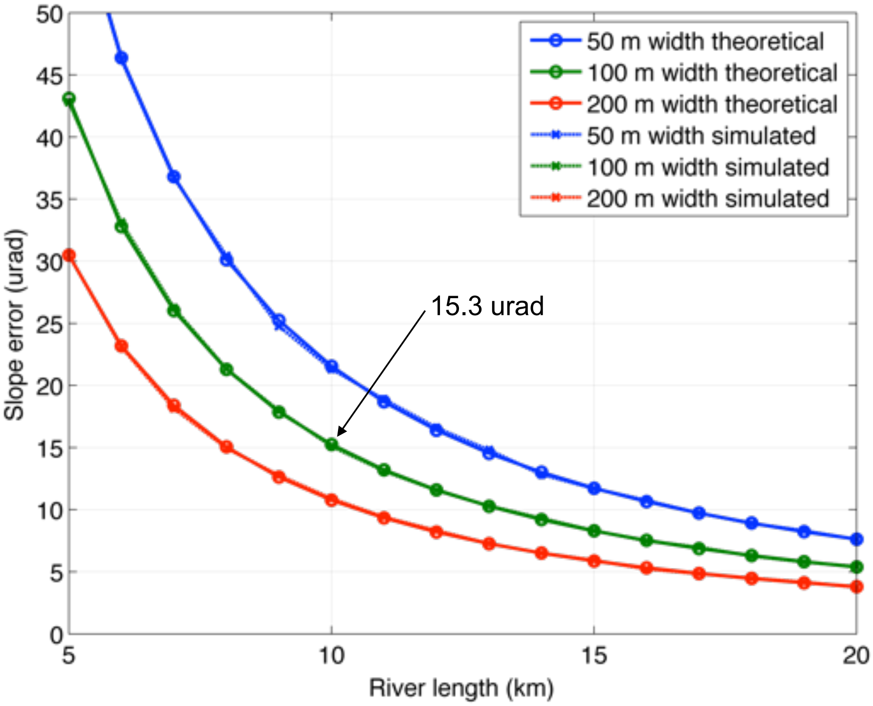

Figure 68. Slope error as a function of averaging length for different widths (not including systematic or media errors)

While the above allocation of 15.3 urad will be used in the error budget and is directly responsive to the wording of the science requirement, it is important to note that real-world rivers reaches are not well characterized by the idealized concept of a 10 km x 100 m rectangular shape, and that in reality the following factors will have some play in the actual performance:

1) Rivers exhibit variations in their width along the reach. Due to the dependency of the error on $\frac{1}{WL^3}$, slope estimates are most sensitive to variations in width near the ends of the reach. Intuitively, this effect can be easily understood: a narrowing at the reach boundaries implies losing samples that have the largest possible pairwise separation in L. Therefore, the estimation error increases even if more samples are available around the center of the reach, since their effective separation is smaller. In contrast, the height estimation is not sensitive to this effect because the error scales as $\frac{1}{WL} = \frac{1}{Area}$; therefore, provided the total area is preserved, the number of samples available for height estimation remains the same regardless of how they are distributed along the reach. Estimates based on a study of several single-channel real-life river reaches indicate that the typical river width variability is within 30%.
2) Rivers can have islands and may break into multiple channels within a reach, making the definition of the mean width for evaluating performance requirements difficult to interpret.
3) Water body classification will use an algorithm, which will be unequivocally subject to false alarms (adding land-contaminated pixels) as well as miss rates (removing available water pixels). While not necessary for estimating area extent, eroding (or weighting) the heights around the river edges may be necessary to mitigate the effect of land-contaminated pixels, which carry different height information than that of the river depending on the river

morphology and surrounding topography (including natural or artificial levees, where present). Of course, for the narrowest rivers (and in the near-swath, where the cross-track resolution of KaRIn increases to ~60 m, becoming comparable to the requirement of 100 m river width), the error caused by removing pixels may be larger than the error introduced by land contamination.

4) There are additional geophysical considerations that may impact the expected level of performance, including: 1) the decorrelation time of the water (the time the observed water stays coherent so as to enable synthesizing an along-track resolution comparable to the intrinsic resolution capability of the instrument). Just like a camera, if things move within the shutter speed (i.e., the exposure time), the resolution is degraded –an effect commonly referred to as a “blurred image”. Similarly, a rapid temporal decorrelation of the scene will limit the azimuth resolution of KaRIn. Note the number of independent observations for a given pixel and hence, speckle reduction, is independent of temporal correlation, and so while the decorrelation time is not a threat to the height accuracy of water-only pixels, it can impact the detection of the edges of water bodies; 2) the impact of vegetation; in-water vegetation has the potential to attenuate the transmitted signal and therefore reduce the signal-to-noise ratio and increase the random error; also, both vegetation inside the water bodies and in close proximity will produce layover onto the water pixels and affect the height and slope estimates; 3) the impact of land-to-water layover.

6.4 Systematic errors

The overall flow-down of the key systematic errors across mission elements is shown in the figure below, with every component discussed in the following sections.

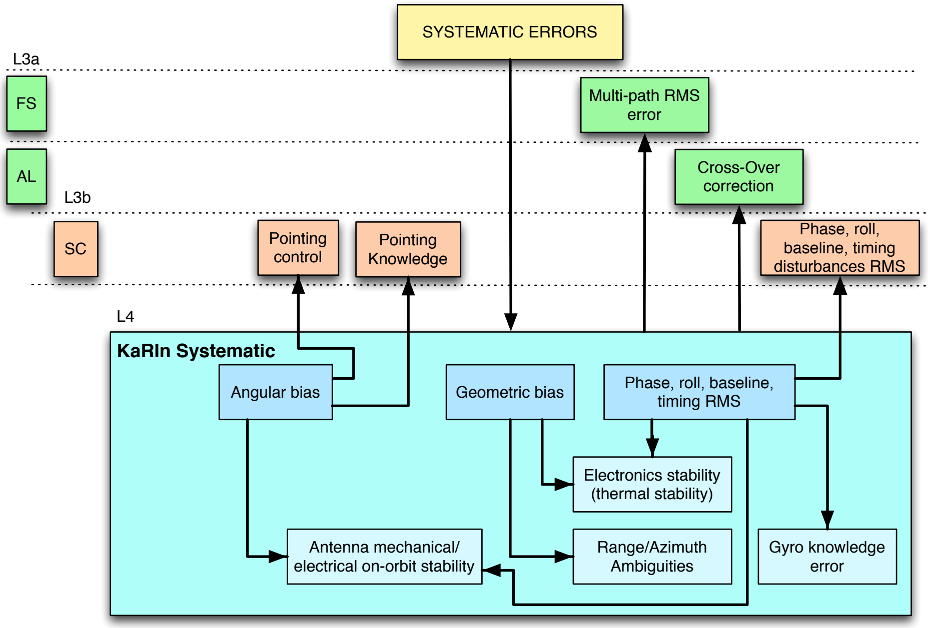

Figure 69. Conceptual high-level flow-down of the systematic error to the key mission elements.

The flow-down is similar to the ocean; the difference here is that: 1) the errors are not expressed as a PSD since specifying how the errors are temporally accumulated is not relevant, rather only that the individual integrated error allocations over the effective pass length is met; given that the effective pass length is greater than 1,000 km, the allocations constitute separate requirements from the ocean spectra; and 2) in forming the high resolution images for surface water bodies, it is necessary to impose additional constraints on systematic errors causing errors on scales shorter than 1 km (i.e. frequencies >6.5 Hz). This will constitute “high-frequency” error allocations, formulated as the equivalent of integrated RMS for frequencies from 6.5 Hz to infinity. The expected source of these errors is not thermoelastic effects, rather disturbances such as the ones generated by the S/C bus reaction wheels, solar array rotations, etc.

The derivation of the systematic errors starts from the PSD of the systematic errors that is required for the ocean, and for scales larger than 1,000 km, the systematic error is allowed to grow at a faster slope, to balance the errors across the error budget. The expression of the overall systematic error PSD is given by:

$$E_{systematic}(f) = \begin{cases} 2.21 \cdot 10^{-6} f^{-2.733}, & f \leq 10^{-3}\ cy/km \\ 1.1 \cdot 10^{-5} f^{-2.5}, & 0.021 > f \geq 10^{-3}\ cy/km \\ 1.71 \cdot 10^{-1}, & f > 0.021\ cy/km \end{cases}$$

Following the way the ocean requirements are sub-allocated, the break-down of the systematic requirements is as follows: 60% to differential phase drift, 20% to baseline roll, 5% to baseline dilation, and 10% to timing (5% left as unallocated margin), while the gyro knowledge error is allocated separately. Note that these are notional sub-allocations since the requirement, as previously discussed in the ocean section, the allocation of these errors is performed at the height error level. However, the different contributions are derived here separately for guidance.

The along-track slope errors can be obtained for every systematic error component by integrating its spectrum in a similar fashion as what was done for the random error, i.e.:

$$\int_{1/2L_{eff}}^{\infty} df\ Slope_{systematic}(f) = \int_{1/2L_{eff}}^{\infty} df\ (2\pi)^2 f^2 \left(\frac{10\ \mu rad}{cm/km}\right)^2 E_{systematic}(f)$$

This results in the following top-level allocations, where $2L_{eff}$=12,500 km is imposed, corresponding to a time duration of ~32 min.

Table 10. Break-down of the systematic errors

Systematic Error Component	Height Error [cm]	Along-track Slope Error [μrad]	Comments
Roll error	0.94	0.096	These errors are corrected by cross-overs and the residual (uncorrected) error is the RMS integrated up to 7,000 km (0.00092 Hz)
Phase error	1.63	0.166	
Gyro roll knowledge error	1.30	0.230	
Baseline dilation error	0.47	0.048	These errors are not corrected by cross-overs and therefore these are the RMS integrated down to 0 Hz.
Timing error	0.67	0.068	
Total Systematic Error (RSS)	**2.4**	**0.3**	

From the perspective of the high-frequency errors, there are different scenarios that need to be taken into account, depending on how the river is aligned with respect to the flight track. The bounding cases appear when considering that the river is either parallel, or perpendicular, to the flight track, as illustrated in the figure below.

Figure 70. Illustration of the two cases considered for high frequency slope errors for a river (represented by the black surface), where one reach is aligned in the flight direction and the other one perpendicular to it.

In cases where the river is roughly oriented perpendicular to the flight direction, and for relatively small river widths, a high frequency disturbance will basically introduce an instantaneous, constant slope error across the reach length, which can be seen as an additional cross-track slope in addition to the residual slope after cross-over correction. As such, and approximating for the moment that all error sources (phase, baseline, and roll) contribute solely as a linear slope, the error is simply given by the integral of the PSD of the height error, as an effective RMS for frequencies greater than 6.5 Hz, converted to an angle by dividing by the equivalent cross-track distance, $\bar{C}$.

$$\left(\sigma_{slope}^{HF}\right)_{cross-track}^{2} = \frac{1}{\bar{C}^2}\int_{6.5\ Hz}^{\infty} df\ E_{systematic}(f)$$

In cases where the river is roughly oriented in the flight direction, the disturbances really need to be considered as a slope spectrum given by:

$$\left(\sigma_{slope}^{HF}\right)_{along-track}^{2} = \int_{6.5\ Hz}^{\infty} df\ (2\pi)^2 f^2 \left(\frac{10\ \mu rad}{cm/km}\right)^2 E_{systematic}(f)$$

However, the slope will not be estimated by integrating the along-track spectrum. In its most basic form, the algorithm to estimate the slopes will use a linear fit to the height measurements over a distance of 10 km for every line of high-resolution pixels within the river width. Effectively, this can be seen as a low-pass filter that will remove any high-frequency components corresponding to wavelengths shorter than 1 km. Therefore, the effect on the slopes of these high-frequency terms can be neglected, given that they are already bounded by the errors introduced in the cross-track direction.

The requirements integrated from 6.5 Hz to 5.2e-4 Hz (~32 min) are thus as follows:

- Roll: 45 masec (1-sigma), sub-allocated as 14 masec (1-sigma) to the Flight System for disturbances, and 43 masec (1-sigma) to KaRIn.
- Phase: 161 mdeg (1-sigma), sub-allocated as 32 mdeg (1-sigma) to the Flight System for disturbances, and 158 mdeg (1-sigma) to KaRIn.
- Baseline: 21 um (1-sigma), sub-allocated as 6 um (1-sigma) to the Flight System for disturbances, and 20 um (1-sigma) to KaRIn.
- Timing: 44.7 ps (1-sigma), only sub-allocated to KaRIn.
- Gyro: the gyro knowledge error is sub-allocated 0.065 masec (1-sigma), only sub-allocated to KaRIn.

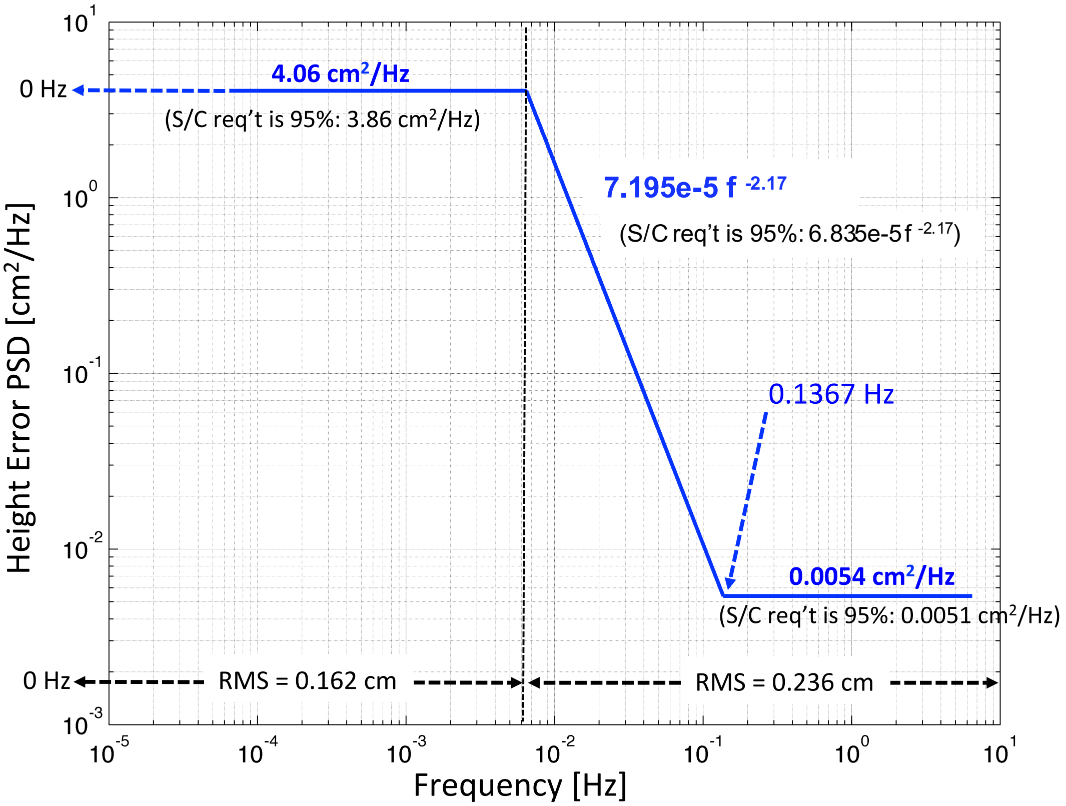

Figure 71. F/S Disturbance PSD requirement for the F/S (excluding KaRIn), and sub-allocations to the S/C.

For the F/S (non-KaRIn) elements, the requirement is expressed as the same PSD requirement as that of the ocean for scales shorter than 1,000 km, and a not-to-exceed power spectral density of 4.06 cm^2/Hz for longer wavelengths:

$$E_{F/S}(f) = \begin{cases} 4.06\,cm^2/Hz, \quad f < 0.0065\,Hz \\ 7.195 \cdot 10^{-5} \cdot f^{-2.17}\,cm^2/Hz, \quad 0.0065\,Hz < f \le 0.1367\,Hz \\ 0.0054\,cm^2/Hz\,, \quad 0.1367\,Hz < f \le 6.5\,Hz \end{cases}$$

At the other end of the spectrum, the high-frequency (>6.5 Hz) RMSs are derived from allowing each error to create a maximum of 1.15 cm height error at the equivalent center of the swath, which is 37.9 km, as derived in the ocean section. For a roll, this means:

$$\delta\theta_{roll} \approx 10^{-5}\left(\frac{648000}{\pi}\right)\frac{\delta h_{[cm]}}{C_{[km]}}\left(1+\frac{h}{R_E}\right)^{-1} = 47.6\,\delta h_{[cm]} \quad [masec]$$

and therefore the roll allocation is an overall RMS error of 34 milliasec. For phase, the error is:

$$\delta\phi \approx 10^{-2}\,\frac{180}{\pi}\left(\frac{B_{[m]}k_{[m]}}{C_{[km]}}\right)\left(1+\frac{h}{R_E}\right)^{-1}\delta h_{[cm]} = 98.9\,\delta h_{[cm]} \quad [mdeg]$$

For baseline dilation the error is:

$$\delta B \approx -10^{-2}\left(\frac{B_{[m]}H_{[m]}}{C_{[km]}^2}\right)\left(1+\frac{h}{R_E}\right)^{-1}\delta h_{[cm]} = -56\,\delta h_{[cm]} \quad [\mu m]$$

where B is 10 m.

The high-frequency (>6.5 Hz) RMS errors are allocated as follows:

- Roll: 34 masec (1-sigma) to the Flight System, sub-allocated as 30 masec (1-sigma) to S/C bus and 16 masec (1-sigma) to KaRIn.
- Phase: 71 mdeg (1-sigma) to the Flight System, sub-allocated as 50.2 mdeg (1-sigma) to S/C bus, and 50.2 mdeg (1-sigma) to KaRIn.
- Dilation: 24 um (1-sigma) to the Flight system, sub-allocated as 20 um (1-sigma) to S/C bus and 13 um (1-sigma) to KaRIn.

The associated height errors for each element are shown in the table below.

Table 11. Break-down of the high frequency errors

High-frequency (>6.5 Hz) Error Component	**F/S allocation**	**S/C bus sub-allocation**	**KaRIn sub-allocation**
RMS Roll > 6.5 Hz	34 masec	30 masec	16 masec
(Height error) (Cross-track slope error)	(0.71 cm) (0.19 urad)	(0.63 cm) (0.17 urad)	(0.33 cm) (0.09 urad)
RMS Phase > 6.5 Hz	71 mdeg	50.2 mdeg	50.2 mdeg
(Height error) (Cross-track slope error)	(0.72 cm) (0.19 urad)	(0.51 cm) (0.135 urad)	(0.51 cm) (0.135 urad)
RMS Baseline > 6.5 Hz	24 um	20 um	13 um
(Height error) (Cross-track slope error)	(0.43 cm) (0.11 urad)	(0.36 cm) (0.095 urad)	(0.23 cm) (0.06 urad)
Total Allocation (RSS)	**1.1 cm** **0.29 μrad**	**0.89 cm** **(0.24 μrad)**	**0.65 cm** **(0.17 μrad)**
Unallocated Margin (RSS/SUM)	0.36 / 0.05 cm (0.4 / 0.21 urad)	0.23 / 0.025 cm (0.25 urad / 0.11 urad)	0.23 / 0.025 cm (0.3 urad / 0.18 urad)
Total (RSS) RMS Error	**1.15 cm** **0.5 μrad**	**0.92 cm** **0.35 μrad**	**0.69 cm** **0.35 μrad**

6.4.1 Radial Knowledge Error Requirements

As previously discussed in the ocean error budget section, a radial knowledge error will directly translate into a height error, since the topographic measurement assumes perfect knowledge of the orbit's altitude and the reference point of each instrument. The knowledge error of the true radial height above a reference surface has several contributors:

1) Errors in the orbit determination of the satellite

The fundamental vector provided by POD is from the Center of Mass (CoM) of the Earth system to the CoM of the satellite[3]. The required error figure of 1.5 cm RMS (a 24h RMS number) to

---

[3] Hereafter, we will use CoG and CoM for the Flight System and its elements interchangeably. While,

cover the ocean wavelengths greater than 1,000 km with the nadir altimeter corresponds to the uncertainty in the radial component of this ~7,400 km long vector. Several phenomena contribute to this error, including modeling errors of atmospheric drag, solar radiation pressure and gravitational effects.

To estimate the position of the satellite center of mass on-orbit as accurately as possible, several instrument measurements are used. In order to meet the 1.5 cm radial accuracy required for the operational orbit, SWOT, like the Jason series of altimeter satellites, is equipped with state-of-the-art DORIS, LRA and GPSP tracking systems. The orbit determination noise is expected to be essentially uncorrelated, as by definition represents the non-systematic contribution to the error budget. Random errors can thus be quantified to some extent by comparing the reduced-dynamic orbit solutions obtained by different groups and methodologies, whereas specific detailed analyses are required in order to characterize the systematic errors. Depending on the frequency and amplitude of the error, the impact on the different orbit solutions can be estimated and, as a result, drifts can be assessed. The most critical errors come from any unknown variations at timescales of the orbital period since, in that case, they cannot be distinguished from noise, thereby degrading the error budget.

Regarding POD validation, it is important to mention that the accuracy of the orbit determination is typically assessed by using several metrics, involving the comparison between the different orbit solutions and the analysis of the residuals of high elevation SLR measurements. These datasets are provided by different teams using different software tools, and employing similar although not identical techniques.

An a priori knowledge of the distance between the phase center of each instrument and the satellite center of mass in the 3 axes is needed to get all the measurements in the same reference frame. However, the final performance is impacted differently depending on what instrument and what axis is considered. For example, a lack of knowledge in the nadir direction on the LRA optical center position would have a direct impact of the restituted orbit using this instrument. Many mission-dependent parameters have also to be known to provide the models with the highest accuracy possible of the forces involved, e.g. the satellite's size and geometry, its surface emissivity properties, solar arrays rotation angle, attitude, etc.

2) Absolute knowledge accuracy of the vectors between the phase center of the POD instruments and the satellite CoG

It is important to note that the POD error already accounts for an absolute knowledge error of the vectors between the phase center of the POD instruments and the satellite CoG. The same requirement already levied on the POD is therefore compatible with the errors associated to retrieving the height of the satellite CoG above the reference ellipsoid for hydrology.

As described below, the knowledge error can be flown down to different contributors for different frequency ranges. Drifts in the CoG of the satellite are obviously an important factor. From a POD perspective, the satellite's CoG is moving smoothly around the Earth's center, and

---

strictly speaking, the CoM is the point at which the distribution of mass is equal in all directions (which does not depend on the gravitational field) and the CoG is the point at which the distribution of weight is equal in all directions (which does depend on the gravitational field), for our purposes and in the case of a satellite orbiting the Earth the difference is negligible.

any changes (due to vibrations, thermoelastic effects including solar panel snaps, or fuel consumption, for example) will introduce a separate radial height error.

The knowledge of the vector between the antennas phase center and the satellite CoM is one of the drivers of the final accuracy and of the POD stability, through its dynamic component. Each instrument contributing to the generation of the Precise Orbit Ephemeris (POE) provides a measurement with respect to its own reference point. For DORIS and GPSP, measurements are related to their respective antenna phase center. For the LRA, the measurement is referenced to its optical center. These instrument references have then to be referenced to the satellite CoM. To integrate these elementary measurements, the vector between all the phase/optical centers and the CoM has to be known with the best accuracy possible. Note that the knowledge error of the optical center of the LRA is more stringent as it is used to validate DORIS + GPSP performance; therefore, the better the knowledge error achieved, the better the accuracy of the resulting POD validation and calibration.

The knowledge error of each antenna measurement reference to the satellite CoM vector has several contributors. Some are truly static, that is, an error that will remain constant during the on-orbit life, and some are dynamic. The latter includes errors that vary during the on-orbit lifetime, which can exhibit different frequencies. It is important to establish the main different frequencies of these error signals, as they can be handled differently by the POD team in determining the orbit.

Compared to other missions such as the Jason series of altimeters, SWOT is a large satellite with large appendices, making the accuracy of the CoM measurement significantly more challenging, and with a larger range of expected thermoelastic distortions for several flight system elements. As a result, and compared to other missions, the combination of all the possible dynamical error sources based on existing capability for SWOT exceeds heritage levels. This has triggered the need to perform specific detailed analysis to understand and characterize the different effects depending on their frequencies, in particular over the duration of an orbit.

Three types of frequencies can be defined:

- Static, or initial knowledge errors: these are the initial errors expected at the beginning of the on-orbit operations, including all the uncertainties accumulated before that state (i.e., measurement uncertainties, modelling errors, ground deployment of KaRIn antennas in a 1-g environment, etc.). For the most part, these error components are adjusted over the first months of the mission using the following metrics: high elevations SLR residuals, SSH residuals at crossover points, intercomparison of different orbit solutions, and orbit overlap. The vector from the satellite CoM to the DORIS or the GPS phase center can actually be estimated as part of the POD process as a "nuisance parameter", allowing the identification of potential errors on these vectors (e.g. GPS antenna phase variations due to, for example, multipath effects). This step will be conducted during the early stages of the SWOT Cal/Val phase, as it was done for the Jason series of altimeters, allowing to adjust for the static components of the knowledge error.
- Orbital variations: these refer to all of the unknown variations at timescales of an orbit (typically thermoelastic effects).
- Long term variations: these refer to all of the unknown variations occurring with a period longer than an orbit, and likely more prominent in the timescales of days to tens of days,

such as thermoelastic errors induced by the "seasonal" variations of the beta angle, maneuvers (causing propellant consumption), etc. Some of these errors are predictable, such as the satellite's CoM position change due to propellant consumption.

In order to meet the required level of performance, POD needs the knowledge accuracy on the relevant vectors summarized in the table below, which has been flown down through the flight system requirements.

Table 12. POD vectors uncertainties – End-to-end requirements in mm.

	X-axis			**Y-axis**			**Z-axis**		
Vector	Static	Orbital variations	Long term variations	Static	Orbital variations	Long term variations	Static	Orbital variations	Long term variations
DORIS -CoM	± 10	± 5	± 5	± 10	± 5	± 5.3	± 12	± 5	± 5.8
LRA-CoM	± 10	± 5	± 5	± 10	± 5	± 5.3	± 8	± 3	±5.8
GPSP-CoM	± 12.1	± 5	± 5	± 12.1	± 5	± 5	± 12.1	± 5	± 5

The figure below provides an example of the flow-down for DORIS-CoM vector knowledge.

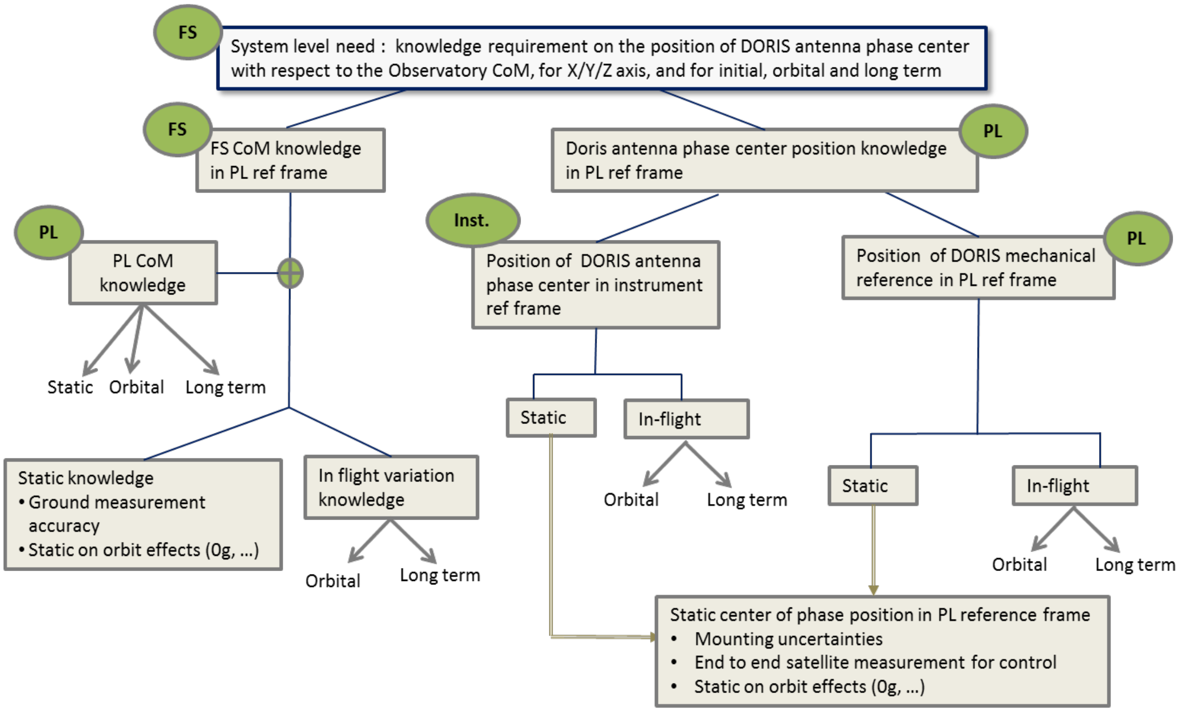

Figure 72. Conceptual flow-down of the DORIS-CoM vector knowledge

As shown in the above figure, the knowledge requirements on these vectors are flown down to the Flight System for CoM initial knowledge (the best pre-flight knowledge of the static errors) and variations (including static biases, orbital and long-term variations), to the instruments for the phase center position knowledge in the instrument reference frame, and to the overall Payload for the instrument reference frame knowledge in the PL reference frame, which is actually the one used to reference all the measurements.

It is important to note that the GPSP configuration is different from that of DORIS and LRA, as it is actually accommodated on the Spacecraft side, and not on the payload (the Payload instruments require a nadir view, whereas GPS requires a zenith view to the GPS constellation). As a consequence, the associated error contribution comes for the Spacecraft rather than from the Payload.

The break-down of the overall vector knowledge requirement between phase centers and the F/S CoG is shown in the tables below for DORIS, GPSP and LRA. These correspond to subsystem (instrument, PL, SC) allocations.

Table 13. breakdown of the overall vector knowledge requirement between center of phase and CoG

	STATIC - mm			ORBITAL - mm			LONG TERM - mm		
	X	Y	Z	X	Y	Z	X	Y	Z
DORIS phase center knowledge	± 1.00	± 1.50	± 5.25	± 1.00	± 1.00	± 1.00	± 1.00	± 1.30	± 1.80
LRA optical center knowledge	± 1.41	± 1.80	± 1.80	± 0.50	± 0.50	± 0.50	± 1.00	± 1.30	± 1.80
GPSP phase center knowledge	± 6.10	± 6.10	± 6.10	± 1.70	± 1.70	± 1.70	± 0.15	± 0.15	± 0.15
F/S CoG knowledge	± 6.00	± 6.00	± 6.00	± 1.50	± 1.50	± 1.50	± 4.00	± 4.00	± 4.00

The contribution of CoG variations on orbital and long term variations arises from independent effects (e.g., thermoelastic and propellant consumption), thereby allowing to consider the final orbit radial error at instrument measurement level as an RSS of both components. The total CoG variations is then lower than 4.3 mm, with a corresponding allocation of 5 mm, as shown in Table 14.

3) Drifts in the radial height of KaRIn's interferometric baseline

Deformations of KaRIn's mechanical boom, due to on-orbit thermoelastic effects or dynamic disturbances will shift the radial position of the interferometer's baseline over time (relative to the nominal one) resulting in a height error. While there is some commonality with shifts in the

CoG (i.e., a thermoelastic deformation of the interferometric baseline can also induce a CoG shift), the radial displacement of the baseline will directly introduce a height error that is independent of how the deformation impacts the mass distribution of the satellite. Therefore, a requirement is levied on the stability of the radial center of KaRIn's interferometric baseline of 1 mm.

The POD errors are expected to be independent of thermoelastic effects that will cause drifts in the satellite's CoG and deformations of the radial component of the KaRIn interferometric baseline. Therefore, the latter two are added as a direct sum, which is then RSS'ed to the POD performance requirement. The allocation break-down is captured in the table below.

Table 14. Break-down of the radial height error

Radial Error Component	Height Error [cm]
POD	1.5
Flight System CoG knowledge error	0.5
KaRIn baseline radial stability error	0.1
Total Radial Error	**1.62**

The POD slope errors also need to be specified in order to meet the overall slope error requirement; an allocation of 0.5 μrad is therefore levied on the Flight System and the POD performance. The allocation break-down for slopes is captured in the table below (the same approach of direct sum and RSS as for height is used for slopes as well). Note that the conversion from μrad to perhaps friendlier units of cm/s can be obtained by considering that the ground speed is 6.5 km/s. Therefore 0.5 μrad (or 0.05 cm/km) would translate into 6.5 km/s*0.05 cm/km = 0.3250 cm/s.

Table 15. Break-down of the radial slope error

Radial Error Component	Slope Error [μrad]
POD	0.4
Flight System CoG slope knowledge error	0.2
KaRIn baseline radial slope stability error	0.1
Total Radial Error	**0.5**

6.5 Land Media Error Requirements

6.5.1 Wet troposphere

The typical variability of the wet troposphere signal over land can be characterized from the quality controlled Integrated Global Radiosonde Archives (IGRA). An analysis of 981 globally distributed stations, using path delay profiles from 1980 to 2010, has been used to derive representative estimates of the mean values of the signal, as well as of the variability that can be expected between different passes. These are shown in the two figures below.

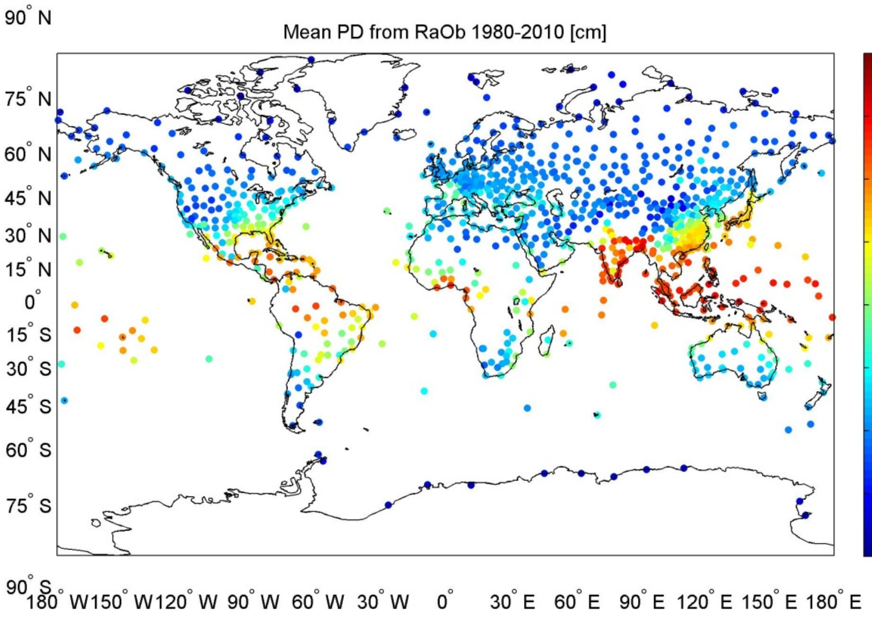

Figure 73. Mean path delay in cm, for each station.

As one would expect, the variability scales with the magnitude of the path delay signal, with lower variability in winter in mid-to-high latitudes, and higher variability in low latitudes and in the summer months in mid latitudes. The total variability of the path delay, shown in the figure above, reaches a maximum of 12 cm. This is in fact dominated by the annual signal, and decreases to less than 7 cm maximum after removing it.

However, a model can be used to remove a significant fraction of the path delay signal. For example, the NCEP reanalysis product, available every 6 hours at a 2.5 deg resolution can be used to this end (other models such as MERRA and ECMWF are also available). An analysis performed by comparing the NCEP model estimates to actual measurements acquired by the US Department of Energy's atmospheric radiation measurement facilities, most of which include an upward looking microwave radiometer providing 1-min measurements of the wet tropo path delay, shows that the difference is always smaller than 4 cm at all stations, ranging from 1.1 cm to 3.8 cm; the measurement error of the radiometers is estimated to be approximately 0.5 cm, so most of the residual error points to the model.

Based on this, the allocation to the wet tropo height error over land is 4 cm, and will require the Algorithm System to implement the ingestion of model estimates to correct the wet tropo variability. The allocation of the wet tropo slope error over land is 1.5 urad.

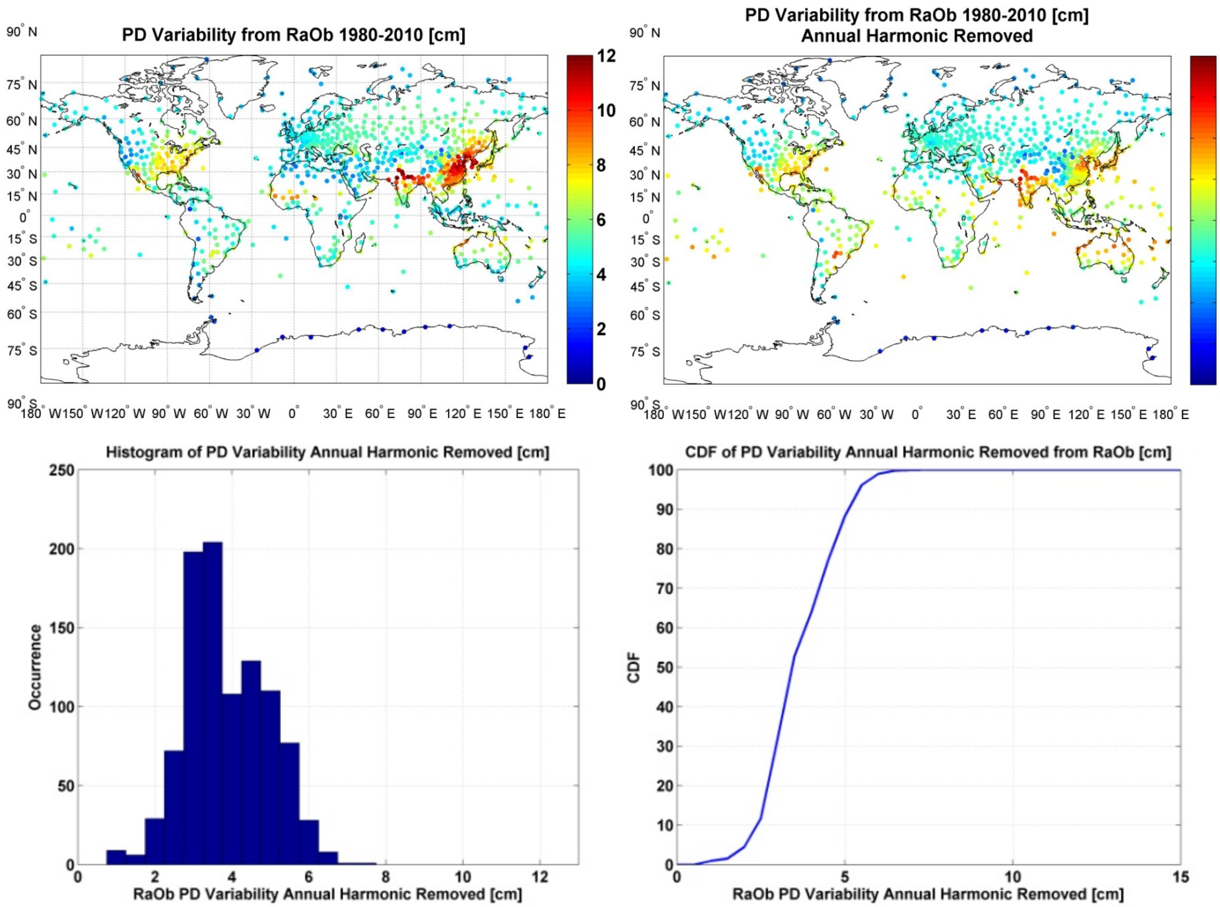

Figure 74. (top left) total variability at each station derived from the path-delay standard deviation from 1980 to 2010; (top right) variability after removing the annual harmonic; (bottom left) histogram and (bottom right) CDF of the path-delay variability after removing the annual harmonic.

6.6 Dry troposphere and Ionosphere

The dry troposphere and ionosphere signals for hydrology are extracted from models. We have used the ECMWF pressure model for the dry troposphere and the Ionex model [20] for the ionosphere. Based on global simulations of these models, we extract the following spectral envelopes after removing the annual mean:

$$E_{dry\ tropo}(f) = 2 \cdot 10^{-7} f^{-3} \quad [cm]$$

$$E_{ionosphere}(f) = \begin{cases} 1.1 \cdot 10^{-13} f^{-4.593}, & f \leq 3.2 \cdot 10^{-3} \\ 3.15 \cdot 10^{-2}, & f > 3.2 \cdot 10^{-3} \end{cases}$$

These spectra are shown in the figure below:

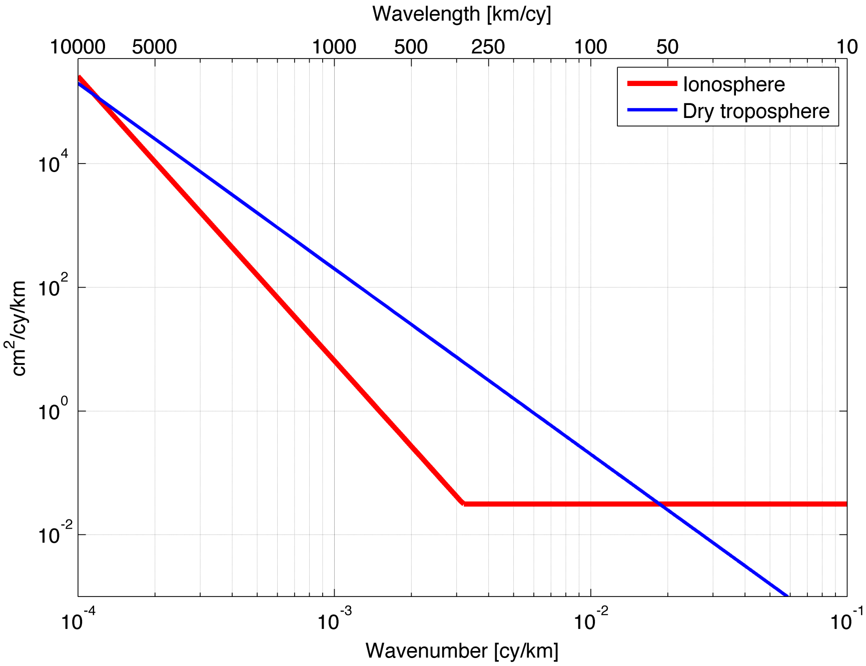

Figure 75. Spectral envelopes for the ionosphere and dry troposphere signals over land.

For the dry troposphere, the overall RMS error integrated over 2,000 km is 0.64 cm, and it is 3.75 cm over 10,000 km. For the ionosphere, the overall RMS error integrated over 2,000 km is 0.2 cm, and it is 3.77 cm over 10,000 km.

The current allocations of 0.8 cm for ionosphere and 0.7 cm for dry troposphere errors require using global models to reduce these errors of the full signal over land, to at least eliminate the global daily mean. The dry troposphere is to be corrected with weather models, like it is done operationally for the Jason series of altimeters, and the ionosphere will use ionospheric models such as Ionex or GPS Global Ionosphere Map (GIM) products.

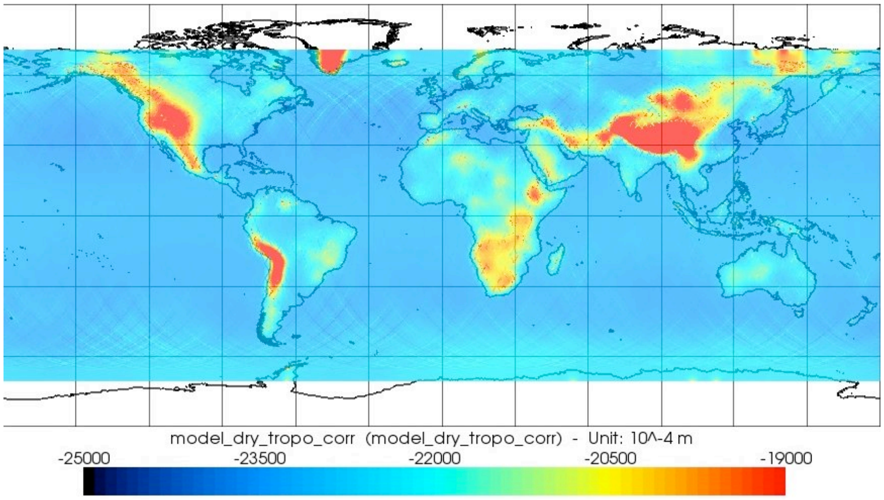

Figure 76. Example of the amplitude in meters of the dry troposphere correction computed from the ECMWF atmospheric pressures and model, as used to correct Jason-1.

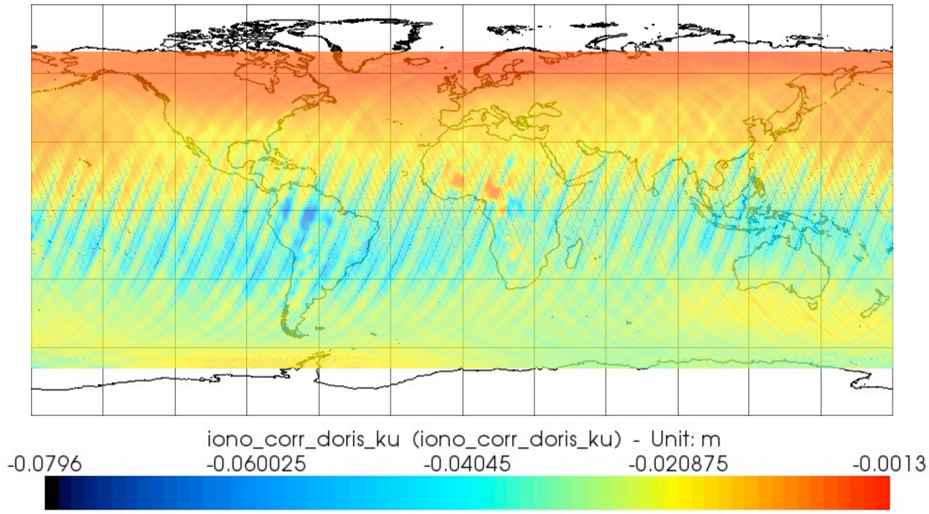

Figure 77. Example of the amplitude in meters of the ionospheric correction derived from DORIS measurements, as used to correct Jason-1.

The slopes that these media errors introduce, computed integrating the corresponding slope spectra, are small, at less than 0.1 urad for both signals.

6.7 Motion errors

In the ocean section, we described how the motion of a target on the ground creates interferometric height errors, and described two components to this error, the first one related to surface ("bulk") motions of the ocean, and the second one related to the radial velocity of ocean waves. For surface water bodies, we consider that rivers and small lakes do not generally develop waves as the ocean does. Therefore, we will hereafter consider that the only motion mechanism is that of a surface water body, as a cross-track velocity, and that we can ignore the effect of vertical velocities and wave bunching associated to waves. However, it is important to note that there are some notable exceptions to this proviso, such as very large lakes and reservoirs, which for most purposes behave like the ocean and will be processed as ocean data.

Based on observations reported in the available literature (see e.g. [11-12]), the surface velocity for most water bodies can be conservatively estimated to be <2.6 m/s in a 1-sigma sense. Following the derivation presented in the ocean motion errors, we allocated for this error the swath-average 1-sigma error in the event of a pitch control error of 33 mdeg and for a surface velocity of 2.6 m/s, which is 0.8 cm.

Note that slope errors will also appear in the presence of surface velocity variations, due to the following mechanisms: 1) variability of the surface velocity itself over the reach. For example, a change in the surface velocity, even under a fixed observational geometry, will introduce a height-varying error along the reach, resulting in a slope error; and 2) a change in the observational geometry over the reach. For example, a bend or a turn of a river relative to the velocity vector will change the apparent line-of-sight velocity and result in a height-varying error along the reach, causing a slope error. Based on the 1-sigma bound of the surface velocity, the worst case 1-sigma slope error would be introduced when the velocity changes from a 2.6 m/s to -2.6 m/s over a 10 km reach. In this case, a height variation of 0.8 cm to -0.8 cm over a 10 km reach would result in a slope error of 1.6 urad. While this is likely a very pessimistic case, it does bound the maximum slope error.

6.8 Classification accuracy

The primary way in which water can be distinguished from land is due to the greater brightness of water relative to land. It is important to note, however, that the classification (as well as height and slope) accuracy requirements apply over non-vegetated surface areas due to the complex way in which vegetation can affect the retrieval of elevations and inundation extent. In its simplest and crudest form, the classification could take a number of looks by spatial averaging the full-resolution pixels to reduce the classification error, and then define classification thresholds based on land return statistics, followed by a simple 2-class Bayesian classification based on a single threshold for a local area. When considering a classification that is based on a single-pixel basis, it can be shown that the Bayesian classifier is in fact optimal. A post-classification algorithm would then remove outliers and consolidate water bodies.

The classification scheme can be conceptualized as finding the power threshold, P_t, where the two distributions of the powers associated to water, f_{water}, and land, f_{land}, meet, i.e., $f_{water}=f_{land}$. For a small number of looks, the land or water pixel statistics, being dominated by speckle, are not Gaussian; instead, they can be modeled as follows:

$$f_{water}(N, P_w, P_n) = \frac{1}{(N-1)!}\frac{N^N}{P_w+P_n}\left(\frac{p_t}{P_w+P_n}\right)^{N-1} e^{-\frac{Np_t}{P_w+P_n}}$$

and

$$f_{land}(N, P_l, P_n) = \frac{1}{(N-1)!}\frac{N^N}{P_L+P_n}\left(\frac{p_t}{P_L+P_n}\right)^{N-1} e^{-\frac{Np_t}{P_L+P_n}}$$

where N is the number of looks, P_w and P_l are the expected value of the water and land power levels, respectively, and P_n is the noise level.

When the noise power level is close to the land power level, i.e., $P_l+P_n \sim P_n$, as it is the case for SWOT since the return from land is expected to be below the noise level, a closed-form approximate solution can be found for the power threshold for an arbitrary number of looks (otherwise the solution depends on N), which is given by:

$$p_t = \frac{P_n}{P_w}(P_w+P_n)\log\left(\frac{P_w+P_n}{P_n}\right)$$

The misclassification probability can then be derived by integrating the respective tails of each distribution above/below the threshold value. In this case, a numerical simulation without making the above approximations has been used to find the threshold and derive the misclassification probabilities. The figure below present below swath-averaged results for different number of looks a fixed land sigma0 of 0 dB, as a function of surface water sigma0 (note that since the land is fixed at 0 dB, the surface water sigma0 in the figures also represents surface water to land contrast in dB). In this simplified analytical analysis, the cross-track resolution varies from 10 m to 70 m (consistent with the KaRIn instrument resolution across the swath), and N x 6.6 m (i.e., N x single-look resolution x presum factor, where here we consider the worst-case presum factor of 2.5 discussed earlier). It is also worth noting that: 1) the classification probabilities are not symmetric, with water being more likely (mis)classified as land; and 2) this is a biased classification method, particularly for water bodies with areas close or comparable to the averaged resolution. This is because, due to the contrast, it is likely to classify a pixel that contains a significant portion of land, as water. More sophisticated classification methods imposing spatial regularization can be envisioned which, together with using the coherence estimates in addition to the power images, can improve the classification performance and reduce or eliminate classification biases.

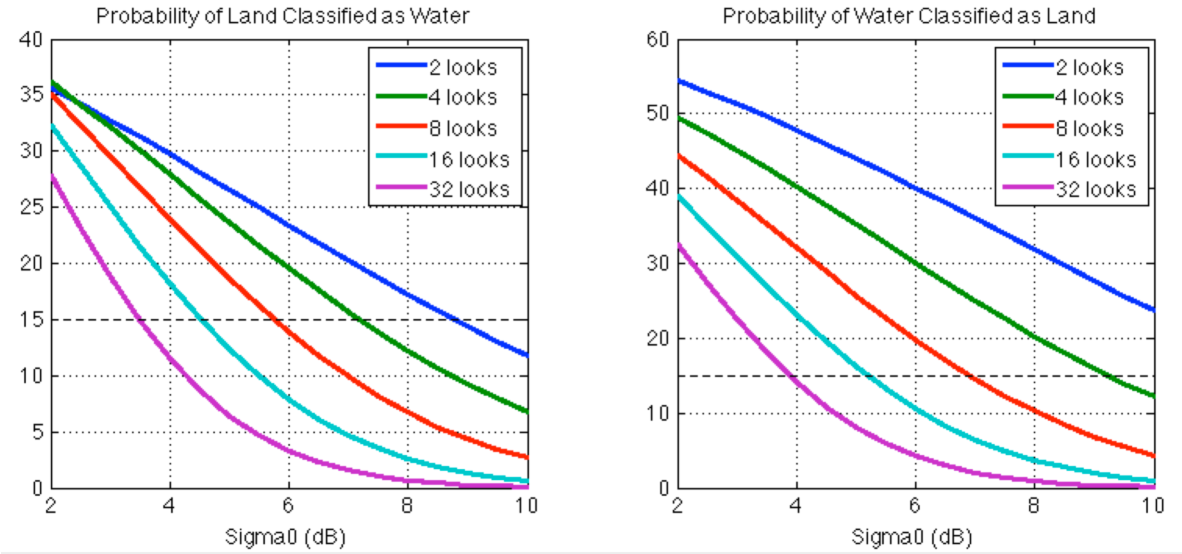

Figure 78. Swath-averaged classification errors for land and water as a function of the sigma0 of the water, and for *N*=2, 4, 8, 16 and 32. The dotted line represents the current requirement of 15% misclassification. In all cases, a land sigma0 of 0 dB has been used.

As it can be seen from the above figure, this requirement primarily drives KaRIn's SNR, together with an assumption of the minimum number of looks that can be used (as it relates to the minimum surface water body area).

In addition, the current assumptions for the classification performance include sufficient land-to-water contrast, as well as an absolute brightness of the water, as shown in the figure above, in order to meet the classification requirement. Available observations from GPM and airborne scatterometers (see figures below) indicate that, statistically speaking, land to water contrast (when water is not specular[4]) is generally above 10 dB for most common land types, with croplands and urban areas being the brightest non-water land types. These results indicate that the contrast is adequate to support meeting the classification requirements.

---

[4] Specular situations are characterized by a very large return at nadir and a very fast roll-off with increasing incidence angle. In this situations, the 10 dB condition over the swath would likely not be met, resulting in a reduced swath. Evidence of these specular water surfaces has been shown by airborne scatterometer measurements over very small lakes under no-wind conditions and some rivers sections (likely portions that are shadowed from the wind), as well as from GPM measurements over large lakes under very low wind conditions.

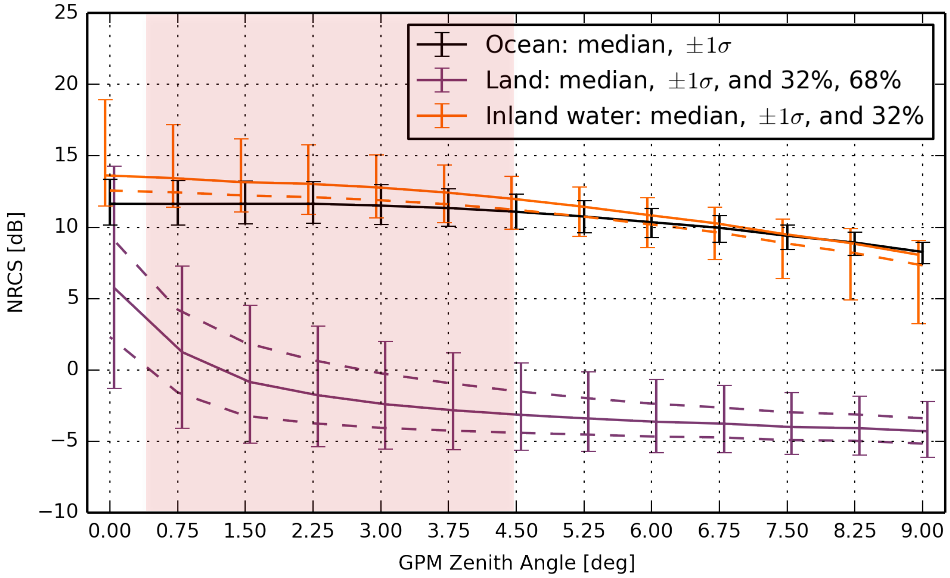

Figure 79. Calibrated GPM Ka-band sigma0 for all (non-water) land surfaces. The ocean and inland water brightness are also shown for reference. The region highlighted in red corresponds to the SWOT range of incidence angles. The contrast for surface water to land is in the range of 12 to 15 dB beyond 1 deg incidence; below 1 deg the mean contrast is reduced to ~7 dB.

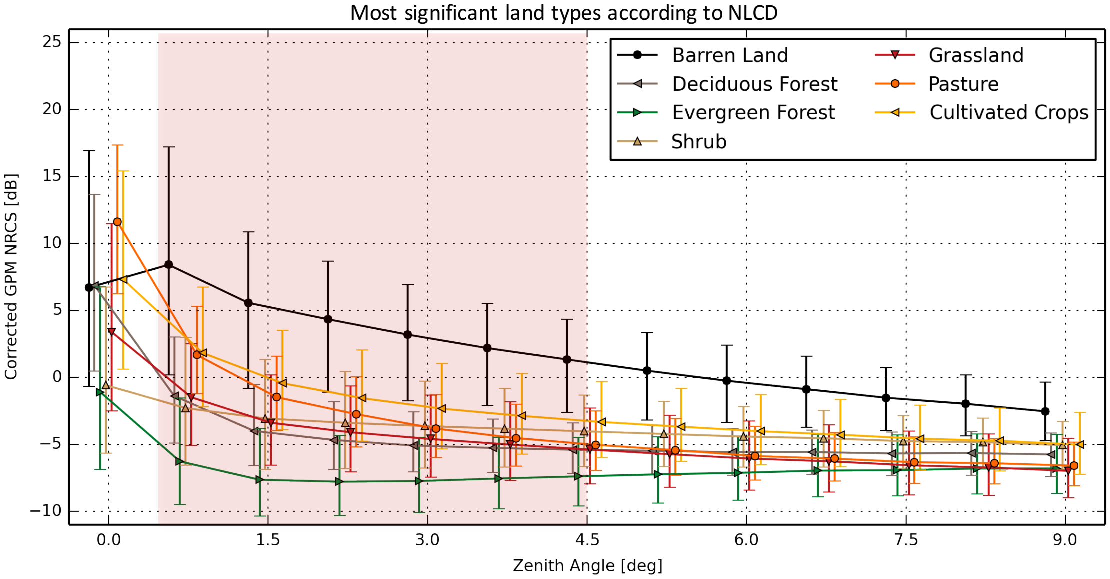

Figure 80. GPM calibrated sigma0's binned by land type (over all seasons). Classification for land types uses the US National Land Cover Database (NLCD), and therefore it is limited to GPM measurements in the US. The GPM measurements are also filtered for high uniformity and no/low water content within the footprint.

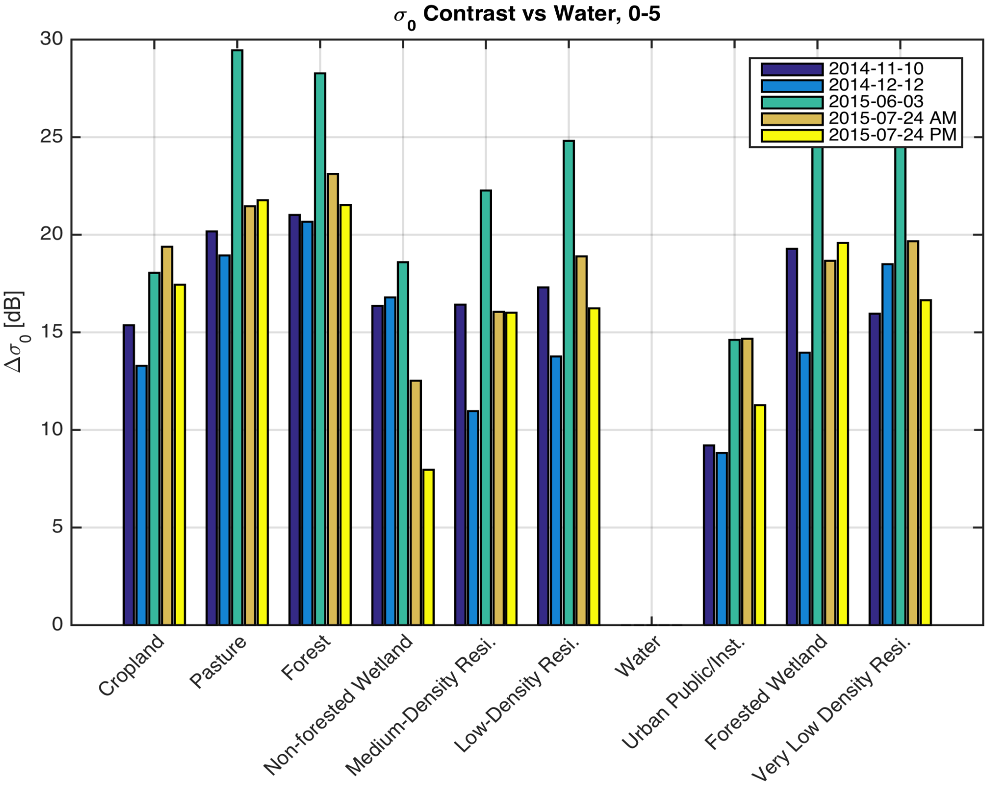

Figure 81. Water to land contrast from measurements collected with the airborne Ka-band scatterometer from the University of Massachusetts. These measurements were collected over the Massachusetts state area, and are separated by land type using the MassGIS Land Use database. With a resolution of 5-15 m depending on the flight altitude, these measurements characterize the contrast of water to other surface types at much higher resolution than GPM.

An additional geophysical parameter of interest towards water classification is the decorrelation time of the water, since the resolution of the aperture synthesis is limited by the coherence time. In practice, if the decorrelation time of the scene being observed is not sufficiently long so that the return stays coherent over the aperture time required to synthesize a certain resolution, a de-focusing or smearing will occur in the azimuth direction (there is no impact to the cross-track resolution). The decorrelation time is most important towards meeting the 15% classification requirement for $(250\ \text{m})^2$ lakes and 100 m rivers since, in order to achieve better than 50 m resolution in the magnitude azimuth point target response of the radar (or, equivalently, 36m in the 3 dB power width), the water needs to be coherent for at least ~9 msec. In order to assess this geophysical parameter, a series of observations were obtained early on with a Ka-band radar deployed to various rivers and reservoirs [14], which have been complemented with observations from the AirSWOT instrument. The early measurements suggested coherence times ranging between 5 and 50 ms (see figure below), with the AirSWOT observations lying in the middle of this range and supporting 3 dB power widths generally between 5 and 25 m (with about 90% of the observations exhibiting power widths narrower than the limit of 36 m).

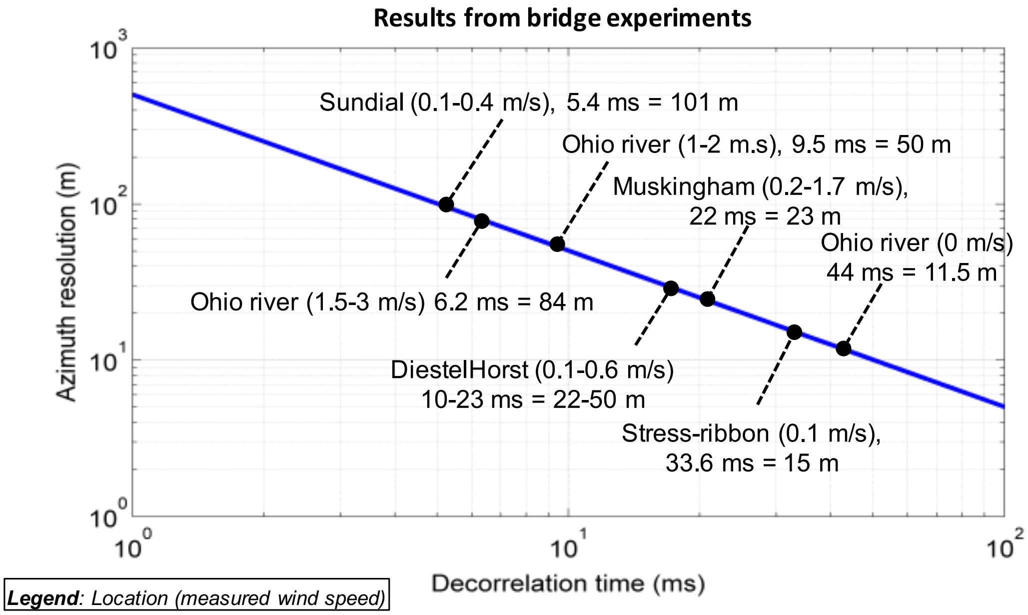

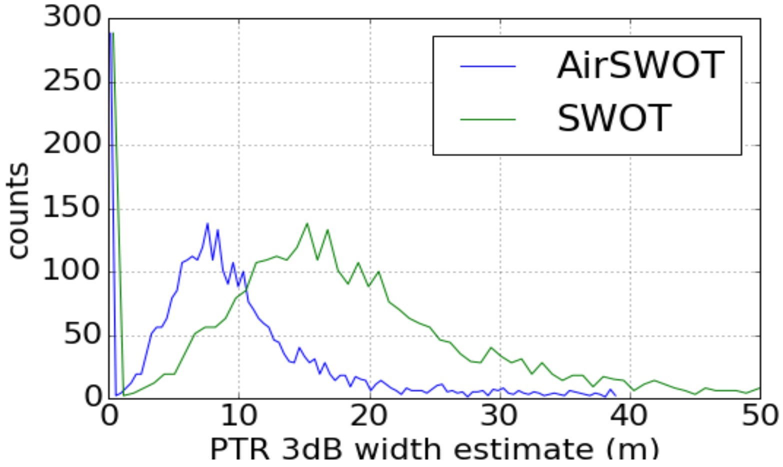

Figure 82. (top) Effective along-track resolution as a function of decorrelation time for SWOT. Each point represents an observation obtained with a Ka-band radar over rivers and reservoirs in Ohio and Redding, CA (see [14]). (bottom) Histogram of power width estimates from AirSWOT observations over the Yukon Flats (AK) area, which includes many small lakes and a braided river. The blue line represents the direct AirSWOT observations, and the green line its conversion to SWOT's geometry.

Initial performance results of Bayesian classification algorithms using synthetic scenes of 250 m^2 lakes and 100 m wide rivers for nominal sigma0 conditions are shown in the figure below as a swath-average against the 15% requirement. It is worth noting that, as expected, the performance mostly depends on the water sigma0 (or, in fact, the water to land contrast, as the land sigma0 is here fixed at 0 dB) as well as the coherence time. The 15% requirement is clearly met for coherence times resulting in azimuth magnitude widths of 50 m (power widths of 36m) and lower, and for water sigma0's higher than 7 dB.

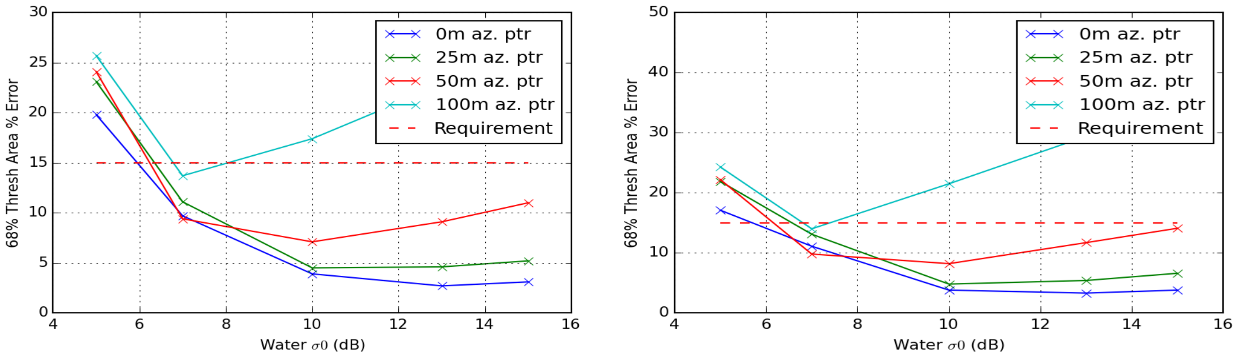

Figure 83. Classification performance for (left) lakes of 250 m^2 area, and (right) rivers of 100 m width. The different curves represent different azimuth (magnitude) point target response widths, and the area error is shown as a function of water sigma0. The requirement of 15% is also shown as a red dashes line. Note that 68% threshold means that 68 % of the data has absolute area % error less than this threshold.

7 Flagging Requirements

There are requirements to flag rain for both ocean and surface water, sea ice for ocean, as well as topographic layover and frozen water affecting surface water bodies, all with an accuracy of 68%. The basic concept to generate the flags is to use a detection algorithm based on return power (SNR loss) and coherence loss (except for ice, which cannot be resolved, and external models are required). The initial assessment is that these requirements do not drive the mission performance requirements beyond what has been already discussed.

A simulation specifically to show the feasibility of meeting the rain flagging accuracy was performed using ocean simulation data that interpolated AMSR-E data to the SWOT swath (at 2 km pixels). To perform the evaluation, the AMSR flag was used as a proxy with a 100 km buffer around land (see map of valid data). The probabilities were computed from whether the radiometer pixel - either nadir or center of each swath - detected rain and what was found in the other swath pixels.

The simulation results for the cross-track radiometer are shown in the figures below over different ocean regions and across the swath, covering -60 to + 60 km.

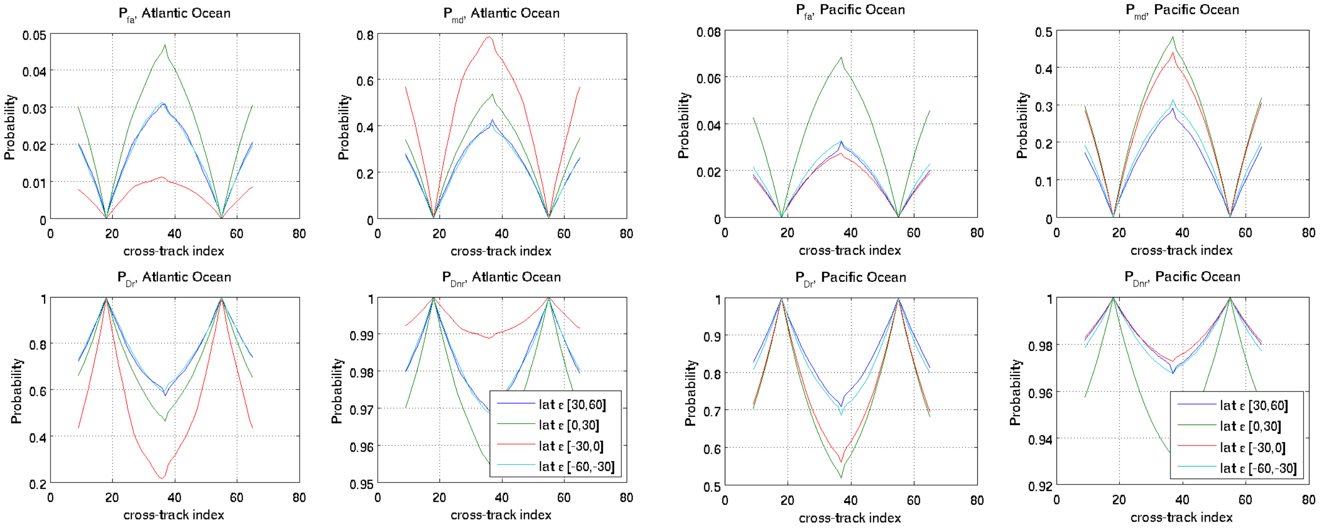

Figure 84. Simulation results for the Atlantic Ocean (left four plots) and Pacific Ocean (right four plots). For each on of these two cases, the four plots show: (1) the probability of false alarm (P_{fa}), upper left; (2) the probability of missed detection (P_{md}), upper right; (3) the probability of detected rain (P_{Dr}), bottom left; and (4) the probability of detected no rain (P_{Dnr}), bottom right.

The table below summarizes the results for each ocean region, which meets or exceeds the required 68% to detect rain in all cases.

Table 16. Summary of classification probability results

Atlantic	**Latitude Band: [-60, 60] deg**
Probability of	
False Alarm	0.015
Missed Detect	0.281
Detect Rain	**0.719**
Detect No Rain	0.985
Pacific Ocean	**Latitude Band: [-60, 60] deg**

Probability of	
False Alarm	0.020
Missed Detect	0.192
Detect Rain	**0.808**
Detect No Rain	0.980
Indian Ocean	**Latitude Band: [-60, 0] deg**
Probability of	
False Alarm	0.017
Missed Detect	0.198
Detect Rain	**0.802**
Detect No Rain	0.983

8 Pointing Error Budget

This section presents the pointing error budget. Hereafter, we will use a spherical coordinate system to define the elevation and azimuth angles, as illustrated in the figure below. Typical SCH coordinates (represented by $(\hat{s}, \hat{c}, \hat{h})$ in the figure, which constitute a local coordinate system defined about the instantaneous sub-satellite point on the Earth's surface, where both s and c follow great-circle paths over the surface) is used to represent the projection of the look vector on the ground. The look vector from a given antenna, in the standard azimuth over elevation convention, is defined by:

$$\hat{l} = \begin{bmatrix} \sin\phi\cos\theta \\ \cos\phi\cos\theta \\ \sin\theta \end{bmatrix},$$

where θ is the elevation angle, and ϕ is the azimuth angle[5]. The elevation angles are positive for positive c ($-\hat{y}$ direction). The projection of the vector $\hat{l}$ in SCH coordinates is thus given by:

$$\hat{l}_{SCH} = F \cdot R_3(-\theta_y) \cdot R_2(-\theta_p) \cdot R_1(-\theta_r) \cdot F \cdot R_1(\Gamma) \cdot \hat{l}$$

where R_i is the Euler rotation matrix about the i^{th} axis, Γ=90 deg, $\theta_r, \theta_p, \theta_y$ are the rigid body S/C roll, pitch, and yaw, respectively, and and $F = \begin{bmatrix} 1 & 0 & 0 \\ 0 & -1 & 0 \\ 0 & 0 & -1 \end{bmatrix}$.

The pointing error budget is in fact derived primarily from the random and systematic error budget, and are broken up into:

- *Absolute pointing control requirements*: mainly driven by the random error performance. Absolute pointing requirements apply to the 3 axis.
- *Relative pointing knowledge requirements*: mainly driven by the systematic error performance, as previously discussed. Roll drift is the driving knowledge requirement.
- *Absolute pointing knowledge requirements*: mainly driven by the systematic error performance, which apply to the 3 axis.

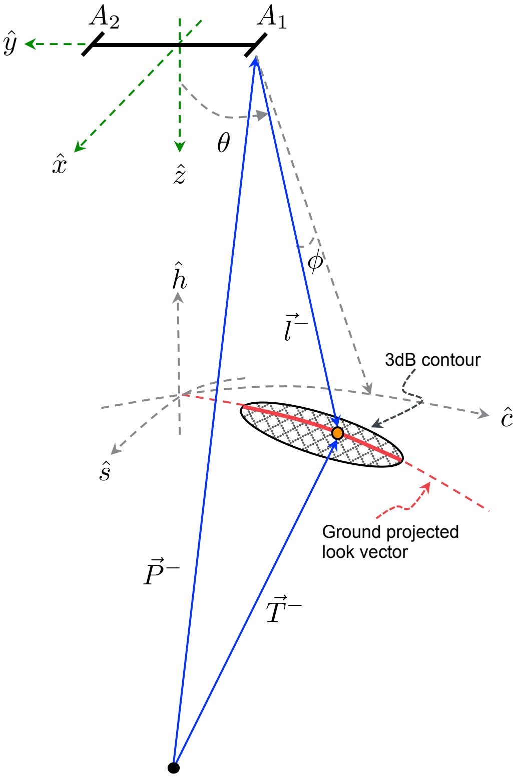

Figure 85. Coordinate system illustrating the phase center of the two KaRIn antennas, $\boldsymbol{A_1}$ and $\boldsymbol{A_2}$, with the baseline oriented along the $\hat{\boldsymbol{y}}$ axis (cross-track direction). The look vector shown, $\hat{\boldsymbol{l}}^-$ (where the minus represents that $\boldsymbol{A_1}$ is at a negative location along $\hat{\boldsymbol{y}}$), points with an elevation angle $\boldsymbol{\theta}$ and azimuth angle $\boldsymbol{\phi}$. The 3dB contour of the antenna pattern projected on the ground is also shown, as is the SCH coordinate system, and the vectors from antenna $\boldsymbol{A_1}$ to the Earth's center, $\vec{\boldsymbol{P}}^-$, and from that antenna to the intersection of the look vector with the surface, $\vec{\boldsymbol{T}}^-$.

There is also a requirement to yaw-steer the S/C to zero Doppler along the orbit. To first order, this is a very slowly varying sinusoidal steering angle of ~+/-4 deg with a period of one orbit. Note that a Total Zero Doppler steering [21] is not implemented, as the pitch direction is not steered by the S/C, only the yaw axis. This results in a

---

[5] Note the azimuth angle defined here is different from the *ground* azimuth angle, previously defined during the discussion of the ocean motion effects.

much smaller, but non-zero residual Doppler variation both across the swath and along the orbit.

We start the discussion of the pointing error budget with a description of the angular biases that are introduced due to pointing errors, followed by the derivation of the pointing allocations.

8.1 Systematic Angular Biases

In the random error section, we discussed the effect of the angular decorrelation in terms of introducing a small loss of coherence. However, the argument of the angular correlation includes the effect of the topography, and will also introduce a systematic phase bias.

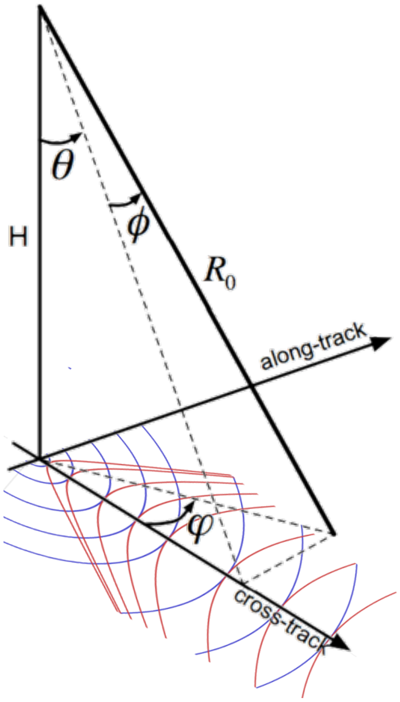

Figure 86. Illustration of the geometry, defining three angles: the look angle, θ, the ground azimuth angle, φ, and the azimuth look angle, ϕ. Also shown are the iso-range lines (blue) and iso-phase lines (red).

Starting from the definition of the angular decorrelation term:

$$\gamma_{\varphi}^{(J)} = \frac{\oint_{r=R_0} G_1(\vec{r})G_2^*(\vec{r})\sigma_0(\vec{r})\chi_{az}^{(J)}(\vec{r})e^{-j\Phi}ds}{\oint_{r=R_0} G_1(\vec{r})G_2^*(\vec{r})\sigma_0(\vec{r})\chi_{az}^{(J)}(\vec{r})ds}$$

Using the geometric definitions shown in Figure 86, and assuming for the time being that there is no surface topography, the phase term Φ can be approximated by:

$$\Phi = k(r_1 - r_2) \approx -kBsin(\theta)(1-\cos(\varphi)) \approx -\frac{kB}{2}\varphi^2 sin(\theta)$$

For the small angles under consideration, we can further approximate:

$$sin(\varphi) \approx \frac{sin(\phi)}{sin(\theta)} \rightarrow \varphi \approx \frac{\phi}{\sin(\theta)}$$

such that the phase term becomes:

$$\Phi \approx -\frac{kB}{2}\frac{\phi^2}{\sin(\theta)}$$

and the associated measured height will be:

$$h \approx -\frac{C}{kB}\Phi = -\frac{H}{2}\phi^2$$

A key result of this derivation is that the measured height will have, in addition to the surface topographic heights (neglected thus far in this derivation), an additional systematic height bias term associated to the instantaneous azimuth look angle, which comes from the fact that the lines of constant range (iso-range lines) and the lines of constant phase (iso-phase lines) even in the absence of topography are not perfectly aligned (see Figure 86). Since this last term is weighted by the height of the platform, it is not negligible and will require absolute knowledge so as to remove the contribution of an azimuth pointing control error, as will be discussed further below. Recalling that the OBP produces interferograms for a series of sub-beams that divide the azimuth real aperture pattern, the magnitude of the phase bias associated to each beam as a function of position in the swath is shown in the figure below.

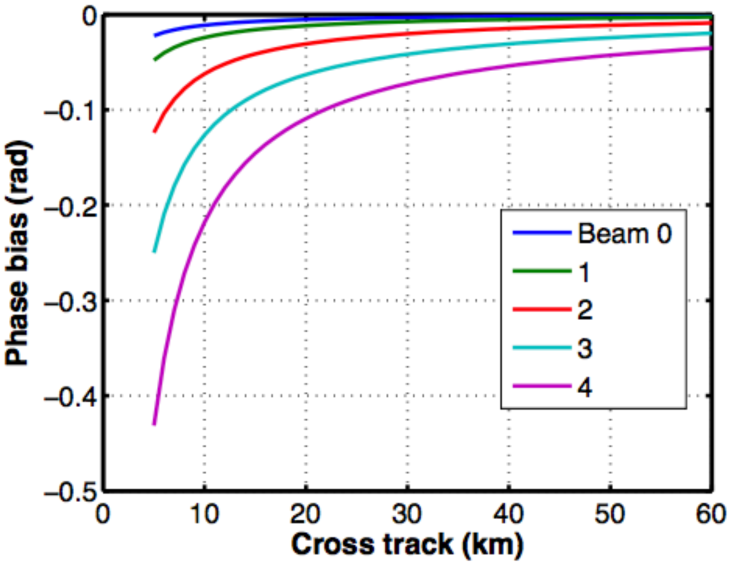

Figure 87. Phase biases as a function of cross-track for each one of the interferometric beams generated by the OBP (beam 0 represents the center beam, and beam 4 represents the most outer beam; only half of the beams are shown since the biases are identical between the respective forward/backward beams).

When converting the phase of the interferogram for a given beam j out of the OBP to heights during ground processing, the obtained heights will include this systematic bias plus the surface height averaged by the product of gains, sigma-0 and the azimuth interferometric response:

$$h^J = \frac{\int G_1(\phi)G_2^*(\phi)\sigma_0(\phi)\chi_{az}^j(\phi)\left(-\frac{H}{2}\phi^2 + h(\phi)\right)d\phi}{\int G_1(\phi)G_2^*(\phi)\sigma_0(\phi)\chi_{az}^j(\phi)d\phi}$$

We will now look at the overall effect taking into account the interferometric response of the system. Approximating again the product of the gains, sigma-0 and azimuth interferometric response by a Gaussian function of azimuth angle ϕ, centered at ϕ_j and variance σ_j, and assuming a linear slope in the topography such that $h(\phi) = h_0 + h_\phi \phi$, the above equation can be solved and results in:

$$h^J \approx \frac{1}{\sqrt{2\pi}\sigma_j}\int e^{-\left(\frac{\phi-\phi_j}{\sqrt{2}\sigma_j}\right)^2}\left(-\frac{H}{2}\phi^2 + h_0 + h_\phi \phi\right)d\phi \approx -\frac{H}{2}\left(\phi_j^2 + \sigma_j^2\right) + h_\phi \phi_j$$

We now define the effective squint angle ϕ_{sq} as the squint resulting from the product of antenna gain, sigma-0 and azimuth interferometric response. This effective squint angle under flat Earth conditions is given by:

$$\tan(\phi_{sq}) = \tan(\theta_{yaw})\frac{C}{r} \rightarrow \phi_{sq} \approx \frac{1}{15}\theta_{yaw}$$

$$\tan(\phi_{sq}) = \tan(\theta_{pitch})\frac{H}{r} \rightarrow \phi_{sq} \approx \theta_{pitch}$$

where C is the cross-track distance, H is the platform altitude, and r is the range distance. Note that for the case of yaw, the effective squint is more than an order of magnitude lower than the actual yaw angle of the antennas, indicating a much lower sensitivity to yaw errors. The height error associated to the knowledge error of ϕ_{sq} is given by:

$$\delta h \approx -H\phi_{sq}\delta\phi_J$$

where ϕ_J is the center of beam j. The height error associated to a topographic slope, s, is:

$$\delta h \approx s \cdot r \cdot \delta\phi_{sq}$$

The pointing requirements associated to these results are discussed in the following sections.

8.2 Absolute Pointing Control Requirements

The main consideration for the absolute pointing control requirement is the overlap of the two interferometric antennas to maintain the SNR. Since a given swath is imaged from both antennas, their footprint on the ground need to overlap to ensure that the overall SNR, as it relates to the random error performance, is preserved. In particular, a roll error can be directly related to a SNR loss. The impact of beam misalignment in the SNR is sufficiently small when the errors amount to less than $1/10^{th}$ of the beamwidths.

The second consideration arises from the decorrelation associated to the interferometric iso-phase and iso-range misalignment increasing as beams move away from the azimuth boresight (nominally 0 degrees). As previously discussed, a pitch or a yaw create an angular decorrelation; a pitch angle has an impact roughly 15 times larger than a yaw.

The third consideration is limiting the motion errors. As previously discussed, absolute pitch (and to a lesser extent, yaw) control errors amplify the errors associated to motion errors.

Finally, SAR operation is typically impacted by shifts in the Doppler Centroid associated to pointing control errors, but the onboard processor implements Doppler Centroid tracking to estimate the fractional Doppler Centroid to mitigate this error. The on-board estimation is actually performed separately for each interferometric pair, and their average is used in the processing.

From an azimuth perspective, both motion errors and systematic angular bias errors drive the need to limit the total 1-sigma pitch error to 33 mdeg, which is sub-allocated as 17 mdeg (1-sigma) to the S/C for attitude control in pitch, and 16 mdeg (1-sigma) to the Payload (ultimately KaRIn). The KaRIn error component covers primarily thermoelastic stability of the boom and antenna system, since the mechanical antenna system includes an alignment mechanism to be able to bring most static biases to zero after on-orbit deployment. Note that the pitch that is actually important is the common pitch, which is the average pitch of the two interferometric channels (the differential pitch, or differential azimuth error, will be discussed later in the context of random errors).

From an elevation perspective, the optimal nominal that optimizes the overall interferometric performance corresponds to the nominal KaRIn electrical boresight(s) elevation pointing angle of ±2.65 deg. In order to preserve the random error performance, the electrical elevation and azimuth boresight angles of the KaRIn antennas need to remain within 0.066 deg (1-sigma) of the nominal angles during science observations. At the same time, this is compatible with the pointing error requirement for the Jason series of altimeters of 0.2 deg (3-sigma), satisfying the nadir altimeter needs as well. The elevation pointing error is also sub-allocated to both the S/C and the Payload (KaRIn). The 1-sigma and 3-sigma control requirements of 0.066 deg and 0.2 deg, for roll and yaw respectively, result in 1-sigma and 3-sigma random errors of approximately 4.5 mm and 11 mm, respectively, which is to be RSS'ed with the nominal random performance. This impact to the shape of the random error performance across the swath is illustrated below.

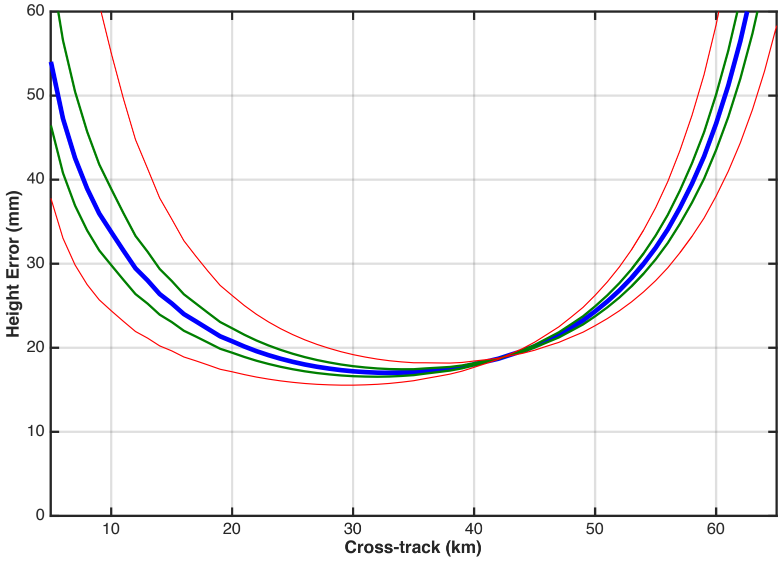

Figure 88. The impact of the overall pointing control error on the (perfect pointing) random performance of KaRIn (blue curve) is illustrated for the cases of 1-sigma (+/-0.067 deg, green curves) and 3-sigma (+/-0.2 deg, red curves).

In addition, the antennas need to maintain a relative azimuth pointing between them. This follows the same principles as before, but it is only sub-allocated to KaRIn. Given the narrow beamwidth of the antennas in the azimuth direction, of approximately 0.11 deg, the requirement is a tenth of that, or 0.011 deg (1-sigma), to yield a 1-sigma error < 1mm.

8.3 Relative pointing knowledge requirements

The relative pointing knowledge requirements are driven by systematic errors. As discussed in the systematic error section, the roll introduces an error that is proportional to the roll angle error times the cross-track distance; the pitch and yaw introduce smaller errors. The sensitivity of the knowledge error to pitch angle is ~0.14 cm/asec (at a pitch error angle of 0.067 deg). This is about 2 orders of magnitude less than the sensitivity of the roll angle (~21cm/asec), and therefore a knowledge drift error of 2.5 asec over 2.6 min is allocated to the KaRIn gyro (which, in fact, provides the same level of knowledge on all 3 axis).

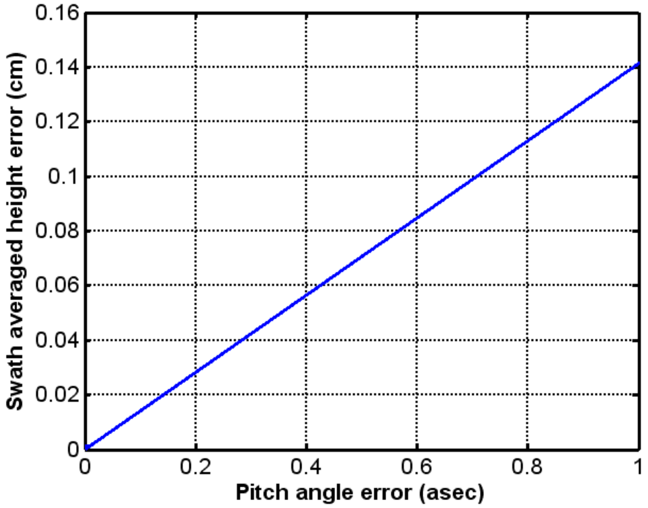

Figure 89. Swath average height error as a function of pitch drift knowledge error

8.4 Absolute pointing knowledge requirements

The absolute pointing knowledge errors are driven by geolocation errors as well as the ability to calibrate out any systematic errors introduced as part of the onboard processing. A pitch knowledge error of 0.01 deg at a pitch control error of 0.066 deg would create systematic errors as high as 6 cm, as shown in the figure below.

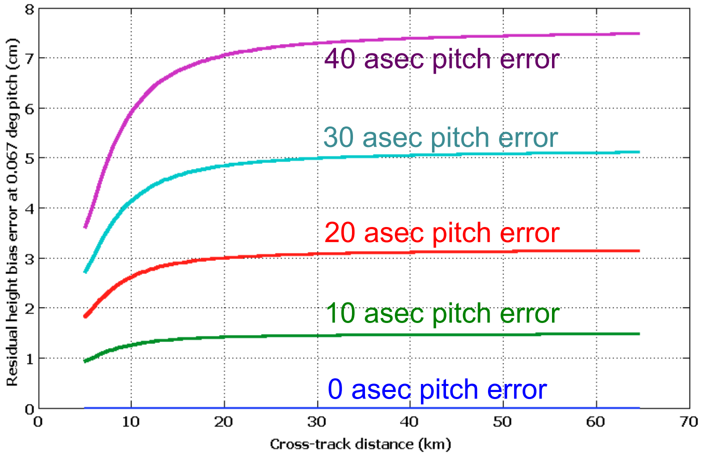

Figure 90. Residual bias errors for different pitch knowledge errors at a pitch of 0.067 deg

While cross-over corrections may be used to reduce these errors, they cannot be applied to remove short scale errors (<1,000 km). Therefore, the absolute 1-sigma knowledge pitch error requirement is specified as 0.020 deg to ensure that these errors do not exceed 0.5 cm, and it is levied on the star tracker on the S/C. The absolute roll knowledge error requirement is specified as 0.01 deg (1-sigma), as is the yaw. KaRIn does not have any "knowledge" of thermoelastic effects; therefore, it is required that any contribution of any thermoelastic effects on the common pitch of each of the KaRIn antenna beams shall not exceed 0.016 deg 1-sigma, throughout the mission life (after on-orbit alignment).

8.5 Pointing requirements summary

The key pointing requirements can be summarized as per the table below.

Table 17. Summary of key pointing requirements

Requirement	Allocations
Roll Absolute Pointing Control of 0.066° (1σ)	• 0.033° (1σ) to Payload (KaRIn) • 0.033° (1σ) to S/C bus
Common Pitch Absolute Pointing Control of 0.033° (1σ)	• 0.016° (1σ) to Payload (KaRIn) • 0.017° (1σ) to S/C bus
Differential Pitch Absolute Pointing Control of 0.011° (1σ)	• 0.011° (1σ) to payload (KaRIn)
Pointing knowledge drift error (1σ)	• Yaw and Pitch: 2.5 asec over 2.6 min (KaRIn's gyro) • Roll: PSD equivalent to ~25 masec over 2.6 min (KaRIn's gyro)

Absolute Pointing Knowledge: Baseline Yaw, Roll - 0.01° (1σ) Common Pitch - 0.02° (1σ)	• Baseline Yaw, Roll: 0.01° (1σ) to S/C bus
	• Common Pitch:
	  • 0.011° (1σ) to S/C bus
	  • 0.009° (1σ) to Payload (KaRIn)

Absolute Baseline Yaw Steering Control Error of 0.066 deg (1σ)	• 0.033° (1σ) to S/C bus • 0.033° (1σ) to Payload (KaRIn)

9 Timing Correlation Error Budget

The timing errors that are being considered here corresponds to errors in the time-tagging accuracy of the payload data, as required to corregister all the different payload measurements. Errors in the time-tagging will result in systematic errors.

For a given signal $x(t)$ with a Fourier transform given by $X(f)$ and power spectral density (PSD) given by $S_x(f) = \lim_{T\to\infty} \frac{1}{T} E[|X(f)|^2]$, the error associated to a constant timing (bias) error in measuring it, is given by:

$$PSD\,\{\, x(t) - \, x(t - t_0)\} = \lim_{T\to\infty} \frac{1}{T} E\left[|X(f)|^2 - \left|X(f) e^{-j2\pi f t_0}\right|^2\right] =$$
$$= |S_x(f)|^2 \left|1 - e^{-j2\pi f t_0}\right|^2$$

In some cases, the signal is not fully known. However, an estimate of the order of magnitude of the timing accuracy can be obtained as a function of how many times the signal is above a pre-established knowledge requirement level, in spectral form. Assuming that the PSD of the signal, $S_x(f)$, is α times the PSD of a given knowledge requirement, $S_{req}(f)$:

$$S_x(f) = \alpha\, S_{req}(f)$$

and establishing that the residual error induced by the timing error should not increase the overall error in spectral form by more than *p* %, then we have that:

$$\left|1 - e^{-j2\pi f t_0}\right|^2 \alpha\, S_{req}(f) \le \frac{p}{100}\, S_{req}(f)$$

therefore:

$$\alpha \le \frac{p/100}{|1 - e^{-j2\pi f t_0}|^2}$$

With some further simple algebraic manipulations we can simplify this equation as follows, resulting in a timing accuracy of:

$$t_0 \le \frac{1}{\pi f} \operatorname{asin}\left(\frac{1}{20}\sqrt{\frac{p}{\alpha}}\right)$$

It is worth noting that there is a dependence with the frequency, and that the most restrictive time bias will be imposed by the maximum frequency of interest. Therefore, the timing required derived in this way is the one that adds a p % of error at that frequency.

The primary measurement that is most sensitive to timing errors are the gyros, given that they operate at the highest sampling frequency (the KaRIn gyros offer data synchronization via a sync signal, which will be used at 64 Hz), and the roll error, in particular, is one of the most important contributions to the error budget. A relative degradation of the gyro error measurement in a spectral sense of 1% is allocated at the maximum resolved frequency (half the sampling frequency, i.e., 32 Hz). The magnitude of the roll signal that will be measurement during the mission is not known, but hereafter assumed to be <1.8 asec over 3 minutes. Given that the error knowledge of the gyro over the same interval integrates to approximately 25 milliasec, this results in a spectral signal-to-error ratio of $(1.8/25\text{e-}3)^2 \sim 5\text{x}10^3$, requiring an overall time correlation relative stability error between the KaRIn measurement and the gyro measurement of better than 7 usec.

In addition, the system is imposed a 0.1 m ground geolocation knowledge requirement due to timing errors, which corresponds to approximately 17 usec at the S/C velocity of 6.5 km/s.

In summary, the absolute time correlation error with respect to TAI is allocated a not-to-exceed bias of 17 us, which is sub-allocated as follows:

- S/C time 1 PPS absolute accuracy of 11 us (including S/C GPS and S/C PPS delivery errors).
- KaRIn: 5 us time accuracy (relative to the received 1 PPS).
- KaRIn gyro: 1 us time accuracy (relative to the received 1 PPS).

The relative error between KaRIn and its gyro is allocated 7 us, which is sub-allocated as follows:

- S/C time 1 PPS stability: 1 us
- KaRIn: 5 us time precision.
- KaRIn gyro: 1 us time precision.

10 Appendix A: SWOT Science Orbit

Although more detailed orbital analysis will be captured on a separate document, here we discuss the basic characteristics of the SWOT nominal science orbit, as defined today. These are provided for description purposes only and do not constitute the ultimate orbit/trajectory analysis, which are captured in the SWOT Mission Analysis document [16].

The basic set of osculating orbital parameters are as follows:

- Semi-major axis: 7277.384316216 km
- Eccentricity: 0.001142626633
- Inclination: 77.60752027474
- Longitude of ascending node: 35.32561775537 deg
- Argument of periapsis: 113.5047240618 deg
- Mean anomaly: 66.37526684875 deg

Which are defined at time 1/1/2020, 12:00:00.

Some basic parameters, such as the geodetic altitude and beta angle for the SWOT platform are shown in the following figures.

.

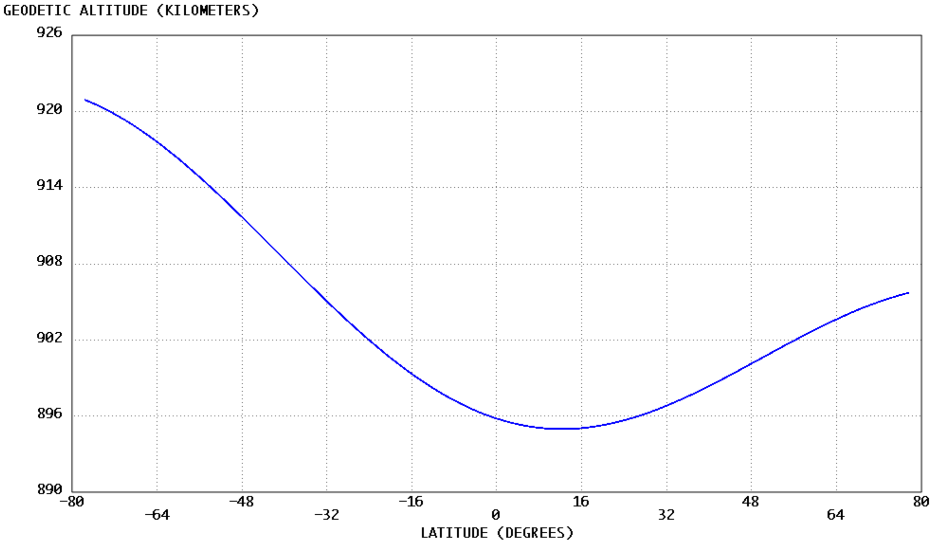

Figure 91. Geodetic altitude (in km) as a function of latitude.

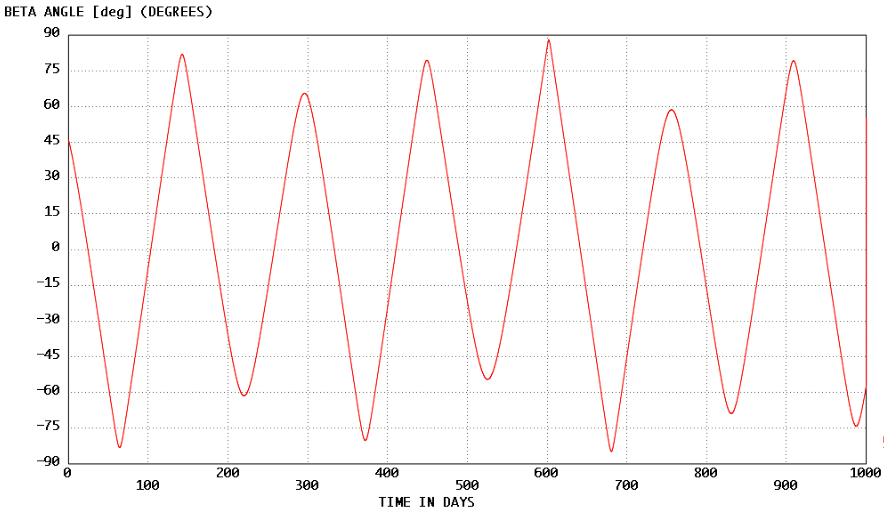

Figure 92. Beta angle as a function time in days

11 Appendix B: Derivation of the spectral form of the slope error

Starting from the basic definition of the slope $s(t)$ as the derivative of the heights, $h(t)$:

$$s(t) = \frac{h(t+\Delta t) - h(t)}{v_g \Delta t} = \frac{1}{v_g}\frac{\partial h(t)}{\partial t}$$

where v_g is the ground speed of the platform, and the units of the slope are radians when $h(t)$ is in cm and v_g is in cm/sec. The Fourier transform of the slopes, $S(f)$, is then given by:

$$S(f) = \int dt \frac{1}{v_g}\frac{\partial h(t)}{\partial t} e^{-j2\pi ft} = \frac{j}{v_g} 2\pi f \int dt\, h(t) e^{-2\pi jft} = \frac{j}{v_g} 2\pi f\, H(f)$$

where $H(f)$ is the Fourier transform of the heights. The power spectral density (PSD) of the selopes, PSD_s is then related to the PSD of the heights, PSD_h by the following expression:

$$PSD_s = \frac{(2\pi)^2 f^2}{v_g^2} PSD_h$$

To convert from rad^2/cy/sec to rad^2/cy/km, we need to multiply by v_g in units of km/sec:

$$PSD_s[rad^2/cy/km] = v_g \left[\frac{km}{sec}\right] \frac{(2\pi)^2 \left(f\left[\frac{cy}{sec}\right]\right)^2}{\left(v_g\left[\frac{cm}{sec}\right]\right)^2} PSD_h[cm^2/cy/sec]$$

$$= (2\pi)^2 \left(\frac{f\left[\frac{cy}{sec}\right]}{10^5\, v_g \left[\frac{km}{sec}\right]} \right)^2 PSD_h[cm^2/cy/km]$$

$$= (2\pi)^2 10^{-10} \left(f\left[\frac{cy}{km}\right]\right)^2 PSD_h[cm^2/cy/km]$$

To convert the slope to units of μrad:

$$PSD_s[rad^2/cy/km] = \left(10^6 \left[\frac{\mu rad}{rad}\right]\right)^2 (2\pi)^2 10^{-10} \left(f\left[\frac{cy}{km}\right]\right)^2 PSD_h[cm^2/cy/km]$$

$$= (2\pi)^2 10^2 \left(f\left[\frac{cy}{km}\right]\right)^2 PSD_h[cm^2/cy/km]$$